UNIVERSIDADE DE LISBOA
FACULDADE DE CIÊNCIAS
DEPARTAMENTO DE FÍSICA

Exploring Cellular Mechanics in ARSACS: An AFM-Based Analysis of Elasticity and Viscoelasticity

João Augusto Antunes Belo

Mestrado em Física
Física Estatística e Matéria Condensada

Dissertação orientada por:
Prof. Mário Rodrigues
Prof. Federico Herrera

2024

Acknowledgements

Felizmente este tipo de documentos não está realmente terminado até os agradecimentos estarem em ordem.

Gostaria primeiramente de agradecer aos meus orientadores Mário S. Rodrigues e Federico Herrera que me guiaram neste projecto sem nunca se cansarem. Ao Prof. Mário mesmo que não concordemos em algumas (muitas) coisas queria agradecer a paciência, ajuda e que me tenha "dado na cabeça" quando era preciso. Ao Prof. Federico agradeço a paciência para lidar com um físico que não sabia bem o que uma célula era e pelo suporte mesmo quando desaparecia durante uns meses.

Queria também agradecer aos dois laboratórios que me acolheram, ao AFMaRT laboratory e ao Cell Structure and Dynamics Lab por me terem acolhido e ajudado quando preciso. Do AFMaRT laboratory gostaria de agradecer especialmente ao Tiago Robalo, à Ana Carapeto, ao Pedro Freixo, ao Tiago Cordeiro e à Joana Nobre pelo apoio e por não me deixarem apodrecer no laboratório. Do Cell Structure and Dynamics Lab gostaria de agradecer especialmente ao André, à Fernanda, à Ana e ao Pedro por me ensinarem a cultivar células e pelas conversas a descer do piso 4 ao piso 1 e a voltar.

Gostaria também de agradecer aos meus pais, tios, avós, primos por estarem sempre presentes na minha vida, por me "obrigarem" a ser uma versão melhor de mim próprio e por terem plantado em mim o amor pela ciência e pelo conhecimento desde pequeno.

Dos muitos anos que (in)felizmente passei na faculdade existem demasiadas pessoas a quem agradecer, mas tentando ser o mais breve e sem tentar esquecer me de ninguém (vou inevitavelmente esquecer). Agradeço à Joana, ao Duarte, ao Bruno, ao Pedras, ao Calé, à Daniela, à Catarina, ao Fernandes, à Laura, à Caipiro, a Vanessa, ao Rafa, ao Neves, ao Ricardo e a todos os outros que estão comigo desde o 2017 e com os quais passei noites sem fim a fazer nada, tarde a beber cerveja, manhãs a dormir em aulas e dias sem fim a estudar.

Não podia agradecer a tanta gente sem me esquecer de agradecer a Carolina Cipriano, à Rita, à Madalena, ao Chico e ao Tomás, ao David, a Matilde, à Toscano, ao João, ao Pedro, ao Afonso e a todos abaixo deles, foram uma familia que escolhi, me calhou por sorte e que me escolheram, agradeço que tenham estado sempre ao meu lado e que tenham tido essa confiança em mim. Tenho também a agradecer a todos os meus sobrinhos "de avacalho" por me aturaram e fazerem companhia. Sem esquecer de agradecer a todos que pisaram aquele pedaço de terreno (e os ao lado) ao mesmo tempo que eu, por tudo o que significam e fizeram por mim.

Gostaria também de agradecer a Fight Club Jiu-Jitsu Portugal especialmente ao Mestre Heitor Moura por me ajudarem a melhor focar os meus objectivos, ao Clube Musical União por me fazer lembrar o que significa esforço e ter amor à camisola, agradecendo a ambos por me ajudarem, como pensavam Sócrates e Tucídides, a manter o corpo mais perto do pensamento.

Trabalho suportado por PTDC/FIS-MAC/2741/2021 (doi:10.54499/PTDC/FIS-MAC/2741/2021) Project grant from FCT, Portugal and UIDB/04046/2020 (DOI: 10.54499/UIDB/04046/2020) and UIDP/04046/2020 (DOI: 10.54499/UIDP/04046/2020) Centre grants from FCT, Portugal (to BioISI).

Resumo

Neste trabalho estudámos as propriedades mecânicas de células quando sujeitas a diferentes alterações do citoesqueleto. Para isso desenvolvemos um algoritmo que permite analisar curvas de força obtidas por microscopia de força atómica (AFM) e deduzir parâmetros que refletem as propriedades mecânicas das células, tanto elásticas como viscoelásticas.

Começamos por enfatizar a importância das propriedades mecânicas, como a rigidez, elasticidade e viscosidade, nos processos celulares. Estes parâmetros mecânicos são cruciais para o crescimento, movimento, adesão celular e progressão de doenças, nomeadamente no cancro. Alterações nas propriedades mecânicas de células têm vindo a ser apontadas como potenciais biomarcadores para várias doenças.

As alterações nas propriedades mecânicas das células estão frequentemente associadas a doenças. Por exemplo, as células cancerígenas tendem a ter propriedades mecânicas distintas que lhes permitem invadir tecidos e metastizar, tipicamente exibindo menores valores de elasticidade. De forma semelhante, em doenças como a fibrose quística, as células infectadas tendem também a apresentar valores menores de elasticidade.

As células eucarióticas são compostas por quatro elementos principais, membrana celular, organelos, núcleo e citoplasma. Neste último os filamentos citoplasmáticos formam uma rede denominada de citoesqueleto. Este consiste numa malha tridimensional composta por microtubos, filamentos intermédios e filamentos de actina. O citoesqueleto contribui para a forma e organização da célula, movimento celular, propriedades mecânicas e é também usado como "carril" por proteínas motoras. O citoesqueleto desempenha um papel fundamental no suporte mecânico das células.

Este estudo foca-se especificamente nos filamentos intermédios. Estes têm um diâmetro médio de 10 nm. Dos três tipos de filamento do citosesqueleto, os filamentos intermédios são os que estão mais associados às propriedades mecânicas das células. A doença Ataxia Espástica Autossómica Recessiva de Charlevoix-Saguenay (ARSACS), uma doença degenerativa rara, está associada a mutações no gene *SACS* que causa a truncação ou má formação da proteína sacsina. Esta mutação causa perturbação da estrutura normal do citoesqueleto, causando uma acumulação de filamentos intermédios na zona perinuclear (perto do núcleo).

Para estudar a perturbação do citoesqueleto são utilizadas células modelo. As células usadas são células de glioma C6 geneticamente modificadas de tal forma a inativar o gene que gera a sacsina, ($C6^{Sacs-/-}$). Estas células reproduzem características das células de doentes com ARSACS.

Estas células mutantes exibem formações citoesqueléticas anormais, particularmente nos filamentos intermédios, que estão ligados a condições neurodegenerativas. Este estudo também explora o potencial do uso da Withaferina A (WFA), um *"steroidal lactone"* natural, que é conhecida por causar acumulações de filamentos intermédios na zona perto do núcleo, como um modelo farmacológico de ARSACS, visto que altera o citoesqueleto de uma maneira similar aos outros modelos de ARSCAS.

A microscopia de força atómica ou AFM (do inglês atomic force microscopy) é a ferramenta utilizada para estudar as propriedades mecânicas das células neste trabalho. O microscópio de força atómica permite obter deflexões, deslocamentos piezoelétricos e tempo, permitindo o cálculo de propriedades mecânicas. Neste estudo para medir as propriedades das células, foi usada uma metodologia de AFM que permite obter não só as propriedades mecânicas através

de curvas de aproximação e retração mas também aproximações da topografia das células. A metodologia é denominada *Force-Volume*, na qual se fazem grelhas em que cada ponto/píxel é um conjunto composto por uma curva de aproximação e uma curva de retração. Neste metodologia a topografia é obtida através do cálculo do ponto de contacto, ou seja, o ponto em que a ponta do cantilever e a amostra entram em contacto, fazendo isto para todos os píxeis da grelha é possível obter uma aproximação da topografia da célula.

O módulo de Young, que descreve a elasticidade linear de um material ou a forma como tende a resistir à deformação imposta por pressões externas, é obtido tanto para as curvas de aproximação como para as de retração usando o modelo de Hertz. As curvas de retração são também usadas devido ao facto de se assumir que todas as deformações plásticas acontecem na curva de aproximação. São discutidos e comparados os modelos parabólicos e esféricos para indentação para calcular o módulo de Young, concluindo que a aproximação parabólica apesar de não ser a aproximação mais correcta, continua a ajustar de maneira satisfatória até pelo menos indentações da ordem do diâmetro do indentador esférico. Das mesmas curvas de aproximação e retração são também obtidos parâmetros viscoelásticos como E_1, que mede a rigidez a longo termo em relação ao tempo de carga, E_2, que mede a rigidez a curto termo em relação ao tempo de carga, τ, o tempo de relaxamento e η, a viscosidade, através de uma solução do modelo *standard linear solid model* (SLS) em que se considera a indentação realizada por uma esfera, esta também numa aproximação parabólica.

Tipicamente só a contribuição elástica é medida na forma de um módulo de Young aparente. Neste trabalho desenvolve-se uma estratégia para aplicar o modelo SLS às células, o que permite uma análise detalhada da elasticidade e viscoelasticidade celular. O estudo expande a análise já existente ao incorporar a viscoelasticidade, uma propriedade que combina tanto elasticidade quanto viscosidade. O comportamento viscoelástico é essencial para melhor entender como as células se deformam e recuperam sob stress mecânico, o que tem implicações em processos como a metastização do cancro e a cicatrização de feridas.

São obtidas as distribuições de valores de propriedades mecânicas para células individuais e conjuntos de células, observando-se que para células individuais as distribuições são normais e para conjuntos de células as distribuições são log-normais, independente do tipo de célula.

Dos resultados das medições de AFM em células do tipo selvagens (WT) (do inglês *wild-type*), mutantes (MT), WT cultivadas em WFA e WT cultivadas em dimetilsulfóxido (DMSO) são obtidos "mapas" de topografia e propriedades mecânicas *"médias"* de modo a melhor perceber a distribuição das propriedades mecânicas. Através destes mapas descobriu-se que as células tendem a ter menor valores de módulo de Young de aproximação, E_{app}, e retração, E_{ret}, assim como de E_1 e E_2 para a zona perto do núcleo, enquanto que τ tem valores mais elevados na zona perto do núcleo. A viscosidade, η, aparenta ser aproximadamente constante em toda a célula.

É também estudado a relação entre a mediana de E_1, E_2 e η com a mediana do módulo de Young das curvas de aproximação. Obtendo-se que E_1/E_{app} para células WT e MT tem distribuições similares e valores medianos superiores aos valores de células WT cultivadas em WFA e DMSO, que são similares entre si. E_1/E_{app} é maior para células WT como esperado. A normalização E_2/E_{app} é maior para as células MT e ainda maior para células WT cultivadas em WFA e células WT cultivadas em DMSO. É claro que o cultivo de células em DMSO tem impacto nas suas propriedades elásticas. Os dados normalizados apontam para que haja uma semelhança entre células WT cultivadas em WFA e células WT cultivadas em DMSO no que diz respeito aos seus valores de E_1 e E_2. O DMSO é o veiculo através do qual a WFA é administrada,

o que pode justificar a semelhança nas propriedades elásticas destas células. Os valores de E_1 e E_2 também estão alterados no caso das células MT, mas não tão significativamente como nas anteriores. Sendo assim através das propriedades elásticas do modelo SLS é possível identificar quais as células sob o efeito da droga.

Foram observadas diferenças nas propriedades mecânicas entre estes quatro grupos. Em termos de Módulo de Young obtido através do modelo de Hertz, os valores para todas as células são similares. O valor de E_2 é similar para células MT e WT cultivadas em DMSO e diferente para WT e WT cultivadas em WFA. Os resultados sugerem que as perturbações no citoesqueleto devido a mutações ou à administração de drogas, como a WFA, afetam significativamente a mecânica celular.

Os resultados sobre as propriedades mecânicas das células fornecem informações valiosas que podem levar ao desenvolvimento de novos alvos terapêuticos para doenças associadas a anomalias no citoesqueleto.

Palavras-chave: Microscopia de Força Atómica, Propriedades mecânicas, Viscoelasticidade, Mecanobiologia, Filamentos Intermédios

Abstract

Studying cell mechanical properties is crucial for understanding various biological processes and disease mechanisms. Incorporating both elastic and viscoelastic properties into the analysis allows for a more complete understanding of cellular mechanics and supports biomedical applications. While measuring viscoelasticity in cells is challenging due to their complexity and current technological limitations, advances in measurement techniques are enhancing our ability to study these properties. This knowledge is essential for accurately modeling biological systems and has significant implications for understanding health and disease.

This study explores the impact of cytoskeletal alterations on single-cell mechanical properties, including stiffness, elasticity, and viscoelasticity. These properties were studied by disrupting the cytoskeleton, particularly the intermediate filaments (IF). This disruption was achieved in two ways: first, using C6$^{Sacs-/-}$ cells, a cellular model for ARSACS (a disease known to impair intermediate filaments); and second, pharmacologically by incubating healthy C6 cells with Withaferin A, a naturally occurring steroidal lactone, that has also shown to cause intermediate filament disruption.

To obtain the mechanical properties of the cells, cells were studied using Atomic Force Microscopy (AFM). The data was analysed using Hertz model to obtain the Young's modulus for approach and retract curves. The Hertz model chosen was the parabolic approximation for a spherical indenter, which was compared to a more robust approximation of a spherical indenter obtained from the Sneddon solution to the contact problem. To obtain the viscoelastic properties, E_1, E_2, τ and η, the data was analysed using a modified SLS model.

Average values for topography, Young's modulus, and viscoelastic parameters were calculated for wild-type (WT), mutant (MT), WT treated with Withaferin A (WFA), and WT treated with Dimethyl sulfoxide (DMSO). Key differences in cellular mechanics were identified between these groups, providing insights into how cytoskeletal disruptions affect cellular behaviour, particularly in diseases like ARSACS.

Keywords: Atomic Force Microscopy, Mechanical Properties, Viscoelasticity, Mechanobiology, Intermediate Filaments

Contents

List of Tables

List of Figures

Chapter 1

Introduction

1.1 Cells

Cells are the structural and functional basis of all living organisms, being referred as the building blocks of life. Cells are divided into two groups, eukaryotic and prokaryotic. Eukaryotic cells possess a membrane bound nucleus while prokaryotic cells do not.

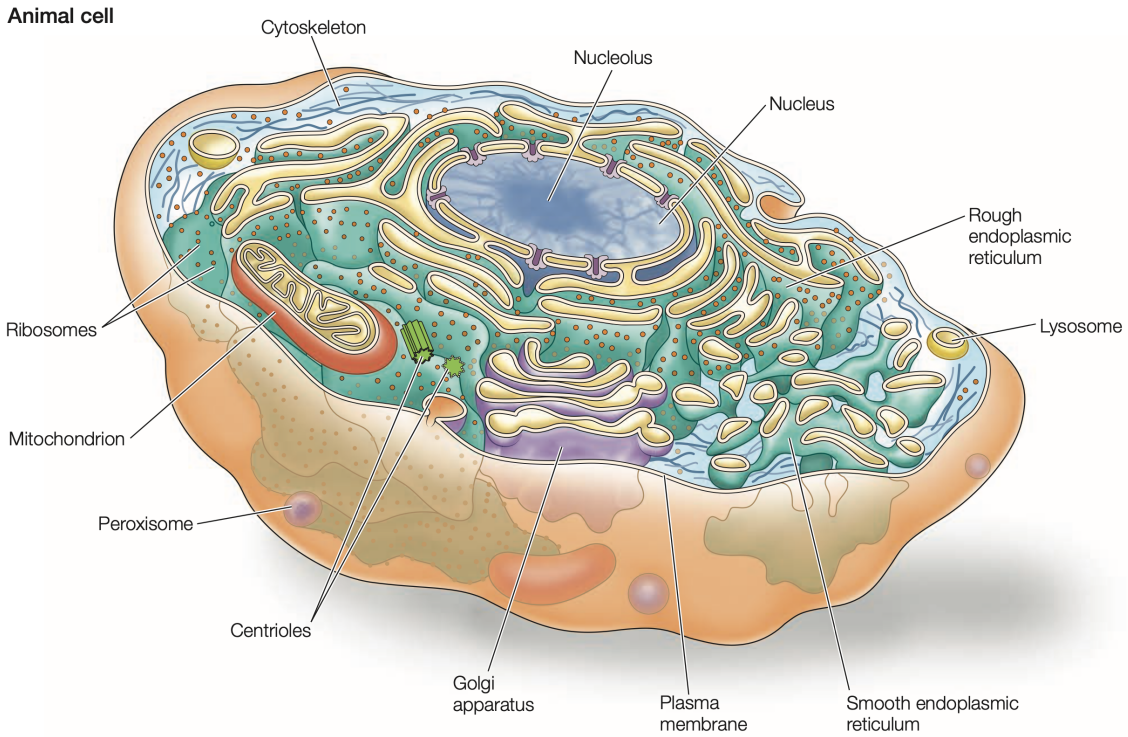

Figure 1.1: Schematic representation of an eukaryotic cell. Adapted from ref. [1].

Cells are a highly complex system which can take on very different types, from osteoblasts (bone-borming cells) to neurons (brain cells). It is estimated that the adult human body alone has more then 200 different cell types [2], and approximately $30 \cdot 10^{12}$ cells [3].

An eukaryotic cell is composed of four main elements: cellular membrane, organelles, nucleus and cytoplasm. In the cytoplasm, cytoplasmic filaments form a meshwork known as the

cytoskeleton.

The cytoskeleton is a highly complex, dynamic three-dimensional network, that grants the cell its shape and its physical/mechanical properties, it is responsible for cell movement, serves as "rails" in which proteins move, acts as a scaffold for positioning organelles and attaches to the cell membrane [4].

The cytoskeleton is composed of 3 biopolymers/proteic filaments: microtubules (MT), intermediate filaments (IF) and actin filaments (AF) and a plethora of cross-linkers and molecular motors. Like any other system of polymers its mechanical properties are dependent on the mechanical properties of the individual polymers, how the link between polymers is done, and how the polymers are arranged in 3D space [5, 6, 4]. The link between filaments can be of various forms as filaments are connected to each other via molecular motors (kinesin, myosin, etc), cross-linkers (plectin, tau, etc) and direct bonding (actin+vimentin, MTs+neurofilaments) [7]. The polymer arrangement varies depending on the polymer type. AF forms bundles (tightly packed parallel array of cross-linked AF) and networks (3D meshwork orthogonally cross-linked). In a non-meiosis/mitosis cell, MT stretch from the centrosome to the cell membrane, and in nerve cells axons and dendrites, MT align either in parallel or antiparallel to each other. IF form a complex continuous network from inside the nucleus to the cell membrane [1].

Due to the existence of molecular motors mentioned before, the cytoskeleton is not an ordinary polymer network, as the motors move along MT and AF, which leads the cytoskeleton to be an active material that is out of thermodynamic equilibrium [8, 9]. Thus, creating a model that describes it is not trivial.

In this work the main research focus will be intermediate filaments (IF) as they play a key role in diseases. Before intermediate filaments were named, they were studied in the form of keratin, one of the proteins from the IF family. In 1932, William T. Astbury published the first data of a periodic structure of keratin [10], obtained from x-ray diffraction on hair, wool and other related fibers. In 1952, Francis Cricks predicted the α-helical coiled coil structure of IF [11, 12]. In 1976 Petter Steinert discovered the *in vitro* polymerization of IF in the absence of a denaturing reagent, "into filaments that have the same structure as the *in situ* keratin filaments", from the seven α-keratin polypeptides *in vitro* in a dilute salt solution [13]. In 1968, Holtzer and colleagues named the intermediate filaments when they discovered "filaments indermediate in diameter" [14] when studying skeletal muscle cells cultured from chick embryos . In most multicellular animal cells IF can be found "almost" uniformly distributed throughout the cell. While AF are coded into 6 genes and MT are encoded into 12 genes (6 for α and 6 for β-tubulin) encoding the same proteins and their isoforms. IF are encoded in at least 70 genes with several isoforms. The proteins encoded can have vastly different sizes, for example, keratin 19 (K19) weighing $\sim$40 kDa and nestin weighing $\sim$240 kDa, and in some cases are able to copolymerise. IFs proteins are divided into 6 protein types. Type I-IV are found in the cytoplasm of various cells, Type V are found in the nucleus and type VI are found in lens [1, 17].

Some relevant IFs for this work are glial fibrillary acidic protein (GFAP) a type III IF which is expressed in the central nervous system, playing a role in mitosis [18], it also plays a major role in Alexander's disease [19], a rare disease. Vimentin, another type III IF is expressed in mesenchymal cell, it plays a role in organelle organization [20] and is able to remove toxic proteins [21]. Nestin a type VI IF is expressed predominantly in nerve cells when this are in an early stage of development, after that it is down regulated and replaced by other IFs, although it can be up regulated in adulthood in case of some pathological situation [22].

IFs proteins share a common structure, a central α-helical rod with a C-terminal tail and a N-terminal head (polypeptide). Two polypeptides twist their α-helical rods with aligned C and N-terminals to form a dimer. Two dimers associate in slightly staggered and antiparallel way to from tetramer. Tetramers associate with other tetramers, end to end, to form a protofilament, which will wound around other 7 protofilaments in a ropelike fashion to form an IF, with diameter around 10 nm and up to several μm in length.

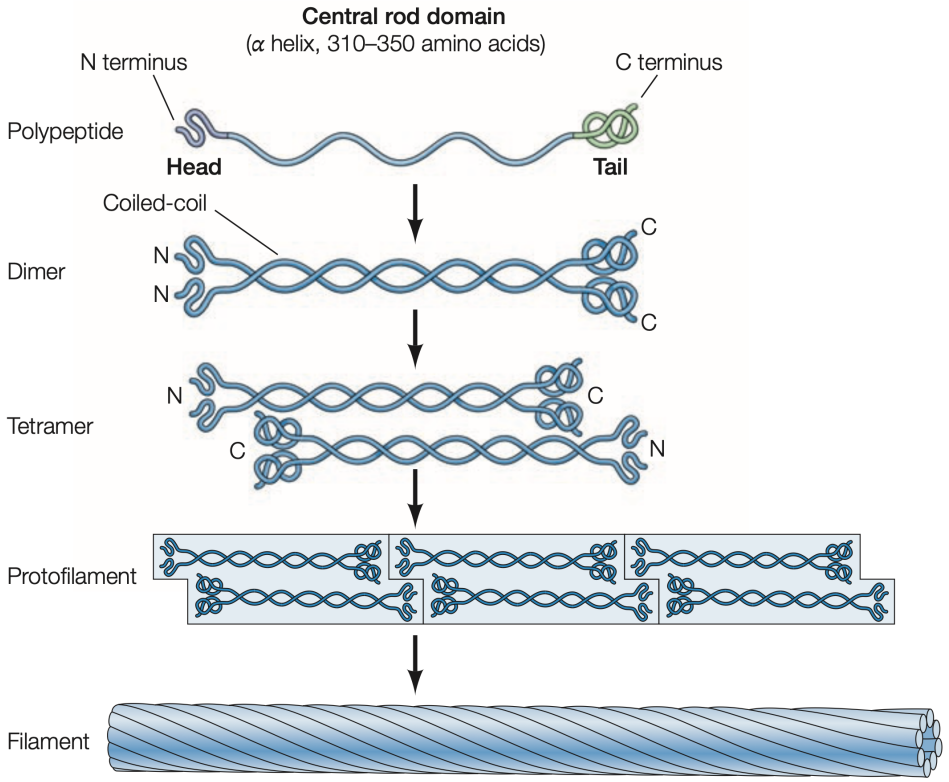

Figure 1.2: Structure and assembly of intermediate filaments. Adapted from ref. [1].

It should also be noted that contrary to MT and AF, IFs are apolar, not having a distinct plus and minus end. IF assembly requires in some cases interaction between different types of IF proteins [1].

Unlike the other filaments IFs do not have a prominent role in cell movement, instead they are responsible of providing mechanical support to cells, positioning the nucleus within the cell, cell-cell/cell-substrate adhesion (via desmosomes and hemidesmosomes respectively) and intracellular signalling.

1.1.1 Disease caused by cytoskeleton alteration

Disruption of the normal structure and function of the cytoskeleton is associated with several diseases [23]. Some examples of diseases cause by disruption of the cytoskeleton are Nemaline myopathy (mutation in the encoding gene of α-actin) [24], Lissencephaly (mutation in the encoding gene of α-tubulin) [25] and Alexander disease (Mutation in the encoding gene of glial fibrillary acidic protein) [26]. Other diseases associated with IFs, White sponge nevus [27], Emery–Dreyfuss muscular dystrophy [28], Hutchinson–Gilford progeria syndrom [29] and Au-

tosomal Recessive Spastic Ataxia of Charlevoix-Saguenay (ARSACS) [30], etc., all caused by mutation of IF protein encoding genes [23].

ARSACS is a rare neurodivergent disorder most prevalent on the region of Charlevoix-Saguenay in Canada, where it was first described in the 1970's [31], with cases reported around the world [32, 33, 34]. It is characterised by an early onset (early childhood), progressing as the patient ages, of progressive cerebellar ataxia (a lack of voluntary coordination of muscle movement) , peripheral neuropathy, and spasticity (abnormal muscle tightness due to prolonged muscle contraction) [30], although other complications have been observed [35, 36] and phenotypes without one of the three complications have also been reported [37, 38, 39, 40, 41, 42]. This disease results from mutations in the sacsin encoding gene, *SACS*, which causes truncated or defective sacsin proteins [30], leading to accumulation of IF in ARSACS patient neurons [43], a hallmark easily observed via immunocytochemistry and widefield imaging [44] in ARSACS model. Sacsin the protein which is responsible for ARSACS weights 520 kDa having its highest expression on central nervous system cells, also being expressed in uterus, kidneys and liver cells [45]. Although sacsin's cellular function is not yet completely clear, it acts as a co-chaperone, helping maintaining protein homeostasis [46]. It was found that sacsin knockout (inactivating the gene that is responsible for sacsin encoding) causes a overly interconnected and functionally impaired mitochondrial network, accumulation of mitochondria [47] and abnormal bundling of neurofilaments (IF) in multiple cell types and celular models [48]. In cells with reduced sacsin expression and ARSACS patients fibroblasts, an abnormal perinuclear (near the nucleus) accumulation of vimentin (an IF) was present [49].

In order to better study ARSACS and due to the fact that ARSACS is a rare disease adding to ethical concerns and cell replicative capacities (Hayflick limit), cells from patients with the disease are not feasible for long term study. As such a model is needed. Experiments with sacsin knockout ($Sacs^{-/-}$) mice have reproduced many key ARSACS features, such as early onset, cerebellar ataxia, upper motor neuron axonopathy (describing various lesions affecting axons in the brain, spinal cord, and peripheral nerves), peripheral neuropathy, and intermediate filament accumulation, suggesting that ARSACS is driven by sacsin loss-of-function [43]. Hence most of the existing models are either based on genetically modified sacsin knockout/depletion or induced pluripotent stem cell (iPSC) [50] from patient cells, models such as sacsin knockout mice [47, 43], sacsin knockout neuroblastoma cells [51], iPSC motor neurons and Purkinje cells [52], which mainly focus on neuronal cells. However, prior to *Murtinheira et al.* [44], studies into ARSACS were focused on neurons, leaving the role of glial cells in this disease largely unexplored. Glial cells, which are responsible for providing physical and chemical support to neurons and maintaining the neuronal environment, could also play a role in ARSACS.

To study the effects that alterations of cytoskeleton have in mechanical properties mutated C6 cells will be used. C6 cells or wild type (WT) cells are a spindle-like cell that was extracted from an induced rat glioma in the 1960's [53]. Glioma is a type of tumor that originates in glial cells, and makes approximately 30% of all brain and central nervous system tumours and 80% of all malignant brain tumours [54].

$C6^{Sacs-/-}$ cells or C6 Mutant (MT) cells are a genetically modified group that will be used as an ARSACS model. These cells appear to be smaller and were shown to have accumulations of IF (vimentin, nestin and glial fibrillary acidic protein (GFAP)) in the juxtanuclear area. Sacin depletion also caused pathological hallmarks of ARSACS similar to those observed in neuronal cells [44].

IF disruption is transversal to all cellular models of ARSACS, we looked for a drug that could mimic these effects, and thus establish the first pharmacological model of ARSACS. The drug found was Withaferin A (WFA), as WFA binds directly to vimentin causing fragmentation of the IF [55], inhibiting vimentin [56] and shows perinuclear vimentin accomulation [55, 56] just as in other models.

Withaferin A (WFA), is a withanolide, a naturally occurring steroidal lactones. It exists in plant of the *Solanaceae*/Nightshade family, including, *Withania*, *Vassobia*, *Trechonaetes*, *Physalis*, *Jaborosa*, *Exodeconus*, *Dunalis*, *Acnistus*. Other than the *Solanaceae* family, withanolides can be found in plants of the *Fabaceae*, *Lamiaceae*, *Myrtaceae* and *Taccaceae* families [57]. WFA is found in *Withania somnifera*, commonly named Ashwagandha, a remedy used in Ayurvedic/Indian medicine. WFA as many pharmacologically well-established activities [58] such as, anticancer and cancer chemopreventive effect [59], apoptosis induction in cancer cells [60], sensitization to chemotherapy [61], anti inflammatory effects [62], immunomodulation [63], bone healing [64], anti fibrosis effect [65] and others [66, 67, 68, 69]. It will be this model ($C6^{Sacs-/-}$) and possible models (C6 cells cultured in WFA) of ARSACS cells that will be used in order to study the effect of cytoskeletal alteration causes in the mechanical properties of cells.

1.2 Importance of mechanical properties of cells

The mechanical properties of cells, such as stiffness, elasticity and viscosity are of significant importance as they play a vital role in a wide range of biological/cellular activities/processes such as cell growth, cell division, cell motion, cell adhesion [70], disease progression [71, 72] and drug-cell interactions [73]. Other cellular processes where mechanical properties are involved are cell differentiation [74] and tissue forming[75], as cells can sense their mechanical environment and respond accordingly (mechanotransduction [76]).

Mechanical properties also impact cell shape as well how they function. For instance, the stiffness of a cell can affect its ability to migrate and invade tissue [77], which plays a pivotal role in biological processes like wound healing [78] and cancer metastasis.

Another important factor to consider about mechanical properties of cells is that changes in these properties are associated with various diseases [79, 80, 81, 82].

A disease that often shows difference in mechanical properties with disease progression is cancer [81, 83, 72, 84, 85]. Studying the changes of the mechanical properties can give insights into cancer progression, invasion and metastasis, leading to new diagnostic markers, therapeutic targets or prognosis. Other disease that show alteration of mechanical properties are Ischemia, a disease which causes reduction in blood supply to the heart, whose patients have red blood cells with lower average stiffness than those of the control group [86]. Idiopathic pulmonary fibrosis (IPF), a disease where excessive extracellular matrix is produced, patients fibroblast show a greater stiffness than those of the control group [87]. Cystic fibrosis (CF), is a disorder characterised by damage to the lungs, pancreas, liver, kidneys, and intestine. Cystic fibrosis bronchial epithelial (CFBE) cells with severe CF caused by deletion of phenylalanine 508 were shown to have a Young's modulus smaller than non CF CFBE cells [88]. In fact, mechanical properties can also be used as diagnostic tool [89, 90, 86, 91]. In tissue engineering, mechanical properties are essential for designing scaffolds, as the mechanical environment can influence cellular behaviour like tissue formation [92]. Another importance of mechanical properties is in cellular differentiation, as the mechanical cues provided by the extracellular matrix can queue

differentiation of stem cells into specific lineages [93, 94], which is important for regenerative therapies.

Investigation into cellular mechanical properties can be a powerful tool to better understand fundamental biological principles such as cell migration, division and their interaction with the environment. Embryogenesis and organogenesis can also be better understood if further our knowledge on the changes in mechanical properties that occur during the development of a fetus [95].

Complementing the study of elastic properties with studying viscoelastic properties provides a more in-depth understanding of cellular and tissue mechanics. Viscoelastic analysis not only enhances our understanding of normal physiological processes but also may aid in exploring disease mechanisms and contribute to the development of advanced biomedical applications.

A notable property of biological tissues and cells is that they exhibit viscoelastic behaviour, that is, they behave both with elastic (solid-like) and viscous (liquid-like) properties. This allows cells to be deformed and later recover the original shape. Understanding this behaviour is essential to understand tissues and cells in physiological settings, where they are subjected to multiple loading and unloading processes regularly (e.g. touching something). The ability of cells to deform and recover shape after application of external forces is often thought to be time dependent. For example after a cell is compressed, it is initially deformed and then will gradually return to its original shape (this happens both due to elastic forces and by cytoskeleton remodelling. The characteristic time of cytoskeletal remodelling is to the best of our knowledge, unknown, thus, some elastic effects might be due to cytoskeletal filament growth). This time dependence might impact cellular processes like migration, proliferation and mechanotransduction.

The viscoelastic properties of a cell can influence their ability to migrate to extracellular matrix or pass between two cells. Viscoelastic materials are known for flowing under constant pressure. For a cell this would allow it to *"flow"* through tight spaces as per processes like wound healing or metastasis. Just like some tumor metastasis are able to penetrate lymphatic or blood vessel [96].

Understanding the changes in the mechanical properties of tumor cells can provide insights into cancer progression, metastasis, and spread, as well as the influence of the mechanical environment on tumor development.

In tissue engineering, incorporating viscoelastic properties into the scaffold material might enhance cell attachments, proliferation and differentiation as it better mimics the natural extracellular matrix.

For bioreactor, a controlled environment used to grow and maintain cells, understanding the viscoelastic behaviour of cell might help optimize the condition for cell growth. Another area that benefits from incorporating viscoelasticity are computational models used to predict cell behaviour under load.

Since there is still no widespread and unanimous protocol and method for analysis of cells mechanical properties using Atomic Force Microscopy (AFM), this results in different values for the same material even for simple properties such as the Young's modulus [97]. More complex properties, such as viscoelasticity, are not usually analysed when using an AFM, due to the complexity involved.

With this work we hope to define a simple method to calculate cell's elastic properties as well as develop a new and simple method to obtain cell's viscoelastic properties based on atomic force microscopy and related techniques.

1.3 Mechanical properties

The mechanical properties of a material give us a relation of an applied load/stress to the deformation/strain. Materials can be categorised via several properties, the two most relevant to this work are elasticity and viscosity. Elastic materials are characterised by having a well-defined conserved shape, deforming under an applied load (until a finite deformation, where the deformation becomes permanent), returning to its original shape when force is removed. Viscous materials are characterised by their ability to deform under load, without maintaining a fixed shape. Contrary to elastic materials, viscous materials do not return to their original shape after the load is removed.

1.3.1 Young's modulus

The Young's modulus, E, describes the stress-strain response in the direction of the load of a material being loaded uniaxialy. It is defined by $E = \sigma/\varepsilon$, where σ is a tensile or compressive stress and ε is the strain, defined by $\varepsilon = (L' - L)/L$, where L is the the original length of the material and L' is the length of the material after the stress as been applied.

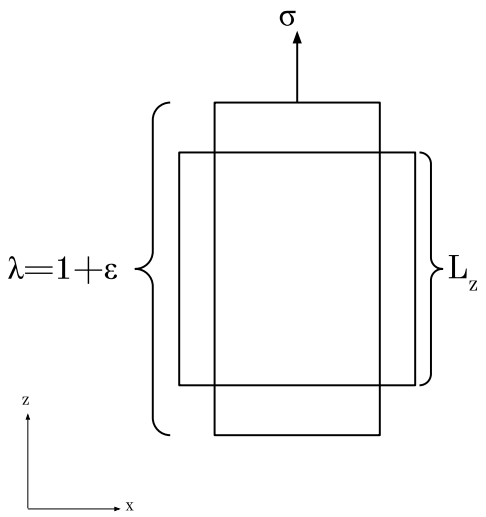

Figure 1.3: Schematic representation of elastic deformation caused by pulling on one of the sides of a square. σ is the stress applied, λ is the elongation/extension/stretch ratio, $\lambda = L'_z/L_z$, where L_z and L'_z are the length of the material in z before and after being deformed, ε is the axial/elongational strain, it is related to λ by $\varepsilon = \lambda - 1$.

When the material is stretched in the z direction, it usually becomes smaller in the other axis. If we assume an isotropic material, the reduction in size will be equal for both axis. The strain in the x axis will be $\varepsilon_x = L'_x/L_x - 1$. And from that we can obtain the Poisson's ratio, $\nu = -\varepsilon_x/\varepsilon$. The Poisson's ratio measures the expansion or contraction of a material in the direction perpendicular to the applied load. The Poisson's ratio for most regular materials ranges from 0 to 0.5. Though rarely, values below 0 can be observed in particular materials, such, as some *exotic* crystalline material [98, 99, 100], polymer foams [101] and folded origamis [102]. The Young's modulus is one of the several quantities used to quantify/describe the stress-strain response of a materials. For an isotropic material the Young's modulus can be obtained from the shear modulus by $E = 2G(1 + \nu)$, where ν in the Poisson's ratio. In Table 1.1 some examples of Young's modulus are given.

Table 1.1: Some Young's modulus for biological samples and the method used to obtain it.

	Young's modulus	Technique
trabecular bone	10.4 ± 3.5 GPa	Microtensile test [104]
trabecular bone	14.8 ± 1.4 GPa	Ultrasonic tests [104]
cortical bone	18.6 ± 3.5 GPa	Microtensile test [104]
cortical bone	20.7 ± 1.9 GPa	Ultrasonic tests [104]
femoral artery (canine)	10.4 ± 1.5 MPa	[105]
saphenous vein	4.2 ± 3.3 MPa	Bioreactor [106]
medial gastrocnemius muscle	22.59 ± 3.31 kPa	Shearwave ultrasound elastography [107]
lateral gastrocnemius muscle	23.56 ± 4.08 kPa	Shearwave ultrasound elastography [107]
achilles tendon	363.38 ± 41.11 kPa	Shearwave ultrasound elastography [107]

1.3.2 Viscoeslaticity

Viscoelasticity is a property of materials which combines both the resistance to flow of viscous materials and the capacity to return to the original shape after deformation of elastic materials. Unlike purely elastic materials, viscoelastic materials have a strain rate dependence on time and dissipate energy during their loading and unloading, this can be seen in their hysteresis of the loading and unloading loops. Another key characteristic of viscoelastic materials is creep, the gradual deformation of materials when under a constant stress/load. Once the load is removed viscoelastic materials tend to recover back to their original shape or close to it, depending on how much energy was lost.

Table 1.2: Some viscosity values for common liquids.

	Viscosity (Pa·s)	Ref.
Water	10^{-3}	[108]
Skim milk	$1.4 \cdot 10^{-3}$	[108]
Whole milk	$2.12 \cdot 10^{-3}$	[108]
Olive oil	$8.4 \cdot 10^{-2}$	[108]
Honey	$0.3 - 70$	[109]

Standard linear solid

There are several methods of modelling viscoelastic behaviour, one of those is the standard linear solid (SLS) or Zener model. The SLS model has advantage over the simpler Maxwell model or Kelvin–Voigt model, as it can describe both creep and stress relaxation in the same model. In the Maxwell representation, it consists of a spring (restorative force) in series with a spring and dashpot (damping force) in parallel, like it is represented schematically in FIG.1.4.

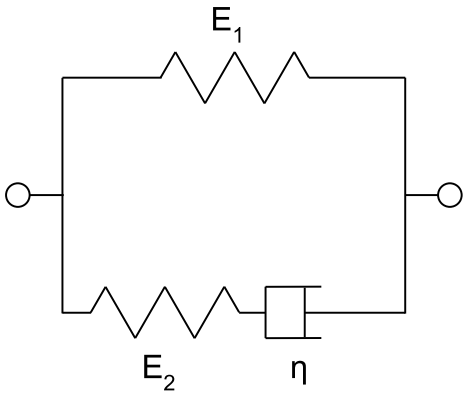

Figure 1.4: Maxwell representation of the SLS model. Where E_1 and E_2 are the Young's modulus of the springs and η is the viscosity of the dashpot.

The constitutive equation for the Maxwell representation of the SLS model is:

$$\sigma + \frac{\eta}{E_2}\dot{\sigma} = \frac{\eta(E_1 + E_2)}{E_2}\dot{\varepsilon} + E_1\varepsilon \tag{1.1}$$

Where E_1 is s the Young's modulus of the restoring spring, the solo spring in Fig.1.4, E_2 is Young's modulus of the spring coupled to the dashpot in Fig.1.4, η is the viscosity of the dashpot in Fig.1.4 and $\tau = \frac{\eta}{E_2}$.

We will use this model, because, as it was said before, this model can describe both creep and stress relaxation, and we expect this to be able to describe, at least in a first approximation, the cells' viscoelastic behaviour.

1.4 Cell describing models

Despite the complexity of cells, there have been several attempts to describe them as a set of equations, either analytically or numerically. Mechanical models of living cells can be fitted into 2 groups: the continuum models and the micro/nanostructural models. The continuum cell models, can be subdivided into 2 major categories, viscoelastic and biphasic models. The viscoelastic models can then be subdivided into the cortical shell–liquid core (or liquid drop) models, the solid models and the fractional derivative models. micro/nanostructural models can be also subdivided into 2 major categories, cytoskeleton models for adherent cells and spectrin-network model for erythrocytes (red blood cells) [110].

The liquid drop models were first developed for micropipette aspiration rheology experiences and have since then developed into several different models [110].

The simpler model is the Newtonian liquid drop model where the cell cortex is modelled as fluid layer with constant tension and the cell "cytoplasm" is assumed to be a Newtonian liquid [111].

As cells are not homogeneous, and the nucleus is stiffer than the cytoplasm [112, 113], a more complex model was needed [112, 114]. Consequently a 3 layers model was developed [115]: the compound Newtonian liquid drop model is composed of an outer cortex with constant tension, a cytoplasm as a Newtonian liquid, a nuclear cortex with constant tension, and the nucleoplasm modelled as a more viscous Newtonian liquid.

When studying the dependence of the apparent viscosity of the aspiration pressure at large

deformities, it was found that the apparent viscosity decreased with the increase in aspiration pressure, via a power-law, as such the shear thinning liquid drop model was developed. The latter is omposed of an outer cortical layer with constant tension and the cell "cytoplasm" is modelled to be a lower-law liquid [116].

The Newtonian, compound Newtonian and shear thinning models are good models for micropipette aspiration with large deformation of the cell. To explain the inicial entry the Maxwell liquid drop model was developed, where a cell is modelled as a cortex with constant tension and the cell "cytoplasm" is assumed to be a Maxwell fluid [117].

In solid viscoelastic models, the cell is assumed to be homogeneous without considering shells/layers like in the cortical shell–liquid core models. "By assuming homogeneity, the mechanical parameters needed are reduced. This greatly simplifies the experimental data analysis" [110].

The simplest model, the linear elastic solid model, assumes that the cells behave as an elastic solid, having no viscoelastic properties. For AFM experiments this model is used when using Hertzian models.

A more complex model is the standard linear solid model, although, in this context, it was first used to study small deformation on micropipette aspiration experiments [118], it will be the model used in this work and will be explored further in the next sections.

The fractional derivative model or power-law rheology model was developed [119, 120, 121, 5] as a way to account for response of adherent cells that are exposed to time varying forces in their environment. It is based on empirical data, that several material exhibit similar properties, this materials are also called "soft glassy" as like glass they can't thermodynamically equilibrate [122]. This model is applicable to AFM when a probe is oscillating in contact with the cell [110].

The biphasic model was developed as a way to account for the fact that cells' cytoplasm is made of 2 separated phases, the "solid" cytoskeleton and the liquid cytosol [123, 124, 125]. It is a more complex model using constitutive equations derived from mixture theory assuming mass conservation and binary mixture of a linearly elastic solid matrix with viscous properties and an incompressible viscous fluid [123].

There are several types of cytoskeleton models for adherent cells, such as, tensegrity models, where the cell cytoskeleton is modelled as stable self-tensioning structures, where isolated bar/struts bear the compression and cables bear the tension [126, 127].

Another example of this type of model is the open cell foam model, where the cytoskeleton (microfilament network) is modelled as an open lattice and its mechanical properties are obtained using theory of foams [128].

The spectrin-network model for erythrocytes models the erythrocyte cytoskeleton (network of spectrin filaments connected to the lipid bilayer via a pletora of intermediate proteins [129, 130]) as a network of polymer chains [131, 132, 133].

1.5 Measuring the cell's mechanical properties

As explained, cell mechanical properties are an important factor when talking about a plethora of cellular processes/activities, and as such measuring them in a precise, sturdy and replicable way is of great interest. Several methods have been used to study single cell's mechanical properties such as AFM, optical stretching, optical tweezers, parallel plate, cell monolayer rheology, particle tracking, magnetic twisting cytometry, magnetic tweezers, microfluidics, micropipette

aspiration, acoustic methods [97, 70]. When measuring the same cell types with different measuring instruments one would expect that, the results from all the measurements, would be similar. However, how *Wu. Pei-Hsun, et al* [97] showed, by measuring the Elastic modulus of MCF-7 (Michigan Cancer Foundation-7) breast cancer cells using different method, the results showed a difference up to 1000 times for different measurement techniques. In the same study, measurements done with AFM with different tip geometry, size, temperature and loading rate also showed different values of Young's modulus, in the order of 25 times. Similar results (but not such a pronounced difference) were also shown in other publications [88, 134], when analysing C6 cells similar results were found, pointing to the heterogeneous nature of cells.

As we will see in this work, cells mechanical properties will be obtained via AFM, using force-volume curves, as it allows for calculation not only of the Young's modulus, adhesion forces and topography but also viscoelasticity.

Using an AFM to obtain cell viscoelasticity is more complex than obtaining the Young's modulus, since Young's modulus measurements are assumed to be quasi-static For viscosity, there is a time dependency that requires techniques that allow for measurement over time. As well, data analysis for viscoelasticity is more complicated, requiring a more sophisticated model to describe the cells' behaviour.

1.6 Concept of Atomic Force Microscopy

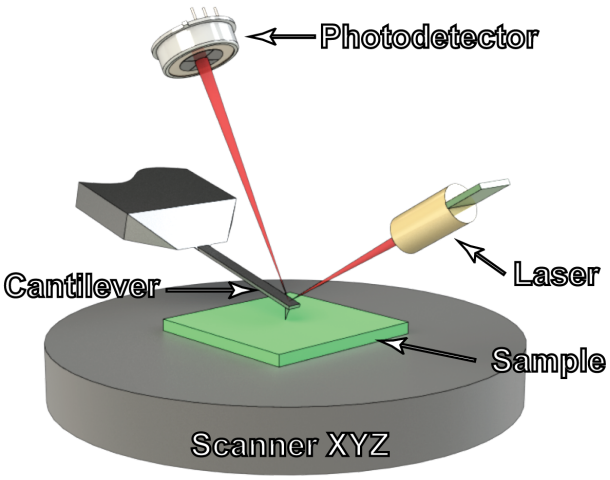

Figure 1.5: Schematic representation of atomic force microscopy experimental setup.

After the first scanning tunneling microscope (STM) in 1981 by Binning & Roher [135], a plethora of similar techniques emerge, including AFM (atomic force microscopy) [136, 137]. AFM is a technique of the type of Scanning Probe Microscopy, in which the interaction between a nano/micro metric probe and the sample surface are measured. This interaction is measured via the bending of a cantilever where the probe/tip is attached. In this work, the bending was obtained via laser beam deflection measured on a photodetector. Although laser beam deflection

give us the angle of the cantilever deflection, we assume that the small angle approximation is valid, and as such, the cantilever angle, θ, is proportional to the tip displacement, z.

There are several AFM methodologies that can be applied for different outcomes. The more common are contact and tapping mode, used to obtain topographies; and force-volume (or force spectroscopy), from which we can obtain topographies and physical properties, commonly Young's modulus and adhesion force, viscoelasticity can also be obtained from this AFM methodology, but it is more complex. All these methodologies are simple and easy to implement but are time consuming. Despite its simplicity, when these methodologies are used in liquid, they become more complex, as the cantilever suffers a much greater drag force and the interaction between the probe/tip and the sample is harder to control.

The more "traditional" use of AFM has proven a worthy tool, being used for surface imaging [138] and characterisation [139], nanomanipulation [140], investigation of adhesion [141, 142, 143], physical properties characterisation [144, 145, 146], etc., as well as being able to achieve subatomic resolution of molecules [147]. Since its creation in 1986 several AFM adjacent techniques were developed such as multifrequency force microscopy [148, 149, 150], high speed AFM [151, 152], FluidFM [153], correlative atomic force microscopy and near/far-field super-resolution microscopy [154, 155, 156, 157], localization AFM [158] and many more.

In the context of mechanobiology, AFM has been used for several reasons, the most common uses are obtaining cells images/topographies and mechanical properties using the methodologies exposed above.

In the late 1980's, AFM began to be used for measuring biological molecules, such as the work from *Gould, et al.* [159], where amino acid crystals were imaged and the image was consistent with X-ray diffraction data, *"pointing to the potential usefulness of atomic force microscopy for imaging molecules of biological importance"* [159].

In the 90's there was a *"boom"* of AFM usage in biology and biochemistry for various purposes, such as: cell imaging in air [160, 161, 162], cell imaging in medium [160, 163, 164, 165, 166, 167, 168, 169], cell mechanical properties [170, 171, 168, 169], cell change subjected to a flow [172], dna/chromossome imaging [173, 174, 175, 176], protein imaging [177, 178, 179, 180], molecular interaction [181, 182, 183], *etc* . One of the biggest advancements of the 90's for AFM was the development of tapping mode in liquid [186], which allowed for better resolution, reducing the deformation caused on cells by contact mode AFM, as even a small force applied through a cantilever tip causes immense pressure, *e.g.* a force of 1 nN applied with a cantilever point with radius of 8 nm at a penetration of 1 μm applies a pressure of $\sim$ 40 kPa. As forces larger then 100 pN can cause irreversible deformations [187].

Chapter 2

Methodology

In this work wild type (WT), mutant (MT), WT cells cultured in withaferin A (WFA) and dimethyl sulfoxide (DMSO) will be analysed to determine if any effects are observed when measuring their mechanical properties. This will be done using the SLS model in conjunction with the more common Hertz model. This allows us to get a deeper understanding of the possible differences between cell types, as the SLS allows us to look into cells' viscoelasticity while the Hertz model only explores cells' elasticity.

2.1 Cell culture and cell types

All the cells used for this work were grown in Prof. Federico Herrera's Lab (Cell Structure and Dynamics Lab) in Dulbecco´s Minimal Essential Medium (DMEM) low glucose (Biowest, Nuaillé, France) supplemented with 10%(v/v) fetal bovine serum (FBS) (Sigma-Aldrich, St. Louis, MO, USA) and 1%(v/v) Penicilin-Streptomycin (Thermo Fisher Scientific, Watham , USA) and maintained in a 37 °C humidified atmosphere containing 5% CO_2 following the protocol outlined in *Murtinheira et al* [44].

For AFM experiments, C6 glioblastoma (ATCC, CCL-107TM) cells or WT cells and C6$^{Sacs-/-}$ or MT cells were seeded in 35 mm sterile plastic plates, growing to confluence for at least 3 days.

To culture cells in Withaferin A, WT cells were seeded 35 mm dishes at a density of 150000 cells/vessel and, after achieving confluence, they were exposed to WFA (0.75 μM) and its vehicle (0.1% v/v DMSO) for 24h. WFA alone cannot enter the cell, and so, DMSO is used as a vehicle. The concentration of DMSO used was below what is considered low toxicity: $< 10\%$ [188]. To understand if any of the effect seen in cell cultured in WFA are due only to WFA, a control group of DMSO (0.1% v/v) was also analysed, after exposure to DMSO for 24h.

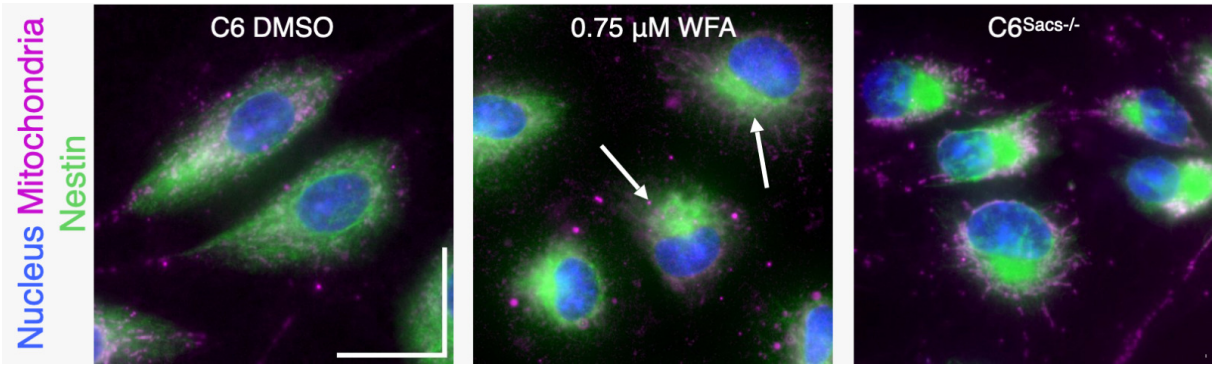

Figure 2.1: Fluorescence microscopy images of C6 cells cultured in DMSO (left), C6 cells cultured in 0.75 μM WFA (middle) and C6 MT cells (right), representing the distribution of nestin (green), mithocondrias (mangenta) and the nucleus (blue), the white arrows point to nestin aggretation, similar to those found on the MT cells. Image provided by Ana Sofia Ribeiro from Cell Structure and Dynamics Lab.

2.2 AFM

As stated before, the AFM has several operating modes, the most common ones are contact, tapping or dynamic and force-volume/force spectroscopy.

In the contact mode, the cantilever tip is in contact with the sample being imaged, while the tip scans over the sample, a feedback loops tries to maintain the interaction between the tip and sample constant by elevating or lowering the cantilever, this enables the creation of topographic maps of the sample.

In the tapping or dynamic mode, the cantilever is vibrating at a frequency near its resonating frequency near the sample's surface when scanning the relevant area. Due to the interaction between the tip and the sample, the oscillating amplitude will change, a feedback loop tries to maintain the oscillating amplitude constant by increasing or decreasing the tip-sample distance, resulting in a topographic maps of the sample.

In force-volume, the area to scan is divided into a grid, with approach and retract curves measured at each grid point. These curves can then be analysed to extract the sample's mechanical properties and topography as will be discussed later in this chapter.

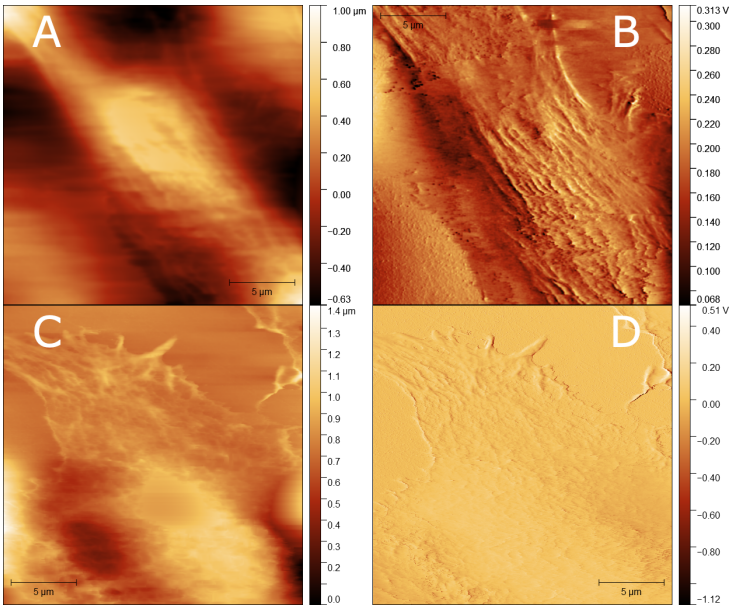

Figure 2.2: Images obtained using contact mode in liquid of WT cells. (A) and (C) are the topography and (B) and (D) are the deflection signal in the photodetector. In (A) and (B) a cell is shown. (C) and (D) a cell and its projection, which look appears to be a lamellipodium, is shown.

2.3 Obtaining mechanical properties of cells via AFM

The AFM records deflection, piezo expansion and time data from a user defined starting point to an endpoint, relative to the *resting* cantilever position. Time data at the start of the curve is $t_{initial} = 0$ and t_{final} at the end of the curve. The AFM generates a file containing a header with key parameters, followed by the acquired data. This data is processed using a script to produce approach and retract curves, which are referred to as *raw* curves and will be used in this work.

An approach curve is composed of the data from the user defined *start* until the user defined *end* or a relative difference larger than 10 V is reached. A retract curve is composed of the data from the maximum piezo expansion for the approach curve to the user defined start. Both of these curves are composed of triplets of time, piezo expansion and deflection. To calculate mechanical properties as it is intended in this thesis, the *raw* curves needs to be converted to a triplets of *usable* units, time, indentation and force. To obtain the indentation, δ, from the piezo expansion, z and the cantilever deflection, Δx, we use:

$$\delta = z - \Delta x \tag{2.1}$$

where, z is the piezo expansion and $\Delta x = cal \Delta V$; where, cal is the calibration of the photodetector obtained experimentally. To obtain the force, F, from the deflection, we use:

$$F = k \cdot cal \cdot \Delta V \tag{2.2}$$

where, k is the spring constant of the cantilever, cal is the calibration of the photodetector and ΔV is voltage in the 4 quadrant photodetector.

The calibration, cal, gives the distance the cantilever moves as a function of the voltage

measured in the 4 quadrant photodetector. It is calculated using a cantilever on a glass pane, as glass' contact stiffness is much larger than the stiffness of the cantilever, thus, the deformation of the glass is negligible when compared to the cantilever deformation. Therefore the slope of the deflection-displacement curve, after jump to contact (see section 2.4.1), will be the variation of the deflection with the movement of the cantilever, so, *cal* is the absolute value of the inverse of the slope. This was done using a script to get the linear part of the approach curve, and calculate its slope.

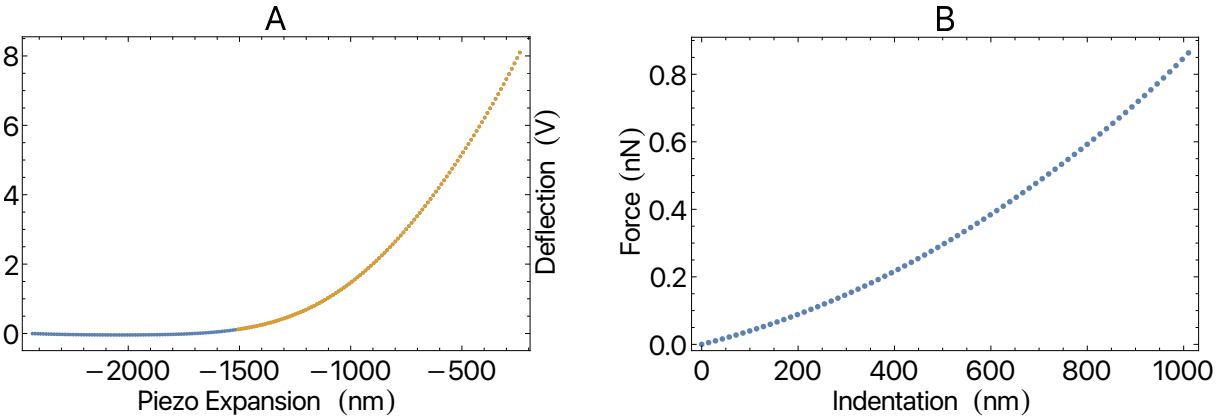

Figure 2.3: (A) Raw approach curve for a WT C6 cell, blue dots represent the part of the curve that will be discarded and the yellow dots the part of the curve that will be converted. (B) Converted curve from (A) using (2.1) and (2.2).

The data shown in Fig.2.3 (B) is referent only to the data points that were taken in contact between the probe and the sample (yellow region in Fig.2.3 (A)), as contact models can only be used after contact has been made. Therefore, we must define a contact point, for which all values before (or after for the retracting phase) must be cut off. This contact point is the point in which the cantilever tip enters in contact with the sample, however finding it is not trivial, leading to a set of problems that will be discussed later.

2.3.1 Calculating the Young's modulus

For this work, the Derjaguin–Müller–Toporov (DMT) model, which is a model for adhesive contact based on the Hertz theory of contact, but includes the effects of adhesion, as an extra attractive interaction term. This model assumes that the adhesion does not affect the Hertzian deformation profile. For a spherical indenter, assuming the parabolic approximation ($R_C = \sqrt{R\delta}$), the model is as follows:

$$F(\delta) = -F_{ad} + \frac{4}{3}E^*\sqrt{R}(\delta - \delta_0)^{\frac{3}{2}} \tag{2.3}$$

where, F_{ad} is the adhesion force, R is the radius of the spherical indenter, E^* is the effective Young's modulus ($E^* = E/(1-\nu^2)$), δ is the indentation and δ_0 is an offset of the indentation. To calculates E^* two approximations were made, first, we assumed the contact model of a sphere with a half plane although the cell is *plano-convex* shaped. Even if we assumed the *plano-convex* shape of the cell, R would be defined as $1/R = 1/R_{indenter} + 1/R_{cell}$, and as $R_{cell} \gg R_{indenter}$ we can assume $R = R_{indenter}$. Secondly, and in the same vein, $1/E^* = (1-\nu^2)/E_{indenter} + (1-\nu^2)/E_{cell}$ but as the indenter tip is made out of silicon dioxide (SiO_2), with

$E_{indenter}$ ranging from $\sim$ 60 GPa to $\sim$ 100 GPa [189, 190] while cells' measured for this work have E_{cell} is of the order of 1 kPa. Thus, because, $E_{indenter} \gg E_{cell}$ we assume $E^* = E_{cell}/(1-\nu^2)$, *i.e.* we assume that there is no deformation of the indenter.

2.3.2 Parabolic approximation

One problem that is commonly ignored that arises from using the parabolic approximation of the sphere, is that the approximation should only hold true for small indentations when compared to the indenter radius, for larger indentations the approximation should not be valid. When measuring cells the typical indentation we obtain is of the order of 1 μm, which is not much smaller than the radius of the indenter used (a sphere with 1 μm radius). One possible solution is to discard data after the indentation becomes larger than the radius of the indenter, but discarding data is also not a good solution. To make use of the complete set of data we use the solution proposed by Sneddon [191]:

$$\begin{cases} F(R_C) = \dfrac{E^*}{2} \cdot \left[(R_C^2 + R^2) \cdot \ln\left(\dfrac{R+R_C}{R-R_C}\right) - 2R_C R \right] \\ \delta = \dfrac{R_C}{2} \ln\left(\dfrac{R+R_C}{R-R_C}\right) \end{cases} \tag{2.4}$$

where, E^* is the effective Young's modulus ($E^* = E/(1-\nu^2)$), R_C is the contact radius, R is the radius of the spherical indenter and δ is the indentation. This expression is better expressed as a function of R_C rather than δ, unlike the parabolic approximation. We can not directly measure the contact radius, and so δ needs to be converted into R_C using the relation in Eq. 2.4, which has no known analytical solution, as such R_C is calculated numerically.

To better exemplify the difference in the contact radius, of the Sneddon solution for a spherical indenter, that will be referred as spherical approximation from now on, and the parabolic approximation, R_C for both approximations as plotted as a function of δ.

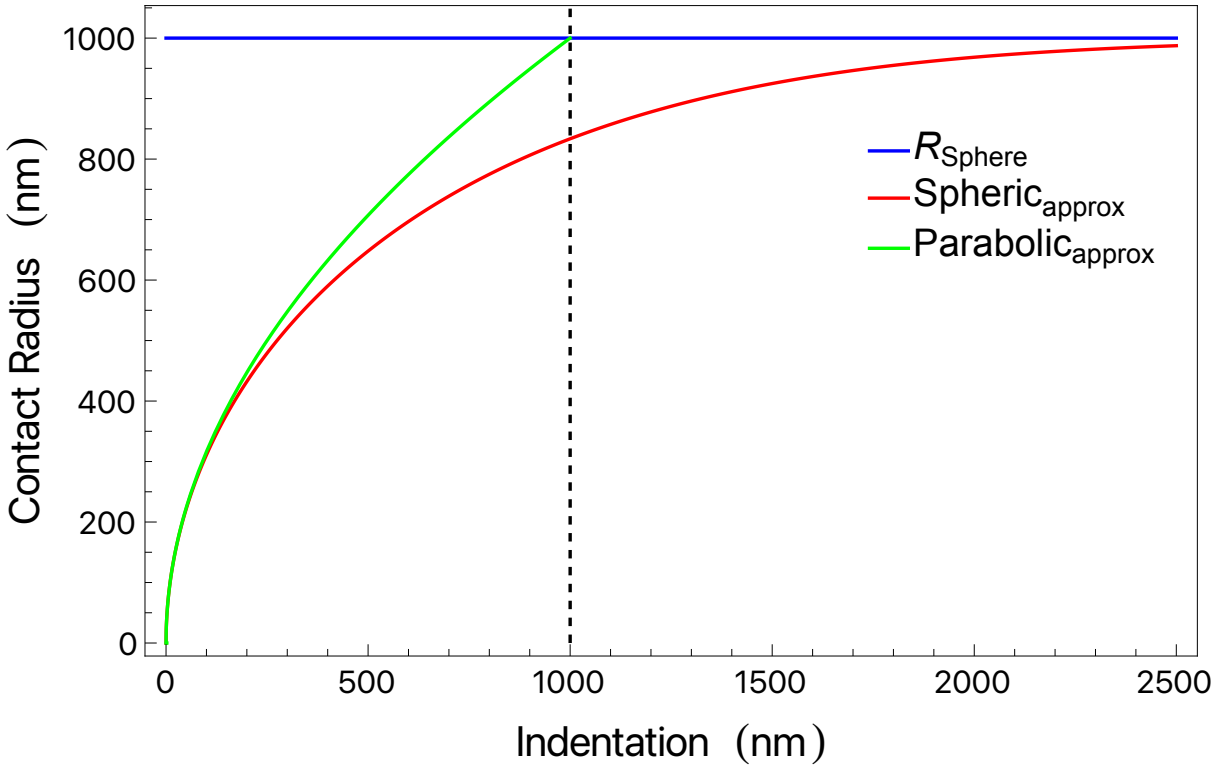

Figure 2.4: Comparison of the Contact Radius, R_C, for the spherical approximation and the parabolic approximation as a function of δ.

As can be seen in Fig.2.4 while in the spherical approximation the contact radius never exceeds that of the indenter. For the parabolic approximation after $\delta = R$, the contact radius will exceed that of the indenter (not shown).

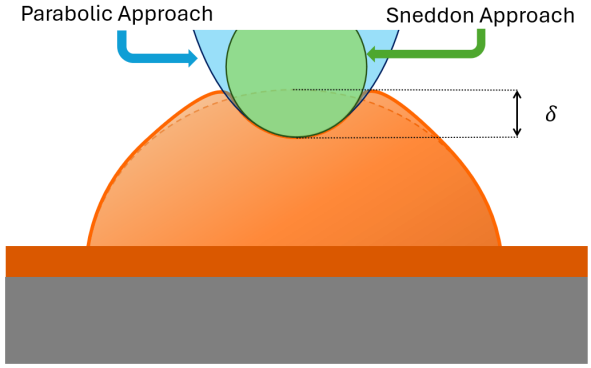

Figure 2.5: Schematic representation of the contact profile for the parabolic and the spherical approximations, where δ in the indentation.

We then compared both methods and test if the parabolic approximation could be used for larger indentations. This was done twofold, first by simulating approach curves with the spherical approximation and fitting them with the parabolic approximation and secondly by calculating the Young's modulus of a random set of cells using both methods and assess the difference between the results.

For the simulating part, several approach curves were generated according to Eq.2.4 using different effective Young's modulus ($E_{spherical}$) and maximum indentation (δ_{max}) to see if there

is any correlation between this parameters and the calculated Young's modulus. The ideal Sneddon curves are then fitted with the parabolic approximation, as can be seen in Fig.2.6.

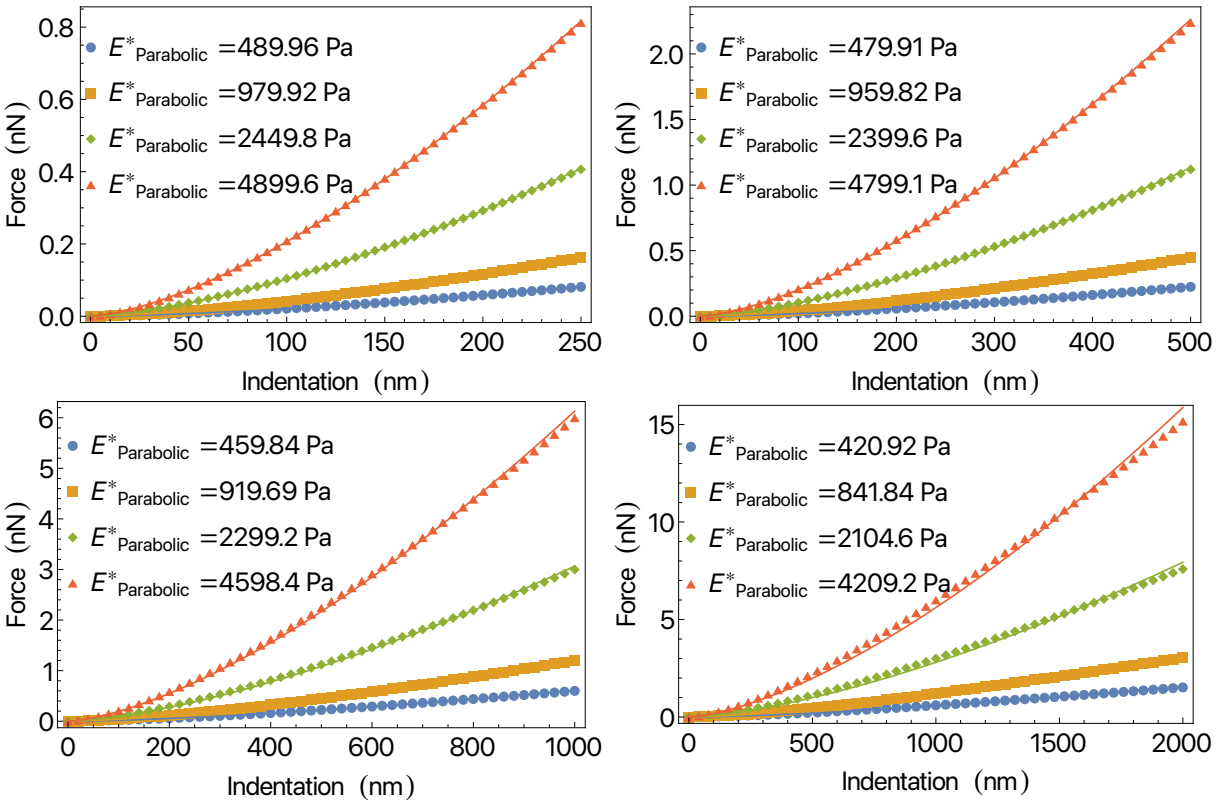

Figure 2.6: Force-indentation curves generated using the spherical approximation for constant tip radius (1000 nm) using $E^*_{spherical} = 500$ Pa for the blue circles, $E^*_{spherical} = 1000$ Pa for the yellow squares, $E^*_{spherical} = 2500$ Pa for the green diamonds and $E^*_{spherical} = 5000$ Pa for the red triangles and different maximum indentations, δ_{max}. The line of corresponding color are the fits obtained using the parabolic approximation. In the legend are the obtained values for $E^*_{parabolic}$ from the fit for the corresponding "dot" type. For better visual clarity only 51 points are plotted, for fitting purpose there is a point each 1 nm

From what can be seen in Fig.2.6 and from the coefficient of determination (R-Squared) (Independent of $E^*_{spherical}$, for $\delta_{max} = 250$ nm it is equal to 1 to the 5th decimal place, $\delta_{max} = 500$ nm it is equal to 1 to the 4th decimal place, $\delta_{max} = 1000$ nm it is equal to 1 to the 3rd decimal place, $\delta_{max} = 2000$ nm it is equal to 1 to the 3rd decimal place. In all cases, however there is a discrepancy between the obtained value and the theoretical value) the parabolic indentation is relatively robust until the indentation exceeds the spherical indenter radius. Although for indentations exceeding the indenter radius the fit is not completely useless and if fluctuations due to thermal noise are added, the discrepancy would probably not be noticed.

To better understand the relation between the two models and synthesise the information in Fig.2.6, we show the relation between $E^*_{spherical}$ used to generate the curves divided by the obtained $E^*_{Parabolic}$, $E_{frac} = E^*_{spherical}/E^*_{Parabolic}$ as a function of $E^*_{spherical}$ and δ_{max}.

Table 2.1: E_{frac} as a function of $E^*_{spherical}$ and δ_{max}. For this data indenter radius of 1000 nm, was kept constant.

$E^*_{spherical}$ (Pa) / δ_{max} (nm)	500	1000	2500	5000
250	1.021	1.021	1.021	1.021
500	1.042	1.042	1.042	1.042
1000	1.087	1.087	1.087	1.087
2000	1.188	1.188	1.188	1.188

From Table 2.1 one can see that E_{frac} is independent of $E^*_{spherical}$, only being depending on δ_{max}. To see if there is any relation between between E_{frac} and δ_{max} one plots E_{frac} for $E^*_{spherical}$ from 500 to 5000 in increments of 500 as a function of δ_{max} from 250 to 2000 in increments of 250, obtaining,

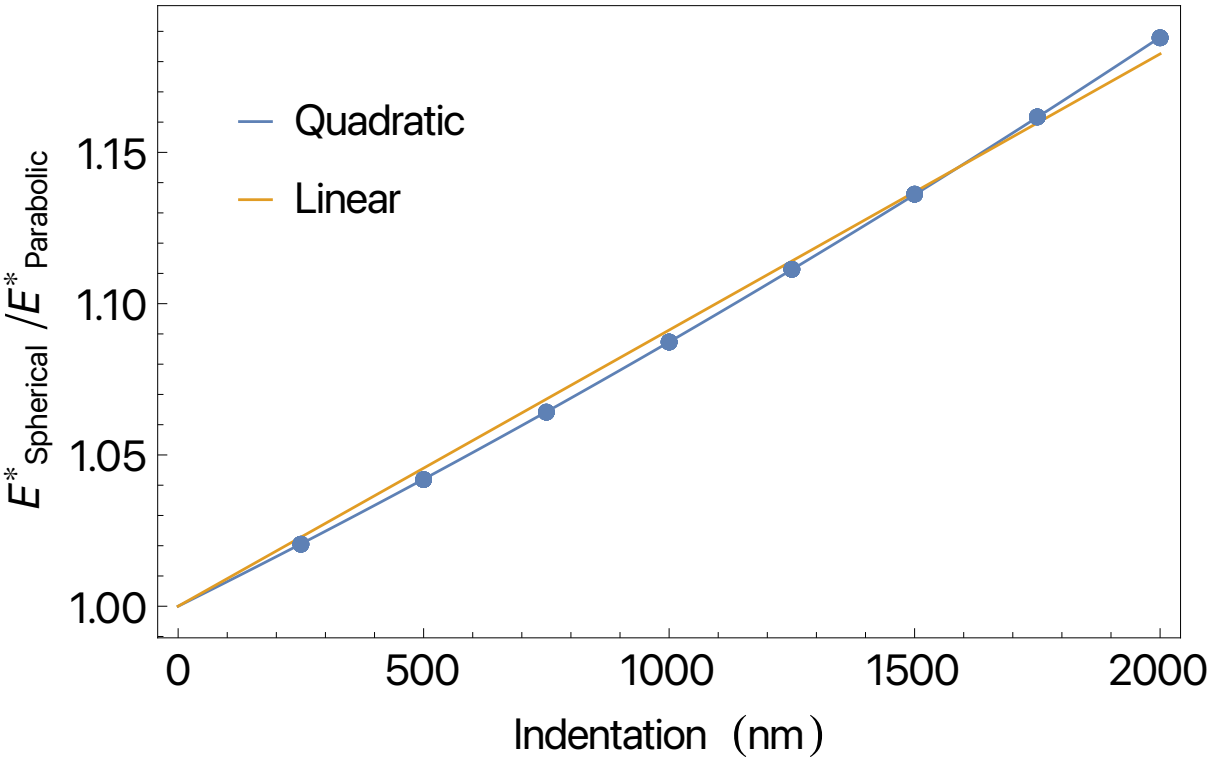

Figure 2.7: E_{frac} as a function of δ_{max} and $E^*_{spherical}$, for constant tip radius and the quadratic and linear fits to the data. This was done by simulating ideal curves for $E^*_{spherical}$ from 500 Pa to 5000 Pa in 500 Pa intervals, similarly, and for each of those values δ_{max} from 250 nm to 2000 nm in 250 nm intervals. As can be seen in Table 2.1 for the same δ_{max} all the value overlap.

Fig.2.7 shows the overlap of the data for different $E^*_{spherical}$ with the same δ_{max}, this data can be perfectly fitted to a 8th degree polynomial with constant term being equal to 1. To avoid a large expression, the data can be fitted instead to a parabolic function with an R-Squared equal to 1 to the 8th decimal place,

$$E_{frac}(\delta_{max}) = 1 + 8.06 \cdot 10^{-5}\delta_{max} + 6.69 \cdot 10^{-9}\delta^2_{max} \tag{2.5}$$

When fitting to a linear function, plotting it with the data one can clearly see that, although the R-Squared value is not small, it is equal to 1 to the 5th decimal place, but the fit is

significantly worst, as shown in Fig.2.7.

The dependency on tip radius was also studied, for such, maintaining $E^*_{spherical}$ constant (500 Pa), and tip radius and δ_{max} were varied, this was done up to an indentation of twice the tip radius. This resulted in Fig.2.8,

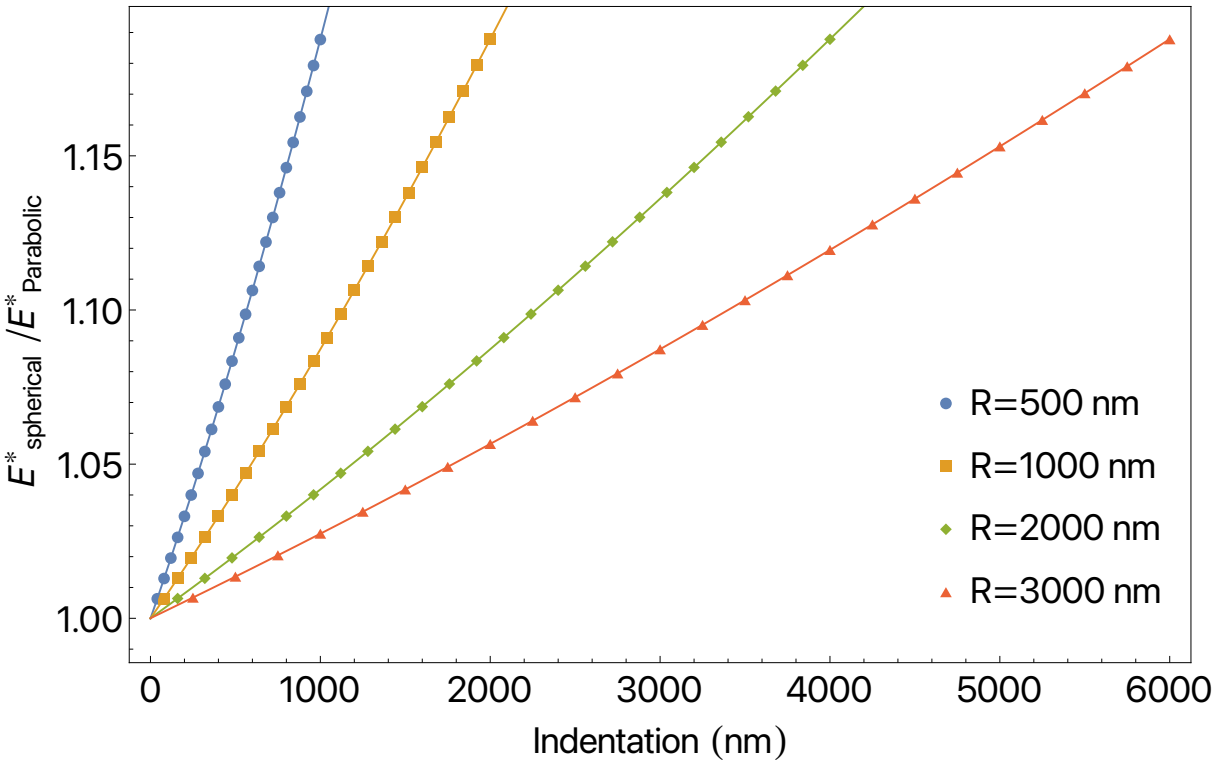

Figure 2.8: E_{frac} as a function of δ_{max} and tip radius. For better visual clarity only about 25 point are shown for each graph, but for fitting purpose there is a point every 1 nm

Fig.2.8 show the E_{frac} as a function of δ_{max} and tip radius, this shows no apparent singular relation like in Fig.2.7. If we instead plot E_{frac} as a function of $\delta_{max}/2R$, where $2R$ is the max simulated indentation, we obtain,

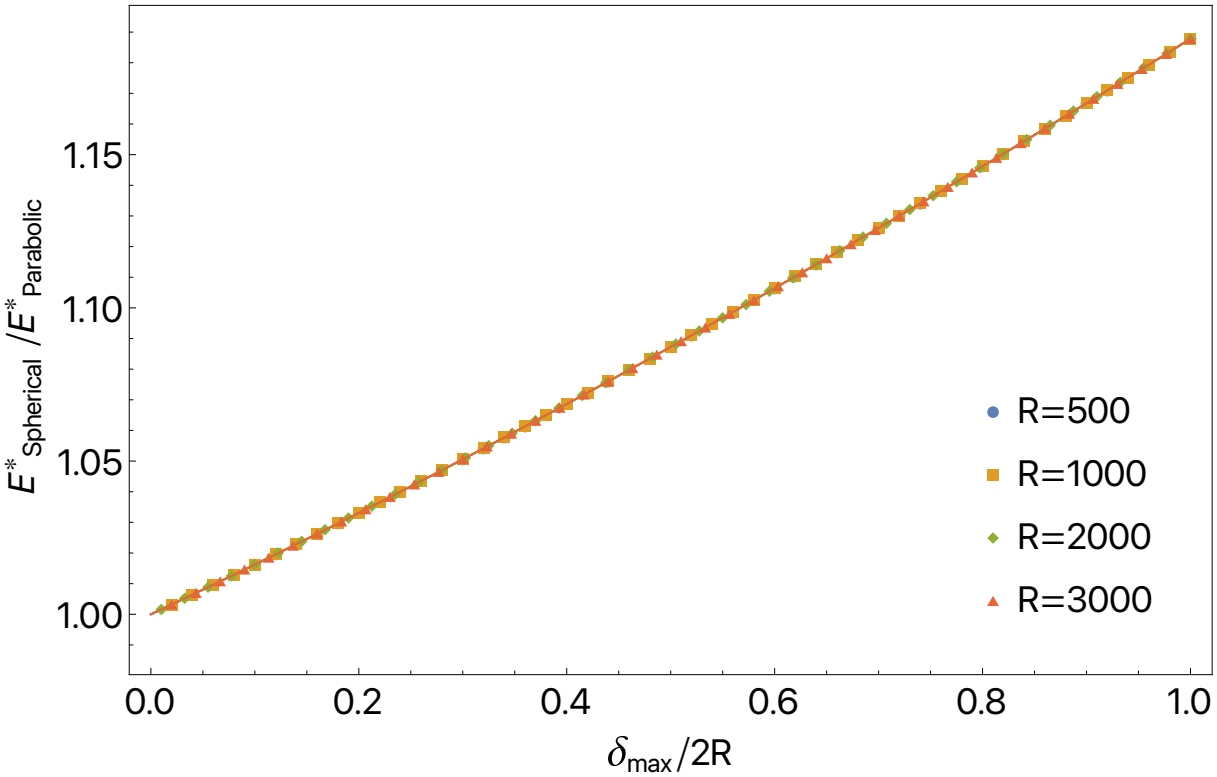

Figure 2.9: E_{frac} as a function of $\delta_{max}/2R$ for different R and the cubic fit.

In Fig.2.7 this data does not perfectly overlap. This leads to shits in the fit for different tip radius even with a 12th order polynomial. As such we used a 3rd order polynomial, the differences between tip radius are small, in the 4th decimal place for the constant term, in the 3rd decimal place for the linear term, in the 3rd decimal place for quadratic term and in the 4th decimal place for the cubic term. If instead we join all the data points and fit them, the 12th order polynomial as a R-Squared of 1 to the 9th decimal place and the 3rd order polynomial also has R-Squared of 1 to the 9th decimal place, this difference does not justify the usage of a more complex and larger polynomial function

$$E_{frac}(y) = 1 + 0.159y + 0.033y^2 - 4.09 \cdot 10^{-3}y^3 \tag{2.6}$$

where $y = \delta_{max}/2R$. This expression allows to correct the parabolic approximation. Thus we derive an easy to follow procedure for correctly computing data from spherical indentations.

When analysing a random set of 168 cells, 84 WT with 5921 points and 84 MT with 5704 points, using the spherical approximation and the Parabolic approximation. The maximum indentation for WT cells was $\delta_{max} = 969 \pm 478$ nm and for MT cells was $\delta_{max} = 764 \pm 396$ nm. This data is shown in Fig.2.10

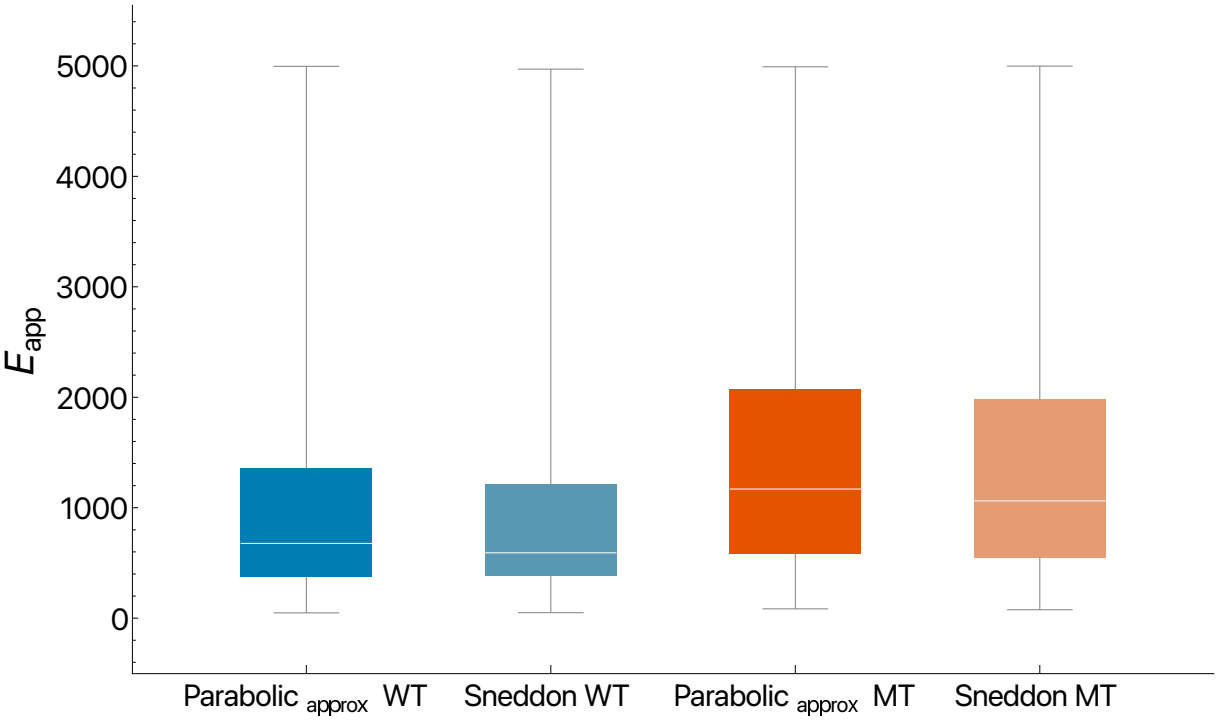

Figure 2.10: Apparent Young's modulus of WT and MT C6 cells calculated using the Parabolic approximation and the Sneddon model. The values are shown in $Median\ (Q_1, Q_3)$, for WT cells using the spherical approximation we obtained $E^* = 592\ (383, 1207)$ Pa for the Parabolic approximation $E^* = 677\ (374, 1557)$ Pa was obtained. For MT cells using the spherical approximation we obtained $E^* = 1062\ (548, 1980)$ Pa for the Parabolic approximation $E^* = 1169\ (589, 274)$ Pa.

As can be seen in Fig.2.10 and contrary to what is shown on Table 2.1 for a set of real data the spherical approximation gives lower results when compared to the Parabolic approximation. The relation of E^* for the spherical approximation divided by E^* for the parabolic approximation is for this set of WT cells 0.87, for this set of MT cells is 0.91. We could not come up with any justification for this difference between predicted and experimental behaviour. This further cements the complexity of measuring mechanical properties of living cells.

Due to the fact that the difference between models is $\sim 10\%$, that the Parabolic approximation requires less time to compute. For this work the Parabolic approximation will be used.

2.3.3 Calculating Young's modulus in approach and retract Curves

In most publications [192, 193, 194, 195] using AFM F-V methodology only the approach part of the curve is used to fit the Hertzian model. If we look at micro-indentation studies, which are similar to AFM F-V measurements, one of the most used methodologies [196] and its advances [197], uses both the approach and retract curve, stating that using the retract curve can facilitate the analysis of the data[197]. In the approach/loading phase it is assume that the deformations occurring are both elastic and plastic, however for the retract/unloading phase we assume that only elastic phenomena happen. We will use the same reasoning to apply this methodology to cells, doing so we will be ignore cell dynamics, which are highly complex and might have yet unknown effects on the measurements.

We observed that the Young's modulus from the approach and retract curve were in most cases different but of the same order. This shows us that the method is robust, as similar

values are obtained from different measurements and also that material isn't fully elastic as the measurements are not equal meaning plastic and/or viscoelastic processes might have happened. A slight caveat to this argument is that the AFM piezo electrics also suffer from hysteresis, which might also contribute to the difference between the approach and retract Young's modulus. This effect is very hard to measure, as it depends on the previous loading history of the piezo, thus, it is different for each individual measurement.

2.4 Calculating viscoelasticity

To calculate viscoelastic parameters a modified SLS model was solved. The SLS was modified in such a way that it would take into consideration the change in contact area as a function of the applied force, to the best of our knowledge this was never done using the procedure we now describe. In this modified SLS model the stress, σ, is swapped for force, F and the strain, ε, is swapped by the strain applied using a sphere for the Hertz contact models, $\frac{4}{3}\sqrt{R}\delta^{3/2}$,

$$F + \tau\dot{F} = \frac{4}{3}\sqrt{R}\tau(E_1 + E_2)\dot{\delta}^{3/2} + \frac{4}{3}\sqrt{R}E_1\delta^{3/2}, \tag{2.7}$$

where E_1, E_2, τ are the same as in the SLS model, Eq.1.1, F is the force applied, R is the radius of the spherical indenter, and δ is the indentation.

Notice that in the quasi-static limit, the time derivatives become negligible and one recovers the Hertz contact relation. This new model ignores adhesion, which is compatible with measurements in liquid.

To simplify this differential equation, the indentation as a function of time, $\delta(t)$ was considered to be, in good approximation, linear. Eq.2.7 was solved using different constraints: for the approach phase the differential equation was solved assuming $F_{app}(t = 0) = 0$, and for the retract phase the differential equation was solved assuming that $F_{ret}(t = t_m) = F_{app}(t_m)$, where t_m (m for middle) is duration of the approach phase and F_{app} is the solution of Eq.2.7 for the approach phase. This results in:

$$F_{app}(t) = \frac{2}{3}a^{\frac{3}{2}}\sqrt{R}\left[\sqrt{t}\,(2E_1 t + 3E_2\tau) - 3E_2\tau^{\frac{3}{2}}F_D\sqrt{\frac{t}{\tau}}\right], \tag{2.8}$$

$$F_{ret}(t) = \frac{1}{3}e^{-\frac{t}{\tau}}\left(C_1(t) - C_1(t_m) + 2e^{-\frac{t_m}{\tau}}F_{app}(t_m) + C_2(t)\right), \tag{2.9}$$

where, a is the slope obtained from the linear fit of $\delta_{app}(t) = a\,t$ to the approach part of the indentation-time data, $\delta_{ret}(t) = a\,t_m - bt$ is the equation that will be fitted to the retract part of the indentation-time data, t_m is duration of the approach phase, F_D is the Dawson integral, Erf is the error function, E_1, E_2, τ are the parameters of (Eq.1.1) and

$$C_1(t) = 2e^{\frac{t}{\tau}}\sqrt{R\delta_{ret}(t)}(2E_1\delta_{ret}(t) - 3bE_2\tau), \tag{2.10}$$

$$C_2(t) = 3b^{\frac{3}{2}}\tau^{\frac{3}{2}}e^{\frac{\delta_{b0}}{b\tau}}E_2\sqrt{R\pi}(Erf(\gamma(t)) - Erf(\gamma(t_m))), \tag{2.11}$$

$$\gamma(t) = \left(\frac{b\tau}{\delta_{ret}(t)}\right)^{-\frac{1}{2}}. \tag{2.12}$$

It should be noted that the equations found for this model are equal to solving Ting's solution [198] as shown in *Efremov et a.l* [199] using the SLS model under the assumption of a linear indentation. But contrary to the model proposed in *Efremov et al.* [199] this type of approach allows for an analytical solution to the SLS equation.

Approximations

The error function and the Dawson integral are defined as $Erf(z) = \frac{2}{\sqrt{\pi}} \int_0^z e^{-t^2} dt$ and $F_D(x) = e^{-x^2} \int_0^x e^{y^2} dy$. Fitting data to an equation that contains either or both of these functions, can make the fit substantially harder. In a first approximation we removed the terms containing them, but to compensate for the lost of terms containing the error functions and the Dawson integral, a constant term, f_0, was added to both the equations. This term needs to be fitted but is equal in both equations. So Eq.2.8 and Eq.2.9 where approximated to,

$$F_{app}(t) = \frac{2}{3} a^{\frac{3}{2}} \sqrt{Rt}(2E_1 t + 3E_2\tau) + f_0, \tag{2.13}$$

$$F_{ret}(t) = \frac{1}{3} e^{-\frac{t}{\tau}} \left(C_1(t) - C_1(t_m) + 3e^{\frac{t_m}{\tau}} F_{app}(t_m) \right) + f_0, \tag{2.14}$$

with

$$C_1(t) = 2e^{\frac{t}{\tau}} \sqrt{R\delta_{ret}(t)}(2E_1\delta_{ret}(t) - 3bE_2\tau).$$

Excluding the error functions and fitting the equations above to force-time curves generated by discretization of Eq.2.8 and Eq.2.9, we observed that E_1 tends to be $\sim 5\%$ higher, E_2 and τ tends to be $\sim 10\%$ lower, than the values used to generate the force-time curves. For more accuracy one can and should use Eq.2.8 and Eq.2.9 at the cost of more computing time.

Calculating viscoelaticity parameters

To obtain the relevant viscoelastic parameters two methodologies were developed.

In the first method, a fit to the retract part of the force-time data is firstly done using Eq.2.14, then the parameters obtained from that fit are used in Eq.2.13. The second and possibly more complex method assumes a new function:

$$F(t) = \begin{cases} F_{app}(t) & \text{if } t < t_m \\ F_{ret}(t) & \text{if } t > t_m \end{cases}, \tag{2.15}$$

where t_m is the duration of the approach phase and F_{app} and F_{ret} are the functions defined in Eq.2.13 and Eq.2.14 respectively. The whole indentation-time data (the approach and retract parts need to be joined) is then fitted to Eq.2.15.

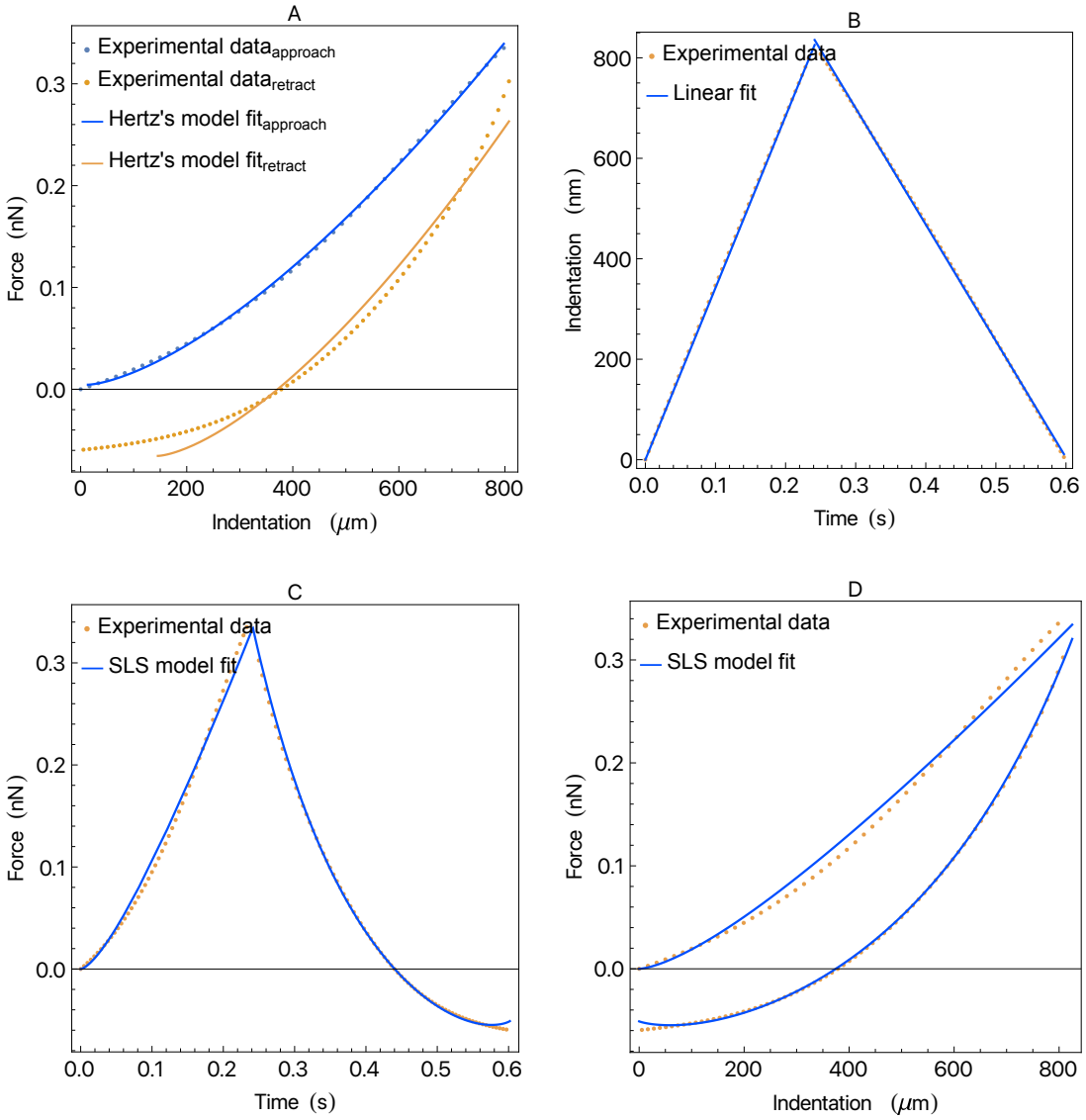

Figure 2.11: Measurements done a WT C6 Cell and fit using the SLS and Hertz models. (A) force-indentation curves and Hertz model fit, (B) indentation-time curves and linear fit for both the approach and retract part, (C) force-time curves and the SLS model fit (D) force-indentation curves and SLS model fit.

As the SLS model is fitted several *"questionable"* results have appeared. Such cases as curves in cells that are purely or almost purely either E_1 or E_2 or when $E_1 \gg E_2$ or $E_2 \gg E_1$.
The lesser "problematic" cases, which are mostly removed when data sets are made to be self consistent are, the case when E_2 is near or equal to 0, because the curve behave purely/mostly elastic, causing $E_{Hertz} \simeq E_1$, and due to the link between τ and E_2, τ is unreliable. In the case where E_1 is near or equal to 0 happens when τ is much greater than the indentation time, *i.e.* the measurement was done to quickly, this can be seen as, in the Maxwell representation of the SLS model, as the damper locking and the only sensing the spring attached to the dampener. In all cases where this happens, $E_{Hertz} < E_2$.

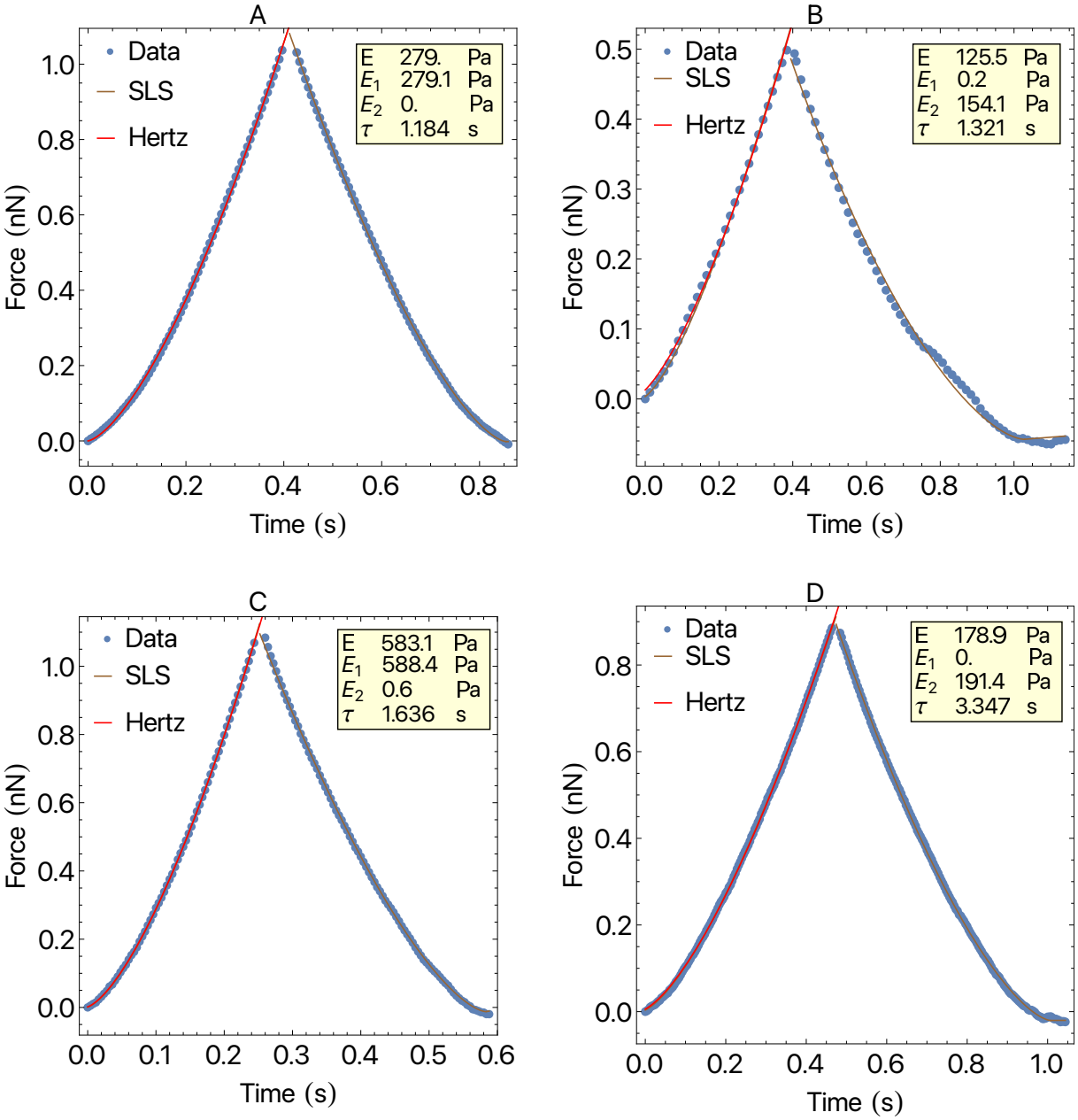

Figure 2.12: Examples of two problematic fits. (A) and (C) shows a fit where $E_2 \simeq 0$, meaning the cell behaved elastically and as expected, $E_{Hertz} \approx E_1$ and τ is a nonsense value. (B) and (D) shows the opposite case, where $E_1 \simeq 0$ and as predicted the measurement time was smaller then the characteristic time, $E_{Hertz} < E_2$, this happens for all cases where $E_2 \gg E_1$.

Interpretation of parameters

E_1 is measured when the deformation of the cell occurs very slowly, giving time for all the relaxations processes to occur. So, E_1 is a measurement of the long term stiffness of the material. In a cellular perspective, E_1 likely represents the contribution of the cytoskeleton after the reorientation and rearrangement resulting from the applied load. Hence, E_1 might be representative of the cytoskeleton integrity and organization.

E_2 is measured when the deformation occurs very rapidly, before any viscous relaxation occurs, capturing a stiffness that the material only exhibits at short time scales. In a cellular perspective, E_2 likely represents the contribution of cytoskeleton crosslinkers or/and cytoskeleton

filament stiffness and might also capture the cell cortex, which main function is to generate tension that allows cells to change shape [200], this may give an initial stiffness but relaxes over time as the cytoskeleton is rearranged. Hence, high E_2 might be representative of cells with high cortical tension and/or a highly crosslinked cytoskeleton.

η is a measure of the resistance of a fluid to a given deformation rate, it is also related to the viscous relaxation rate and to how quickly the material transitions from an instantaneous response to the relaxed state. In a cellular perspective, η is associated with the viscous behaviour of the cytoplasm, any other component that flows under stress or even the organelles flowing inside the cytoplasm. As such, η gives us a measurement of how the cell relaxes under stress, low η indicates easy flow, with quick relaxation, while high η indicates a viscous behaviour, with slower relaxation.

2.4.1 Contact point problem

In F-V measurements in air the contact point normally is easily identifiable by the jump-to-contact, a sudden displacement of the cantilever towards the sample due to the combined facts that the lever has a relatively low stiffness, and the *van der Waals* force increases very rapidly as distance decreases creating an instability. When measurements are done in liquid it is not that simple, as the *van der Waals* force responsible for jump-to-contact are screened by the liquid.

A simple solution to obtain the contact point in liquid is to discretise the *raw* curves, this is done by rounding to the nearest multiple of 3 times the standard deviation of the difference between the successive values of the deflection. Then we find the more frequent value, that value is then considered the curve's "floor". The contact point is then considered to be the point furtherest from the start from the curve's "floor", *i.e.* the point which has the larger value of piezo displacement in the curve's "floor". This method is a fast and simple way to find a contact point, although it is not without it's flaw, in some cases there is a miss calculations of the contact point, which causes over/under estimation of the Young's modulus, as can be seen in Fig. 2.13.

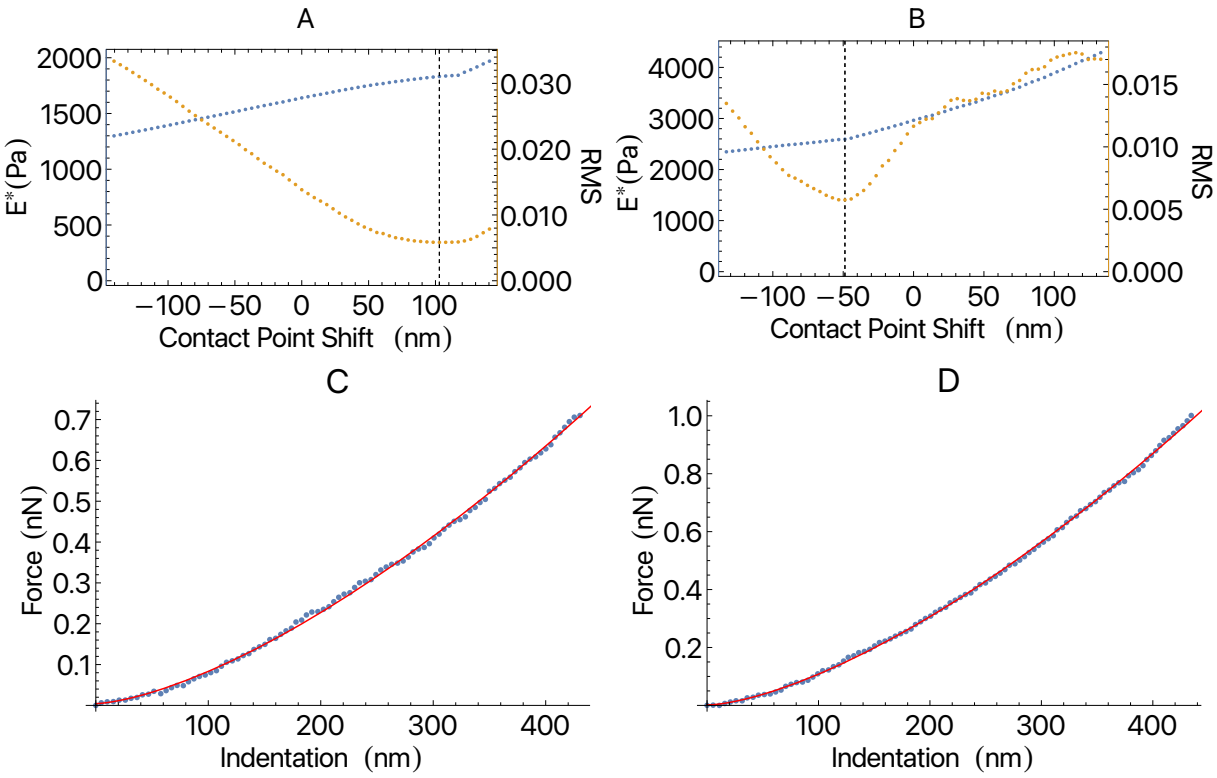

Figure 2.13: (A) and (B) show the effective Young's modulus, E^*, blue (y-axis left), and Root Mean Squared (RMS) of the fit, yellow (y-axis right), as a function of the contact point shift and the minimum of RMS (dashed line). (C) and (D) show the fit of approach curve for which the RMS is minimum.

As can be seen in Fig.2.13, the first assessment of the contact point is not perfect, *i.e.* the contact point for which RMS of the error is minimised, and an over/under estimation of the Young's modulus can be seen. This miss calculation of the contact point can be corrected by shifting the contact point some nm, this was done by changing the point assumed to be the contact point, or implementing more sophisticated algorithms for contact point detection. Any of these solutions increases the computing time of the calculations.

For this work shifting the contact point was used when for both the Hertizan Young's modulus and the SLS approximation of the cell, but the true contact point was chosen to be the one that minimizes the error for the SLS model, meaning that the contact point might not be ideal for Hertzian Young's modulus.

2.5 "Average" cell

Not only can we obtain the distributions in a mathematical sense, mean, median, standard deviation and quartiles of mechanical properties of a cell, we can also obtain the average distribution of mechanical properties and topography of the cell. To do it, first all the grids of values are converted to grids of $(x, y, value)$, where x and y are the position measured in μm. Then the topography of the cells (assumed to be elliptical) are rotated and aligned in such way that their semi minor and semi major axis overlap with each other and that the center of the cell is at $(0, 0)$. The map of mechanical properties of the cell is limited to a distance of 10 μm or 15 μm in the direction of both elipse axis, as C6 cells are about 20 μm in diameter. Then cell are checked

to see if the logarithm of the mechanical properties are within the acceptable limits, median ± 3 Standard deviations (the reason for using the logarithm will be explained in the next chapter). All the oriented cell grids are then joined in a list as (x, y, z_i), where x and y are the position in μm and z_i are the properties being analysed, topography, Young's modulus, etc. Following (x, y) is swept to build an image, this is done by taking the median of all point in a circumference of radius of 3 μm.

In an idyllic world, this method would allow us to see a change in mechanical properties in the perinuclear area in MT cells due to the aggregation of IFs. This is highly improbable, as the orientation of the IF accumulation is not consistent and it is not yet clear if the accumulation of IF causes any change in the mechanical properties. Another information that is obtained from this averaging of the cell, is the average outline of cell properties. This is done for both the semi minor and semi major axis, and it helps to better visualise the distribution of cell properties and can be used to compare one cell type to other.

2.6 Measurements (protocol)

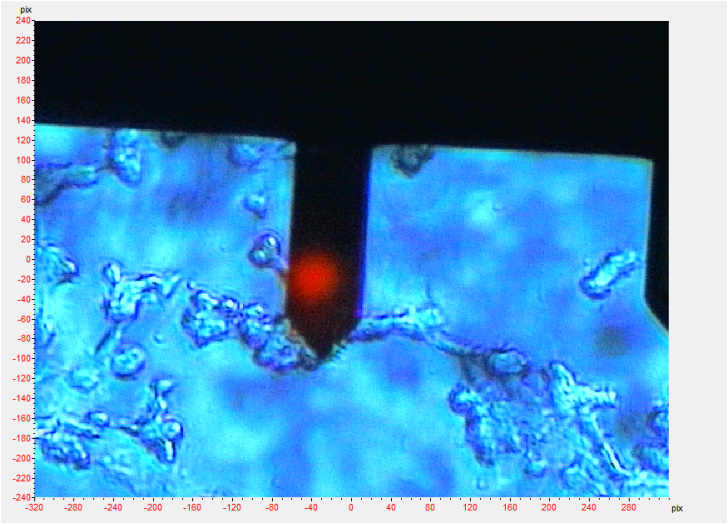

Figure 2.14: Image of C6 WT cells, obtained via de AFM camera showing clumps of cells and one cantilever from a HQ:NSC35/Al BS chip.

To apply all the methodologies exposed above one needs to first obtain data.

1. After all the basic tasks of AFM are done, *i.e.* turning the AFM and all the electronics on, placing a cantilever chip on the chip holder, the laser needs to be aligned to the cantilever tip, in air, and after putting the AFM in ACAFM (dynamic mode), a resonance curve is taken, to see if there is anything abnormal with the cantilever.

2. The cantilever and the AFM head are inserted in a small petri dish filled with water, the laser is realigned and another resonance curve is taken and the exciting frequency is set lower then the resonance frequency. This step can be skipped and done in the petri dish containing the cells and the cell's medium. This step is done in water to not waste time with the cells, as cells can't be kept for an unlimited time outside the controlled atmosphere.

3. The cantilever is lowered using the AFM screws, this is done until one notices the oscillation amplitude of the cantilever dropping suddenly, if the oscillation frequency drops to 0 one must raise the cantilever until the amplitude becomes what it was before the sudden drop, then the AFM is put into contact mode.

4. Using the integrated AFM camera one locates a cell, and using the x-y micrometric screws, the cantilever tip is positioned in the centre of the cell.

5. Using the auto approach feature of the software, the cantilever is set at approximately 1 μm from the cell.

6. A test force-volume curve is done and the setpoint is adjusted so that its value is near the expected value of the contact point.

7. Test force-volume curves are done in the edges of the scannable space to see if it is a suitable location for a grid to be made

8. If it is a suitable location, a grid is started, if not, one retracts the cantilever tip, using the software's retract, and looks for another cell using the camera and the milimetric screws, repeating from point 4 onwards.

Following the measurement of a grid, a *Mathematica* [201] script is used to extract the grid, as explained previously. Using a script, that gives a rough topography of the grid from the force-volume curves, one checks the topography of what was measured. If one obtains a full cell or a partial cell which one is happy with, one retracts the cantilever tip, using the software's retract, and looks for another cell, repeating from point 4 onwards. If one obtains a partial cell which he is not happy with, one can use the AFM software to move the scanning area to try obtain the full cell, or the fullest he can with the range one has, repeating point 6 onwards. All this steps seem easy and intuitive, but doing them in a timely and correct manner (*i.e.* locating cells, placing the cantilever tip over the cell) requires practice, just the processes of measuring the cell takes about 10 min and as cells wither/die over time this processes needs to be as fast as possible.

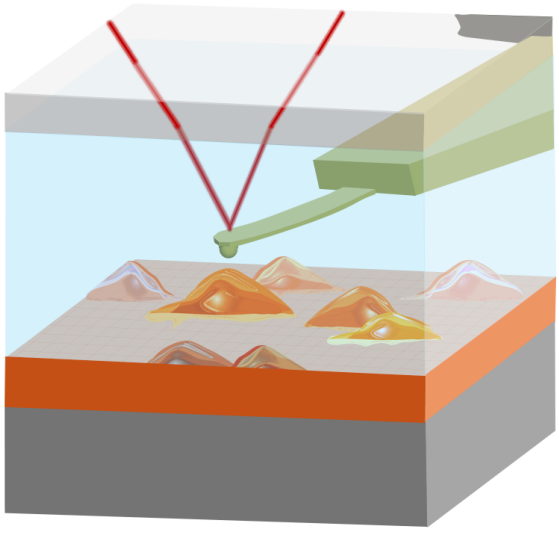

Figure 2.15: Schematic representation of AFM experimental setup measuring cells in liquid. Courtesy of Joana Nobre.

Chapter 3

Results

For all the cells analysed the measurements were obtained using a a PicoLE Molecular Imaging system from Agilent Technologies (Keysight Technologies, Inc., Santa Rosa, CA, USA), using a CP-qp-SCONT-SiO-A Nanoandmore cantilever, with nominal stiffness of 0.01 N/m and a nominal tip radius of 1 μm. A spherical indenter, of the same type shown in Fig.3.1, was used as it allows for a larger contact surface and lower applied pressure when compared to typical conical/piramidal indenter it also allows wholer cell measurements, not focusing on smaller details/heterogeneities in the cell.

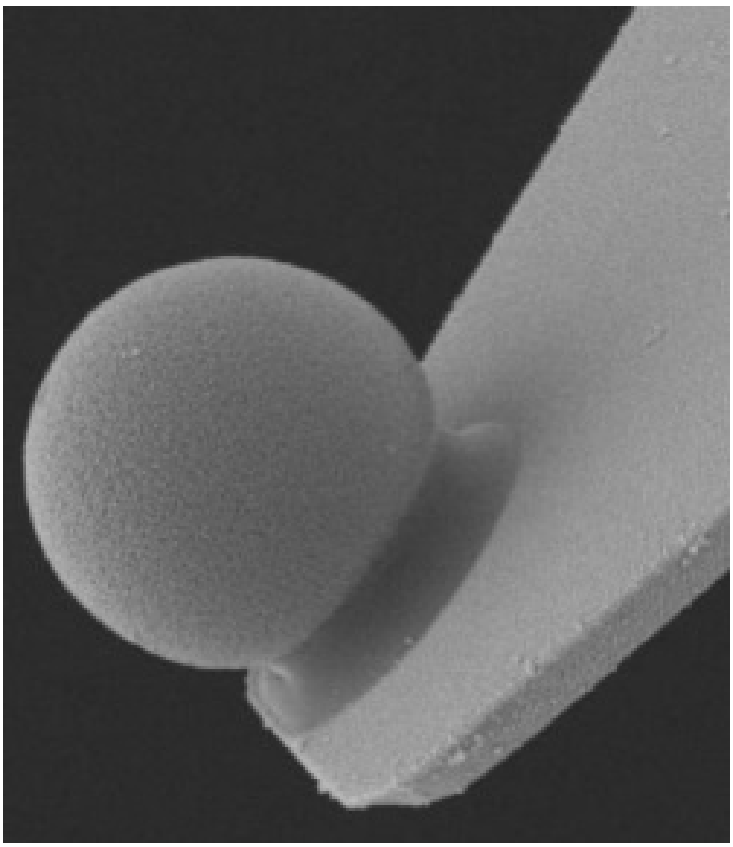

Figure 3.1: Scanning electron microscope image of the colloidal probe of a CP-qp-SCONT-SiO-A.

Typically a 16×16 grid of F-V curves was done (several 32×32 grids were also done), in a range between 15 and 40 μm. The AFM detector was calibrated by performing F-V curves on

a glass substrate.

3.1 Data analysis

To analyse the force curves, several steps are needed. Firstly the F-V grids are converted into topographies. This is done by attributing a value of z corresponding to a first estimation of the contact point obtained from the force-displacement curves for each (x, y) pixel. Hence a list of (x, y, z) is obtained. This is just an estimation of the cell profile and does not need to be very accurate, as cell height is of the order of 3 μm, and this is done solely for the purpose of identifying if a cell was measured, or in which part of the cell the measurements were done.

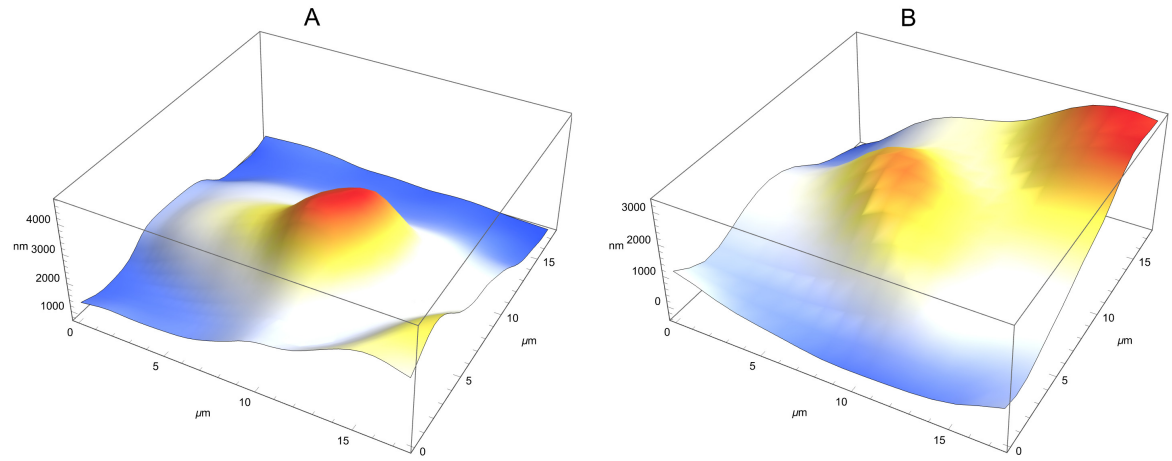

Figure 3.2: Example of topography obtained from F-V grid for 2 different cells, (A) WT cell and (B) a MT cell.

From the reconstructed topographies, cell like structures are manually selected by identifying a center point and the 2 semi axis of an elipse (cells are assumed to have an elliptical shape).

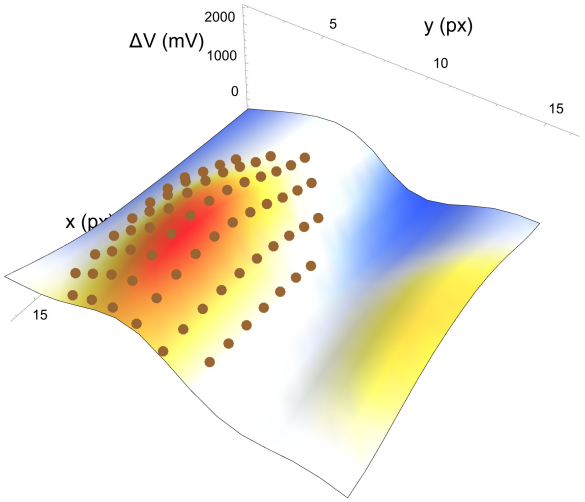

Figure 3.3: Example of the selection of the elipse on a cell with the cell topography obtained using F-V for a 16×16 grid.

The AFM software outputs grids where each pixel contains an approach and a retract curve (time (s) - scanner movement (nm) - deflection (V)), these curves are cut at the assumed contact point and after that, the approach curve is translated in such way that it starts at $(0, 0)$, the retract curve is translated equally and time is also *"translated"* in such way that it starts at 0. As we want to obtain usable/workable physical quantities, time (s) - scanner movement (nm) - deflection (V) cut curves are then converted using Eq.2.1 and Eq.2.2 into time (s) - indentation (nm) - force (nN), converting the curves from their original quantities to the new quantities that allows them to be used in the Hertz and SLS models.

The indentation-force part of this new data is then fitted to Eq.2.3, *i.e.*, both the approach and retract parts are fitted to obtain E_{app} and E_{ret} respectively. After that the time-indentation curves are fit to a linear equation, using the data from that fit, the time-force curves are then fitted to Eq.2.15 using Eq.2.13 and Eq.2.14 to obtain E_1, E_2 and τ. This script is run for all the curves in the grid, returning 5 grids with the parameters (E_{app} and E_{ret}; E_1; E_2; τ).

One issue that arrises from fitting the curves of F-V grids is that sometimes it is not possible to fit the curves, either by fault of the data or due to the fit not converging. When this is occurs, all the relevant parameters will be set to 0 as a way to indicate that the curves in that point weren't fitted. After the grid is complete, an algorithm will be employed to fix those points. This is done by doing a 1st order interpolation of the data making it an average of it's neighbouring points, after all 0 are fixed, a Gaussian filter is applied with radius 2 μm.

After all the parameter grids are corrected, a script selects the points that were previous marked as being a cell as shown in Fig.3.3. For each of these points a list is created that contains the value of the 5 parameters that were fitted, therefore for each cell the result is a list that contains the values for E_{app}, E_{ret}, E_1, E_2 and τ for each point. This nested list will be added to a list that contains all the previous analysed cells of that cell type (WT, MT, WFA, DMSO). After acquiring this data, statistical analysis can be done. Two types of analysis were done, one where the median of the parameters for each measured cell will be analysed as a set, named

"Per Cell" analysis; and another where the parameters of all points will be analysed as a set, named "Via Bulk" analysis.

Before any statistical treatment can be done, outliers are removed. For the Per Cell analysis, the data for each cell will be made self consistent, *i.e.* all the values are within 3 standard deviations of the median, this is done iteratively by removing all data points that are not within 3 standard deviations of the median. This is done by calculating a new median and repeating the process until the list doesn't change from one iteration to the other. Only after obtaining self consistency the median value will be calculated. The set of data containing the medians will also go through the same process of being made self consistent, but instead of being the obtained values that are made self consistent it will be the logarithm of the obtained values. As the set of data of medians seems to follow a log-normal distribution, applying a logarithm to a log-normal distribution converts it into a normal distribution and data set self consistency as was explained requires that the data is distributed according to a normal distribution. For the Via Bulk analysis, similarly to what was done with the data set of medians, a logarithm will be applied to the data set of all points, and the logarithm of the data set of all points will be made self consistent. To obtain the real distribution of the data sets, the data set of logarithm of values is exponentiated.

3.2 Mechanical properties of a single cell

The first question we address is: how are the mechanical properties distributed in a single cell? We have considered the possibility that these distributions are either normal or log-normal distributions. As both normal and log-normal distribution appear in nature. Normal distributions arise from many small independent factors adding together, on the other hand, log-normal distributions arise from many small independent factors multiplying together. To see how the mechanical properties are distributed in a cell, the mechanical properties were normalised (divided by their median value), this makes it so all the data from single cells can be compared to each other cell, independent of original values. Doing this for all the points that are selected as a cell, and without any sort of filtering (the software used to plot the histograms hide outliers for a better viewing, but the outcome would be the very similar) results in:

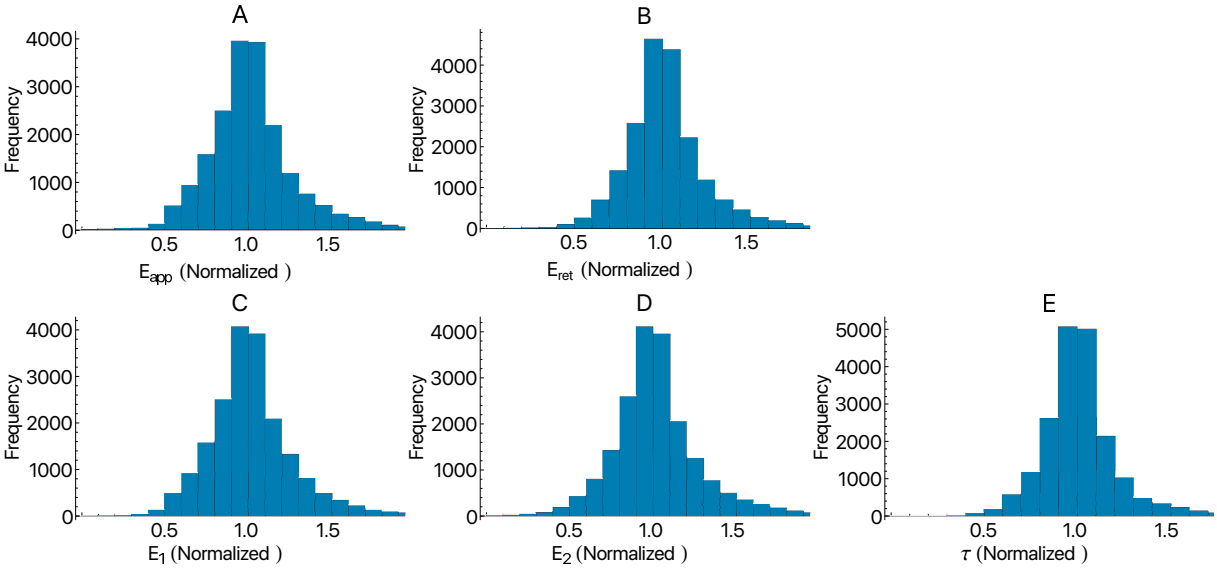

Figure 3.4: Normalised values obtained from the DMT and SLS model fit for WT cells, (A) Young's modulus for the approach curve, (B) Young's modulus for the retract curve, (C) E_1, (D) E_2, (E) relaxation time, τ.

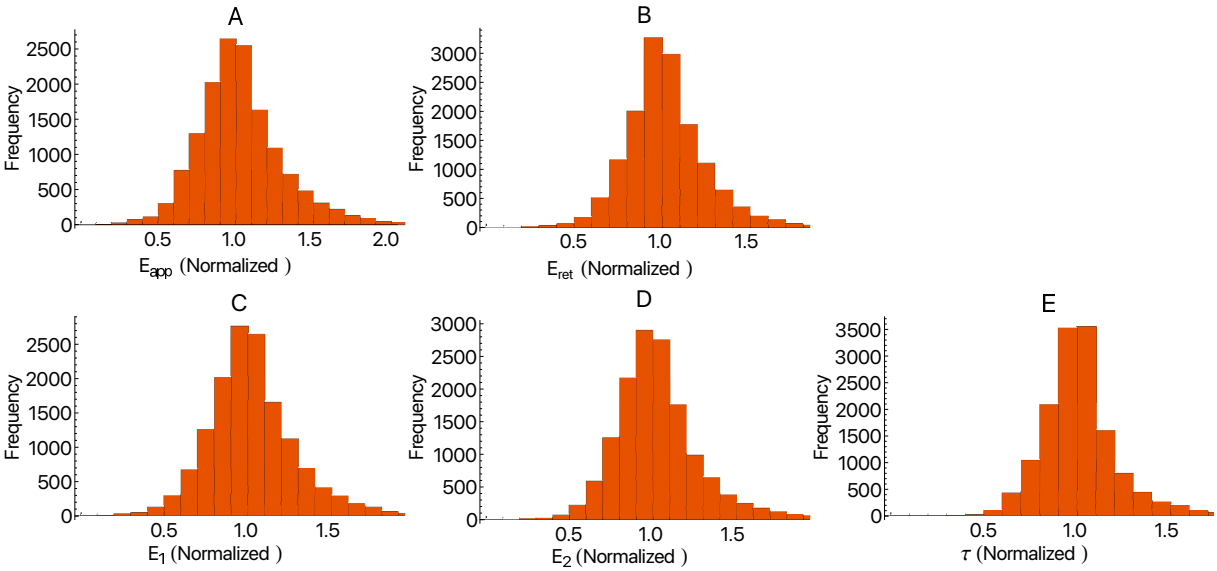

Figure 3.5: Normalised values obtained from the DMT and SLS model fit for MT cells, (A) Young's modulus for the approach curve, (B) Young's modulus for the retract curve, (C) E_1, (D) E_2, (E) relaxation time, τ.

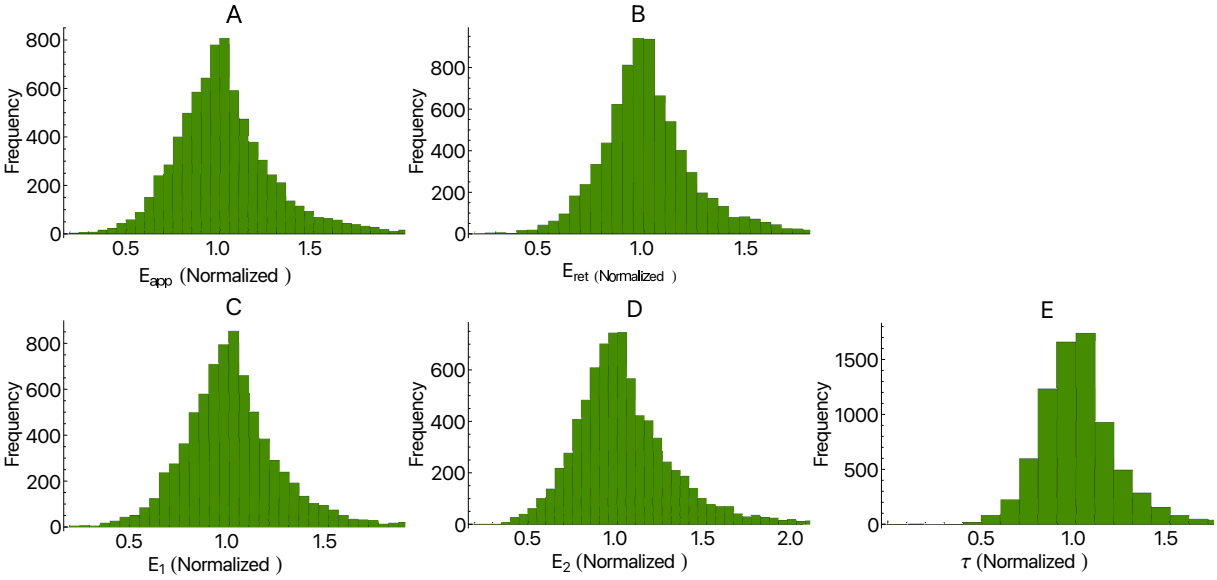

Figure 3.6: Normalised values obtained from the DMT and SLS model fit for WT cells cultured in WFA, (A) Young's modulus for the approach curve, (B) Young's modulus for the retract curve, (C) E_1, (D) E_2, (E) relaxation time, τ.

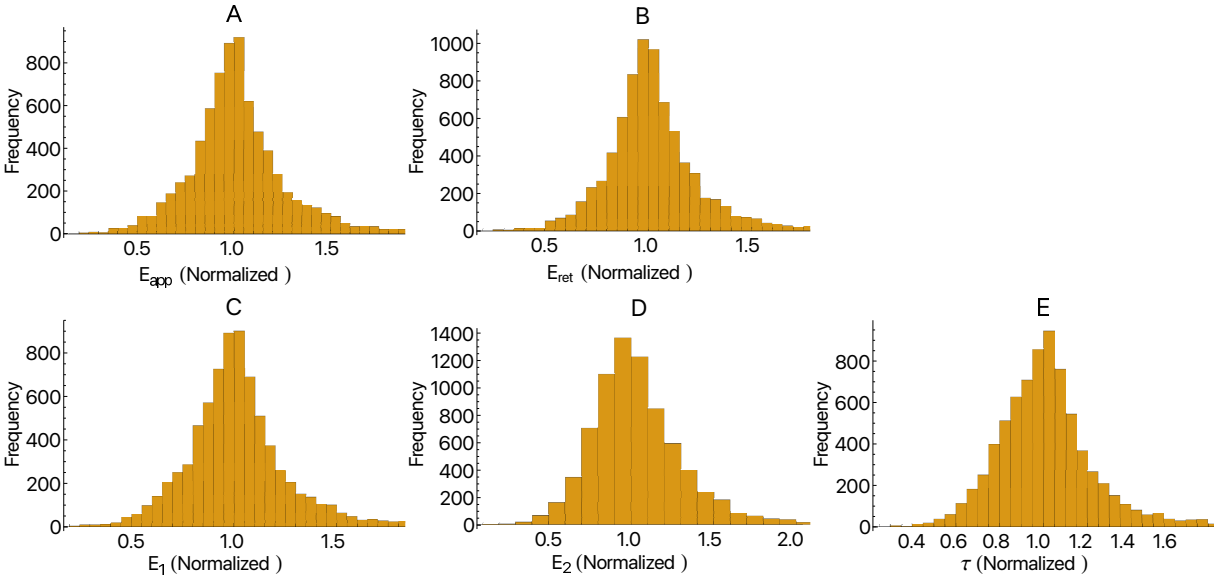

Figure 3.7: Normalised values obtained from the DMT and SLS model fit for WT cells cultured in DMSO, (A) Young's modulus for the approach curve, (B) Young's modulus for the retract curve, (C) E_1, (D) E_2, (E) relaxation time, τ.

As can be clearly seen from Fig.3.4, Fig.3.5, Fig.3.6 and Fig.3.7 the mechanical properties within a single cell follow a normal distribution. This means when making the cell self consistent, there is no need to apply a logarithm to the data. This, as we will see, will not be the case for the distribution of median elastic or viscoelastic properties.

Table 3.1: Median values for the standard deviation of measurements divided by the median of measurements for the Per Cell analysis.

	E_{app}	E_{ret}	E_1	E_2	τ
WT	0.208	0.160	0.203	0.201	0.150
MT	0.213	0.154	0.207	0.196	0.151
WFA	0.227	0.180	0.209	0.217	0.172
DMSO	0.226	0.184	0.204	0.239	0.178

From Table 3.1 we can see that the values tend to be similar to each other for a given mechanical properties and as this values are a measurement of dispersion, one would assume that the dispersion of all measurements should be similar.

3.3 Mechanical properties of a cell set

Following the distribution of mechanical properties of a single cell, we explored the distribution of mechanical properties of a cell set. As previously we consider the possibility that these distributions are both normal or log-normal. As we will see, the distribution of elastic and viscoelastic properties within a set of cells follows a log-normal distribution, as such the data will be presented as $Median\ (Q_1, Q_3)$.

3.3.1 Per Cell analysis

In the Per Cell analysis, we consider the median of the mechanical properties of a single cell as a value for the distribution.

From the 404 WT measurements, only 377 passed the tests and were assumed to be cells and were analysed. From these 349 cells, after obtaining self consistent list, we obtain $E_{app} = 533\ (308, 900)$ Pa, $E_{ret} = 556\ (320, 911)$ Pa, $E_1 = 430\ (243, 734)$ Pa, $E_2 = 284\ (164, 511)$ Pa, $\tau = 0.11\ (0.09, 0.16)$ s, $\eta = 36\ (25, 50)$ Pa·s.

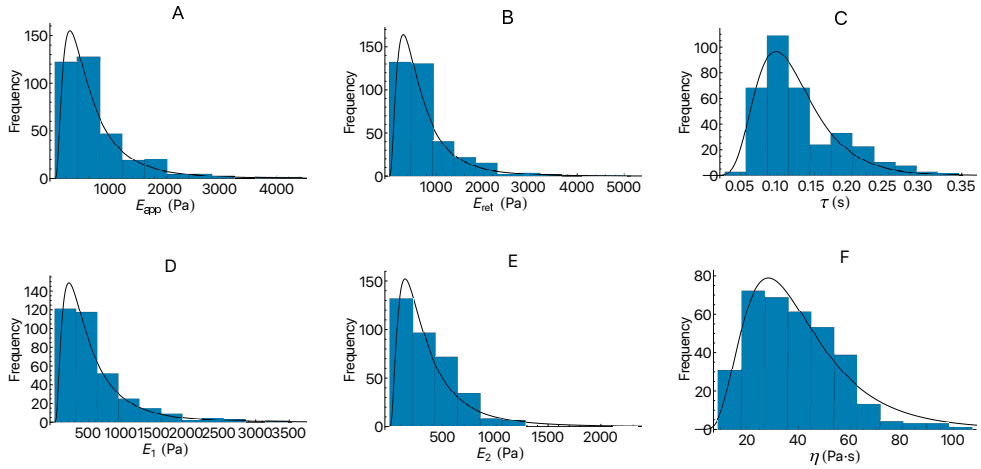

Figure 3.8: Values obtained from the DMT and SLS model fit for WT cells with their corresponding log-normal distributions. (A) Young's modulus for the approach curve, (B) Young's modulus for the retract curve, (C) relaxation time, τ, from the SLS model, (D) E_1 from the SLS model, (E) E_2 from the SLS model, (F) viscosity, η, from the SLS model.

From the 315 MT measurements, only 287 passed the tests and were assumed to be cells

and were analysed. From these 263 cells, after obtaining self consistent list, we obtain E_{app} = 541 (306, 1020) Pa, E_{ret} = 568 (309, 1020) Pa, E_1 = 429 (247, 846) Pa, E_2 = 338 (289, 561) Pa, τ = 0.10 (0.08, 0.13) s, η = 36 (24, 52) Pa·s.

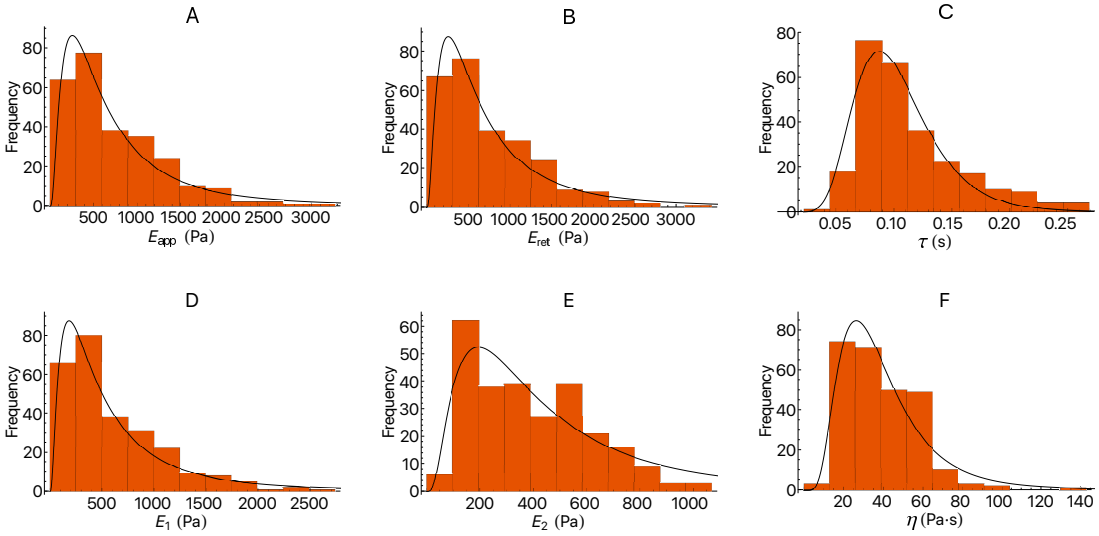

Figure 3.9: Values obtained from the DMT and SLS model fit for MT cells with their corresponding log-normal distributions. (A) Young's modulus for the approach curve, (B) Young's modulus for the retract curve, (C) relaxation time, τ, from the SLS model, (D) E_1 from the SLS model, (E) E_2 from the SLS model, (F) viscosity, η, from the SLS model.

From the 159 WFA measurements, only 151 passed the tests and were assumed to be cells and were analysed. From these 124 cells, after obtaining self consistent list, we obtain E_{app} = 535 (413, 816) Pa, E_{ret} = 560 (425, 823) Pa, E_1 = 404 (311, 654) Pa, E_2 = 444 (357, 532) Pa, τ = 0.09 (0.08, 0.11) s, η = 41 (36, 47) Pa·s.

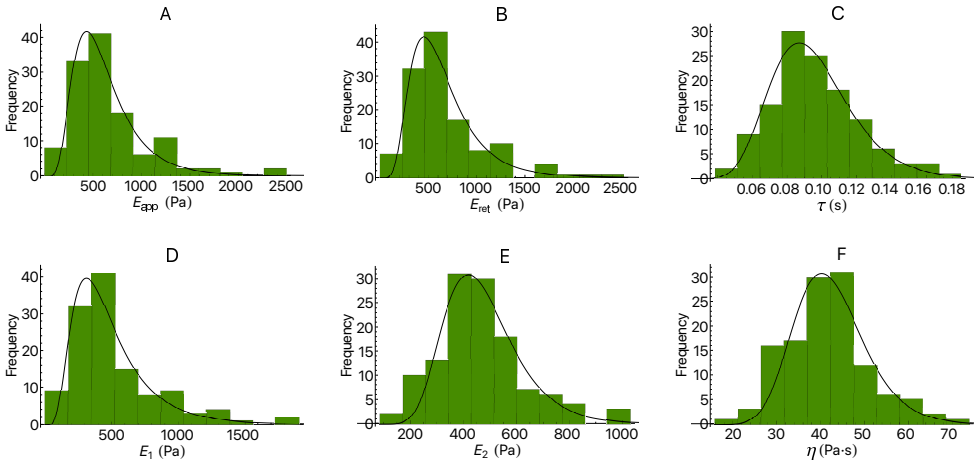

Figure 3.10: Values obtained from the DMT and SLS model fit for WT cells cultured in WFA with their corresponding log-normal distributions. (A) Young's modulus for the approach curve, (B) Young's modulus for the retract curve, (C) relaxation time, τ, from the SLS model, (D) E_1 from the SLS model, (E) E_2 from the SLS model, (F) viscosity, η, from the SLS model.

From the 139 DMSO measurements, only 130 passed the tests and were assumed to be cells and were analysed. From these 101 cells, after obtaining self consistent list, we obtain E_{app} = 383 (285, 593) Pa, E_{ret} = 386 (303, 624) Pa, E_1 = 309 (236, 457) Pa, E_2 = 347 (257, 435) Pa,

$\tau = 0.11\ (0.10, 0.14)$ s, $\eta = 38\ (32, 46)$ Pa·s.

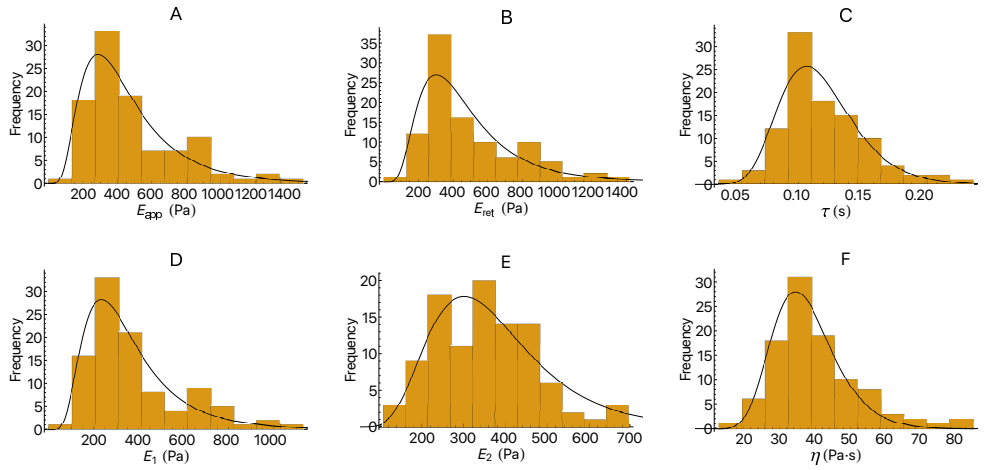

Figure 3.11: Values obtained from the DMT and SLS model fit for WT cells cultured in DMSO with their corresponding log-normal distributions. (A) Young's modulus for the approach curve, (B) Young's modulus for the retract curve, (C) relaxation time, τ, from the SLS model, (D) E_1 from the SLS model, (E) E_2 from the SLS model, (F) viscosity, η, from the SLS model.

Table 3.2: Values obtained for the mechanical properties for the Per Cell analysis for WT, MT, WT cells cultured in WFA and WT cells cultured in DMSO. Values are expressed as $Median\ (Q_1, Q_3)$.

Hertz / Cell type	E_{app} (Pa)	E_{ret} (Pa)
WT	533 (308, 900)	556 (320, 911)
MT	541 (306, 1020)	568 (309, 1020)
WFA	535 (413, 816)	560 (425, 823)
DMSO	383 (285, 593)	386 (303, 624)

SLS / Cell type	E_1 (Pa)	E_2 (Pa)	τ (s)	η (Pa·s)
WT	430 (243, 734)	284 (164, 511)	0.11 (0.09, 0.16)	36 (25, 50)
MT	429 (247, 846)	338 (289, 561)	0.09 (0.08, 0.13)	36 (24, 52)
WFA	404 (311, 654)	444 (357, 532)	0.09 (0.07, 0.11)	41 (36, 47)
DMSO	309 (236, 457)	347 (257, 435)	0.11 (0.10, 0.14)	38 (32, 46)

3.3.2 Via Bulk analysis

In the Via Bulk analysis, we consider the mechanical properties obtained from each curve as a value for the distribution.

From the measurements on WT we obtained 19666 data points, from this 18957 points passed the pre-selection and selection process. From these, we obtained $E_{app} = 575\ (352, 964)$ Pa, $E_{ret} = 601\ (369, 978)$ Pa, $E_1 = 471\ (283, 799)$ Pa, $E_2 = 283\ (172, 486)$ Pa, $\tau = 0.12\ (0.09, 0.15)$ s, $\eta = 36\ (23, 49)$ Pa·s.

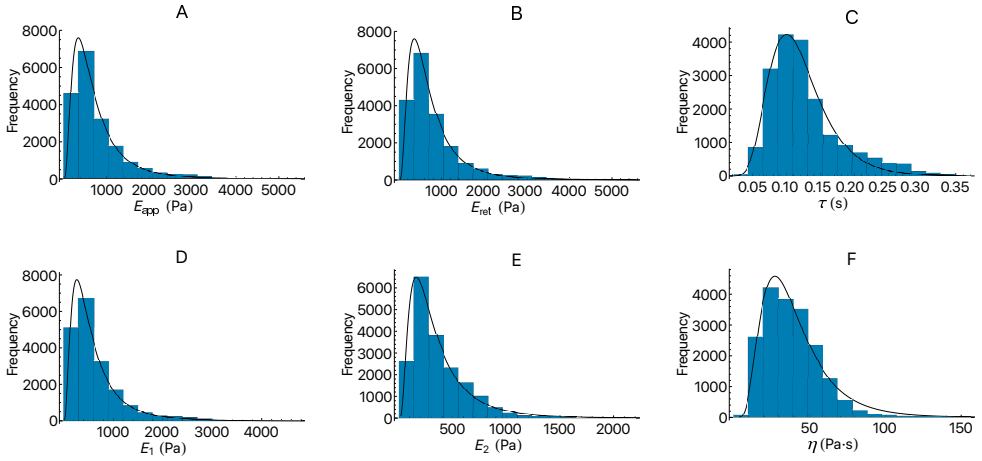

Figure 3.12: Values obtained from the DMT and SLS model fit for WT cells with their corresponding log-normal distributions. (A) Young's modulus for the approach curve, (B) Young's modulus for the retract curve, (C) relaxation time, τ, from the SLS model, (D) E_1 from the SLS model, (E) E_2 from the SLS model, (F) viscosity, η, from the SLS model.

From the measurements on MT we obtained 14641 data points, from this 14034 points passed the pre-selection and selection process. From these, we obtained $E_{app} = 620\ (345, 1059)$ Pa, $E_{ret} = 637\ (361, 1064)$ Pa, $E_1 = 497\ (270, 870)$ Pa, $E_2 = 366\ (237, 558)$ Pa, $\tau = 0.09\ (0.08, 0.12)$ s, $\eta = 36\ (23, 51)$ Pa·s.

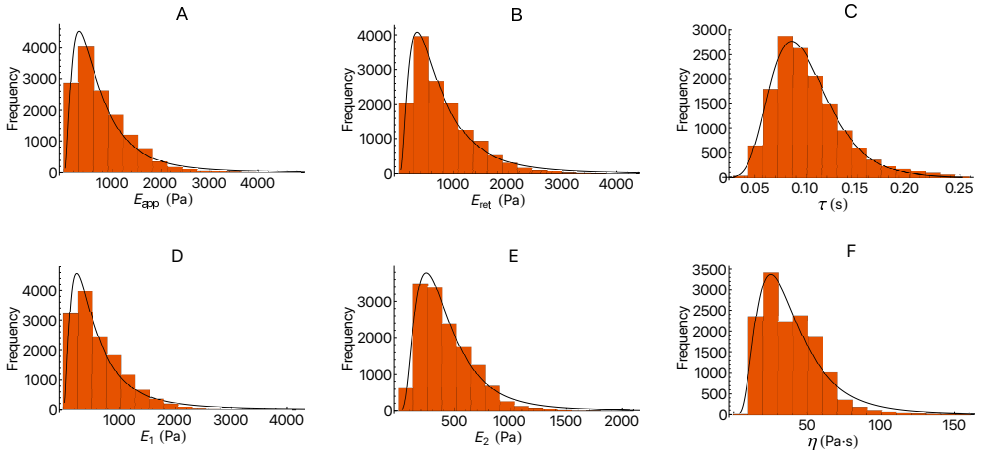

Figure 3.13: Values obtained from the DMT and SLS model fit for MT cells with their corresponding log-normal distributions. (A) Young's modulus for the approach curve, (B) Young's modulus for the retract curve, (C) relaxation time, τ, from the SLS model, (D) E_1 from the SLS model, (E) E_2 from the SLS model, (F) viscosity, η, from the SLS model.

From the measurements on WFA we obtained 7711 data points, from this 7189 points passed the pre-selection and selection process. From these, we obtained $E_{app} = 574\ (402, 840)$ Pa, $E_{ret} = 587\ (422, 843)$ Pa, $E_1 = 436\ (309, 655)$ Pa, $E_2 = 457\ (341, 577)$ Pa, $\tau = 0.09\ (0.07, 0.11)$ s, $\eta = 42\ (35, 49)$ Pa·s.

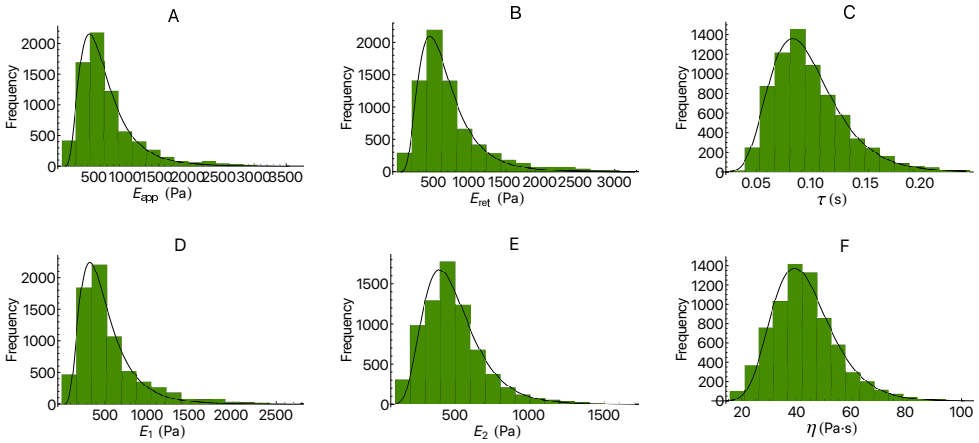

Figure 3.14: Values obtained from the DMT and SLS model fit for WT cells cultured in WFA with their corresponding log-normal distributions. (A) Young's modulus for the approach curve, (B) Young's modulus for the retract curve, (C) relaxation time, τ, from the SLS model, (D) E_1 from the SLS model, (E) E_2 from the SLS model, (F) viscosity, η, from the SLS model.

From the measurements on DMSO we obtained 7610 data points, from this 7070 points passed the pre-selection and selection process. From these, we obtain $E_{app} = 422\ (286, 676)$ Pa, $E_{ret} = 432\ (300, 694)$ Pa, $E_1 = 324\ (223, 514)$ Pa, $E_2 = 352\ (266, 469)$ Pa, $\tau = 0.11\ (0.09, 0.14)$ s, $\eta = 39\ (32, 48)$ Pa·s.

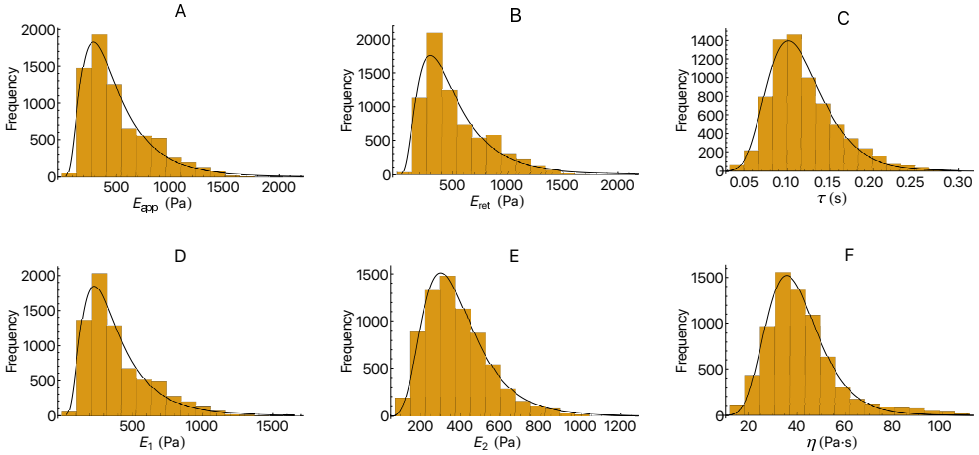

Figure 3.15: Values obtained from the DMT and SLS model fit for WT cells cultured in DMSO with their corresponding log-normal distributions. (A) Young's modulus for the approach curve, (B) Young's modulus for the retract curve, (C) relaxation time, τ, from the SLS model, (D) E_1 from the SLS model, (E) E_2 from the SLS model, (F) viscosity, η, from the SLS model.

Table 3.3: Values obtained for the mechanical properties for the Via Bulk analysis for WT, MT, WT cells cultured in WFA and WT cells cultured in DMSO. Values are expressed as $Median\ (Q_1, Q_3)$.

Hertz / Cell type	E_{app} (Pa)	E_{ret} (Pa)
WT	575 (352, 964)	601 (369, 978)
MT	620 (345, 1059)	637 (361, 1064)
WFA	574 (402, 840)	587 (422, 843)
DMSO	422 (286, 676)	432 (300, 694)

SLS / Cell type	E_1 (Pa)	E_2 (Pa)	τ (s)	η (Pa·s)
WT	471 (283, 799)	283 (172, 486)	0.12 (0.09, 0.15)	36 (23, 49)
MT	497 (270, 870)	366 (237, 558)	0.09 (0.08, 0.12)	36 (23, 51)
WFA	436 (309, 655)	457 (341, 577)	0.09 (0.07, 0.11)	42 (35, 49)
DMSO	324 (223, 514)	352 (266, 469)	0.11 (0.09, 0.14)	39 (32, 48)

3.4 Comparisons

3.4.1 Cell type comparison

In order to better visualise the differences/similarities in mechanical properties between the 4 cell types, their properties are shown together in box and whisker plots for both Per Cell and Via Bulk analysis.

Per Cell

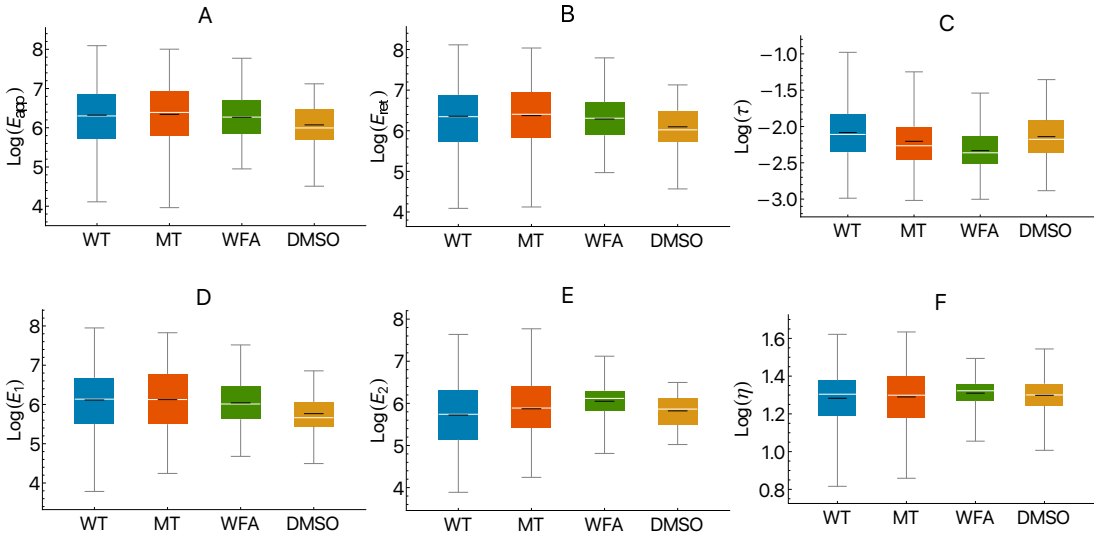

Figure 3.16: Logarithm of the measurements obtained from the SLS and DMT models for all cell types. (A) Young's modulus for the approach curve, (B) Young's modulus for the retract curve, (C) relaxation time from the SLS model, (D) E_1 from the SLS model, (E) E_2 from the SLS model, (F) viscosity, from the SLS model. The black line represents the mean value. WFA refers to the cells cultured in WFA as explained before, DMSO refers to the cells cultured in DMSO as explained before.

Via Bulk

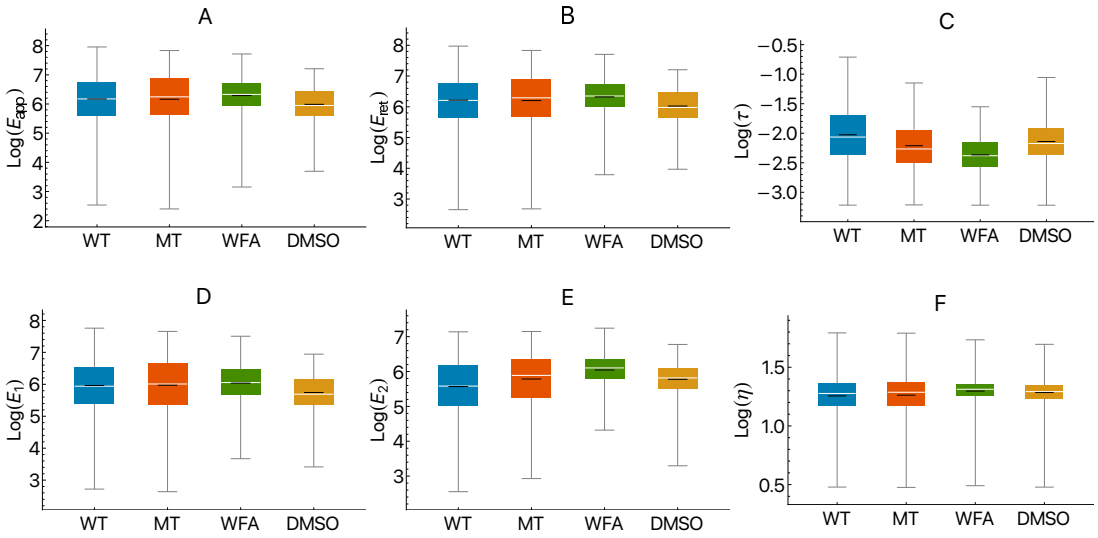

Figure 3.17: Logarithm of the measurements obtained from the SLS and DMT models for all cell types. (A) Young's modulus for the approach curve, (B) Young's modulus for the retract curve, (C) relaxation time from the SLS model, (D) E_1 from the SLS model, (E) E_2 from the SLS model, (F) viscosity, from the SLS model. The black line represents the mean value. WFA refers to the cells cultured in WFA as explained before, DMSO refers to the cells cultured in DMSO as explained before.

Analysing the data in the Per Cell and Via Bulk analysis had two objectives, firstly as a way to possible prevent *"trowing away"* work, as cells that are rejected due to their average value being outside the self consistent group might have some accepted measurements, this can also have a down side. As bad measurements that by random chance get the correct values will also be taken into consideration. Secondly to see if there was any difference in mechanical properties for both methods, from what can be seen in Table 3.2 and Table 3.3 the Via Bulk analysis resulted in larger values for all parameters. The main difference between the methods is that good/valid point in the Per Cell analysis are a property of the specific cell being analysed while in the Via Bulk method good/valid points are a property of the whole set of cells. One down side of the Via Bulk method is that independent of the number of points taken from a cell they are all treated equally, this can cause squeeing in the data. An hypothetical example, if we measured 1000 points on cells with stiffness above the true median and 500 points on cells with stiffness bellow the true median this would make our results larger then the true value. As such although the Via Bulk analysis as some upside, we consider that the downsides out weight them.

3.5 "Average" cell

After calculating all the mechanical properties we wished to see how they were distributed in the cell, this was done using the methodology explained before. For this analysis, the retract Young's modulus, E_{ret}, was not used as it is very similar to E_{app}.

3.5.1 Cell maps

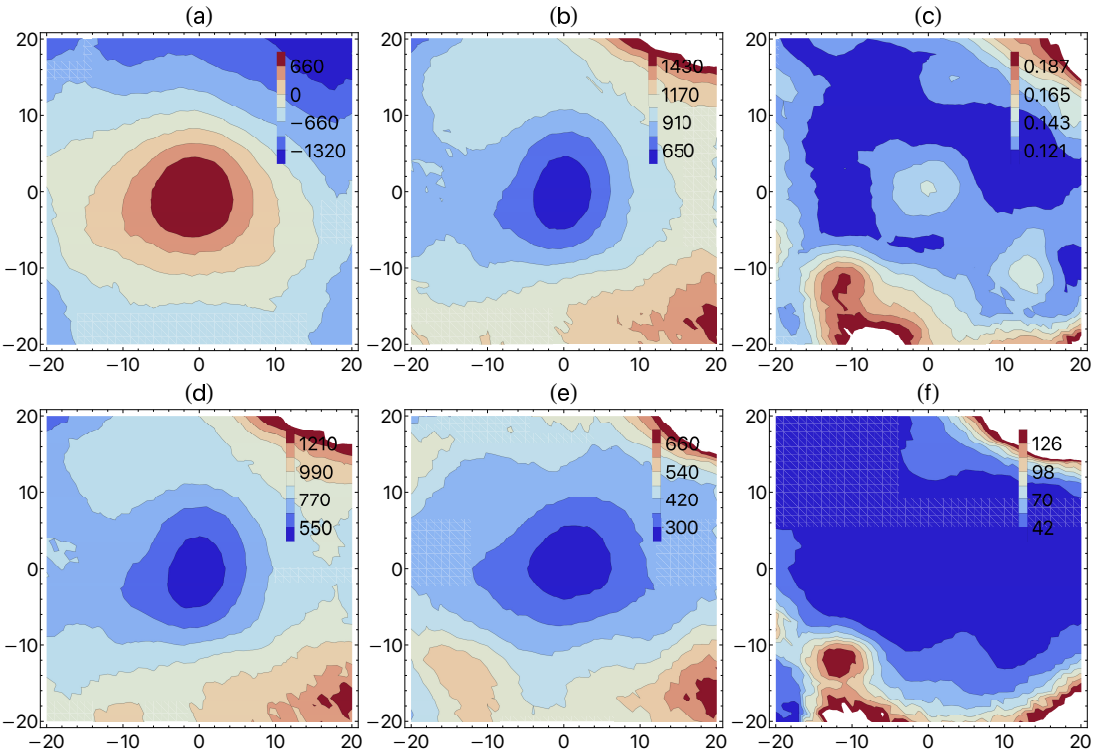

Figure 3.18: Average WT cell, this was calculated from 209 WT cells, (a), is the topography, (b) is the Approach Youngs modulus (E_{app}), (c), is τ, (d), is E_1, (e) is E_2 and (f) is η.

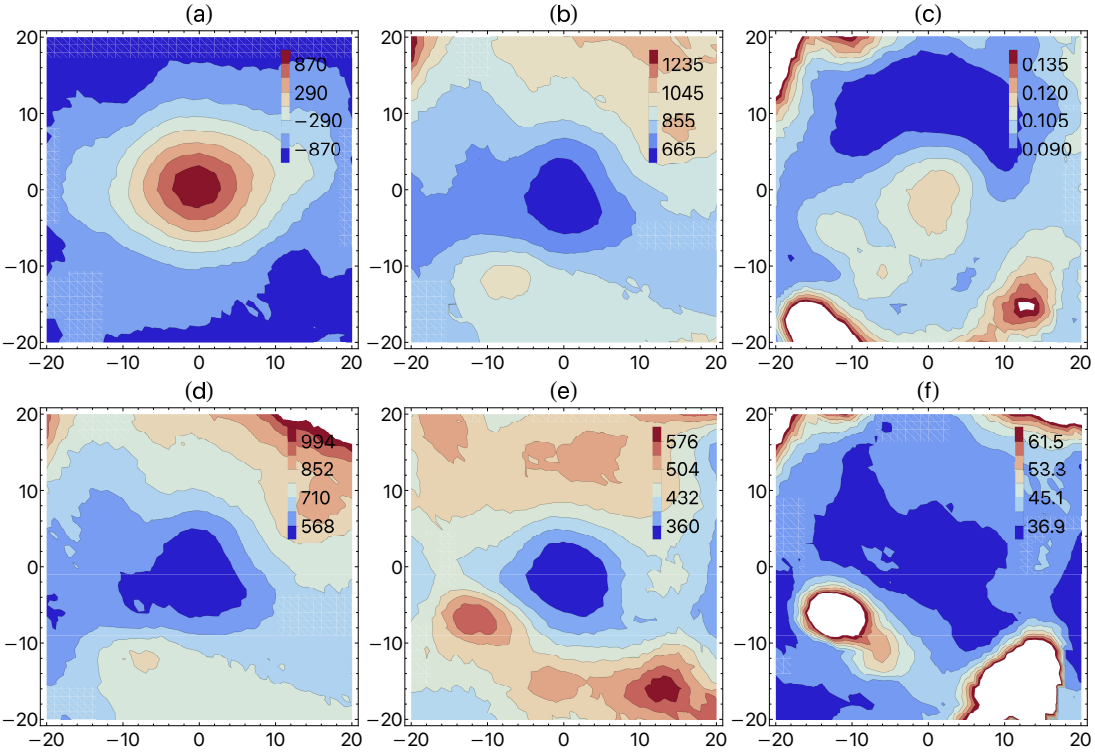

Figure 3.19: Average MT cell, this was calculated from 182 MT cells, (a), is the topography, (b) is the Approach Youngs modulus (E_{app}), (c), is τ, (d), is E_1, (e) is E_2 and (f) is η.

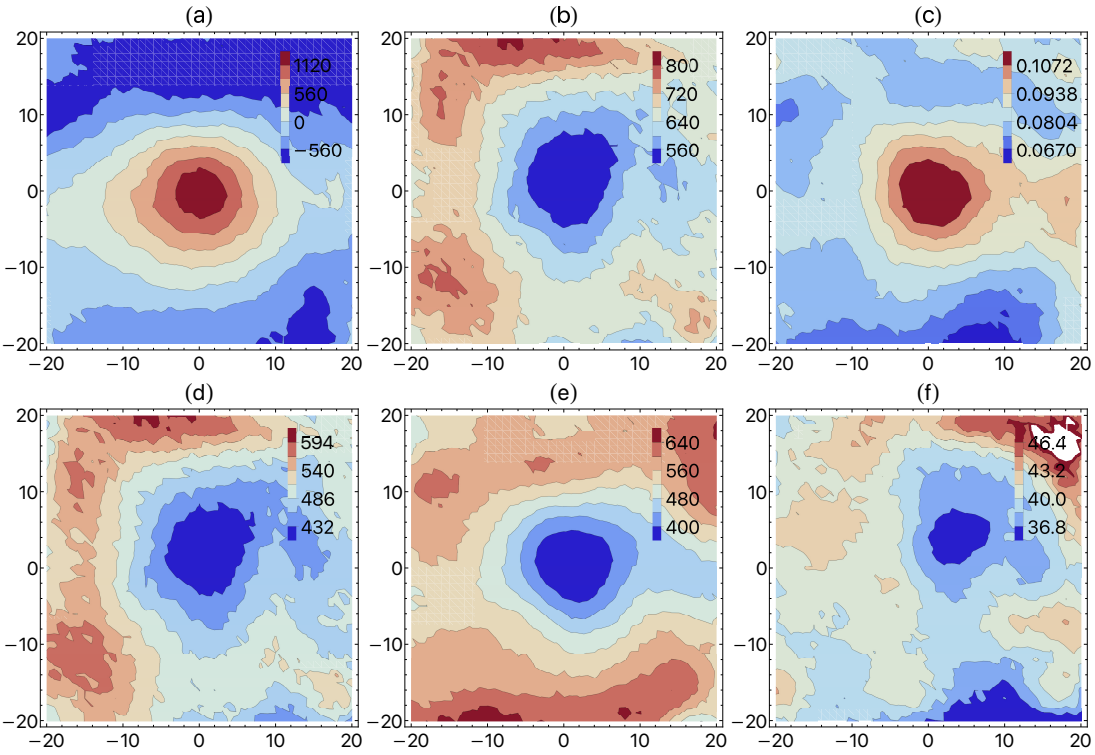

Figure 3.20: Average WFA cell, this was calculated from 62 WT cells cultured in WFA, (a), is the topography, (b) is the Approach Youngs modulus (E_{app}), (c), is τ, (d), is E_1, (e) is E_2 and (f) is η.

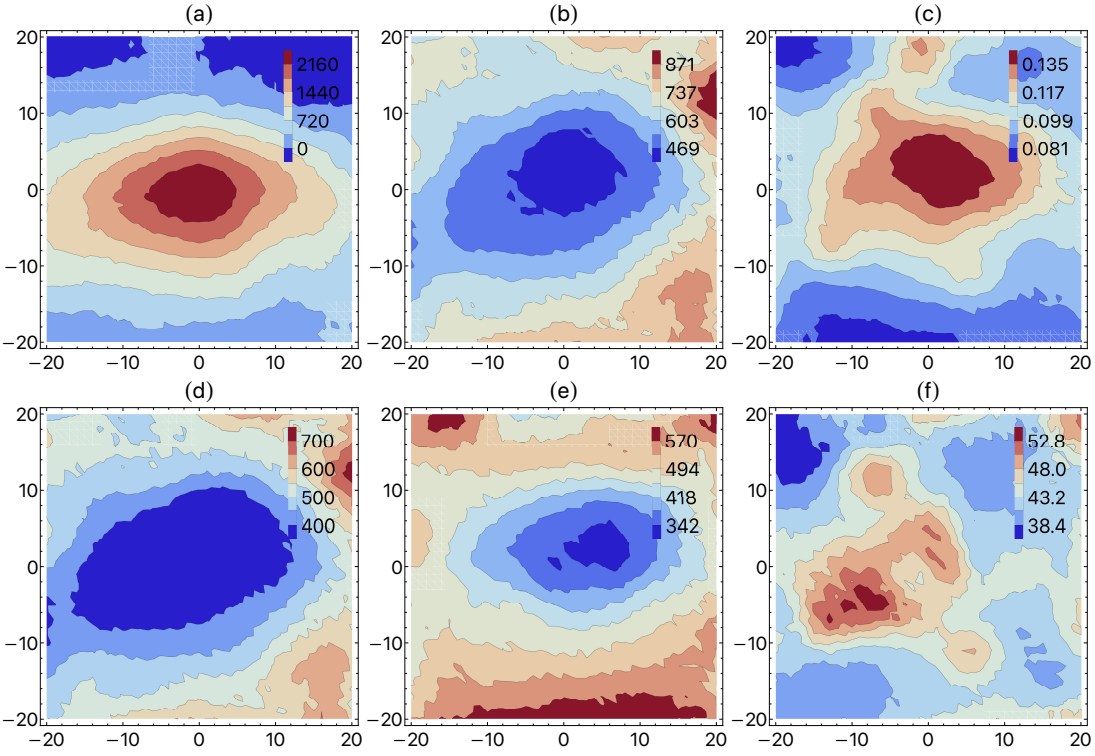

Figure 3.21: Average DMSO cell, this was calculated from 69 WT cells cultured in DMSO, (a), is the topography, (b) is the Approach Youngs modulus (E_{app}), (c), is τ, (d), is E_1, (e) is E_2 and (f) is η.

From the average topography, (a) in Fig.3.18, Fig.3.19, Fig.3.20 and Fig.3.21, we can can see that the control cells have a more pronounced ellipse shape when compared to the cells with cytoskeleton alteration. The cells with cytoskeletal alteration show no clear signature of the IF accumulation in any of the parameters. For all the cells, E_{app}, E_1 and E_2 has lower values near the nucleus area, while τ has higher values in the same zone.

3.5.2 Cell axis

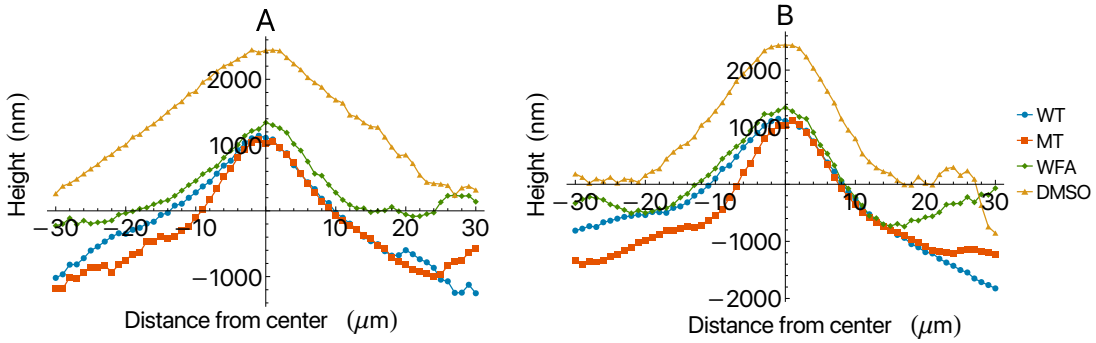

Figure 3.22: Average topography for all cell types, (a), along the semi major axis, (b), along the semi minor axis. The average height (measured for the point at 0 point to the point at -20 μm, this was done because for WT cells the right side of the cell seems to continue pass the "floor" defined by the left side) for the semi major axis is 1460 nm for WT, 1778 nm for MT, 1377 nm for WFA and 1437 for DMSO. For the semi minor axis we obtained 1650 nm for WT, 2013 nm for MT, 1842 nm for WFA and 2283 for DMSO. The blue dots are WT cells, the red squares are MT cells, the green diamonds are the WT cells cultured in WFA as explained previously and the yellow triangles are the WT cells cultured in DMSO as explained previously.

From Fig.3.22 we can conclude that there is a difference in cell height depending on the cell type. For the semi major axis, the average MT is the tallest, followed by the average WT, then the average WT cultured in DMSO and the average WT cell cultured in WFA is the shortest. For the semi minor axis, the average WT cells cultured in DMSO is the tallest, followed by the average MT, then the average WT cell cultured in WFA and the average WT is the shortest.

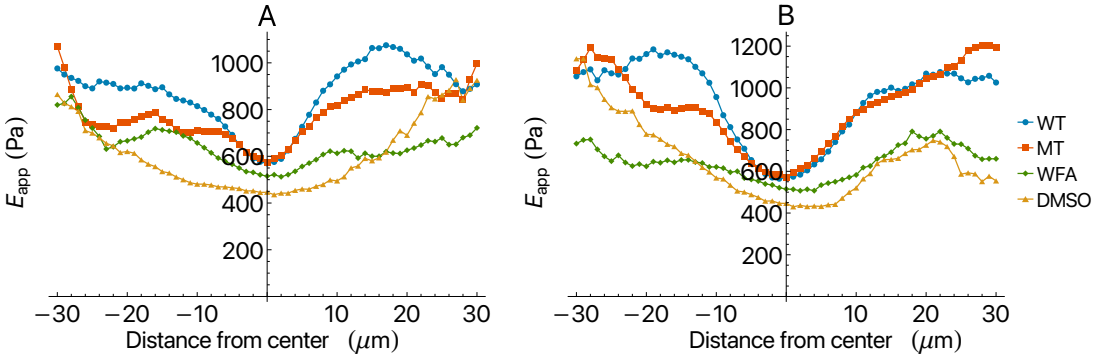

Figure 3.23: Average Young's modulus for all cells types, (a), along the semi major axis, (b), along the semi minor axis. The blue dots are WT cells, the red squares are MT cells, the green diamonds are the WT cells cultured in WFA as explained previously and the yellow triangles are the WT cells cultured in DMSO as explained previously. The blue dots are WT cells, the red squares are MT cells, the green diamonds are the WT cells cultured in WFA as explained previously and the yellow triangles are the WT cells cultured in DMSO as explained previously.

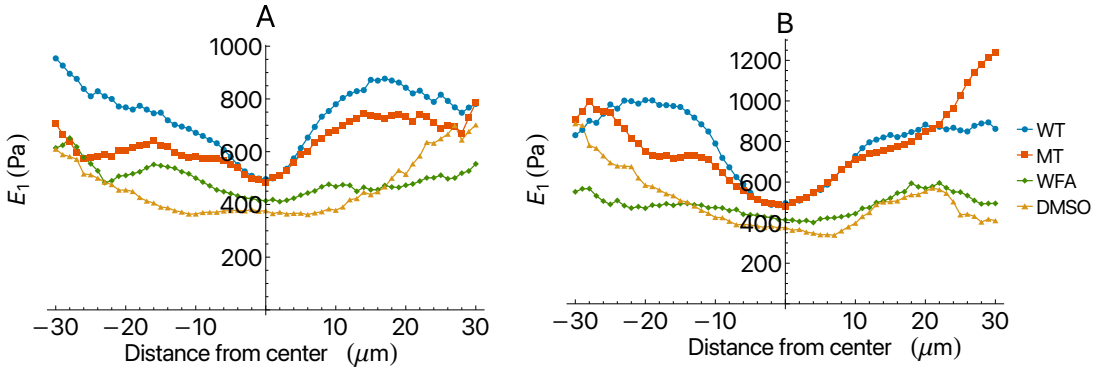

Figure 3.24: Average E_1 for all cells types, (a), along the semi major axis, (b), along the semi minor axis. The blue dots are WT cells, the red squares are MT cells, the green diamonds are the WT cells cultured in WFA as explained previously and the yellow triangles are the WT cells cultured in DMSO as explained previously. The blue dots are WT cells, the red squares are MT cells, the green diamonds are the WT cells cultured in WFA as explained previously and the yellow triangles are the WT cells cultured in DMSO as explained previously.

From Fig.3.23 and Fig.3.24 we can see that the zone near the center of the average cell, what is expected to be the nucleus zone (distance < 10 μm), has lower values of E_{app} and E_1, this is more noticeable for WT and MT cells. From both figures we can also see that for the nucleus zone the average WT cells cultured in DMSO as the lowest value E_{app} and E_1, followed by the average WT cells cultured in WFA, while WT and MT have similar values. In Fig.3.24 we can see that MT cells have smaller values of E_1 at around 10 μm which could be an indication of the IF accumulation at the perinuclear zone.

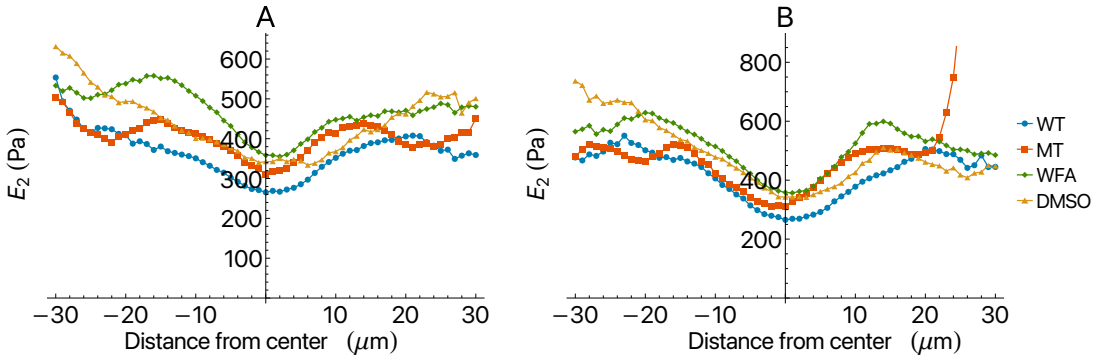

Figure 3.25: Average E_2 for all cells types, (a), along the semi major axis, (b), along the semi minor axis. The blue dots are WT cells, the red squares are MT cells, the green diamonds are the WT cells cultured in WFA as explained previously and the yellow triangles are the WT cells cultured in DMSO as explained previously. The blue dots are WT cells, the red squares are MT cells, the green diamonds are the WT cells cultured in WFA as explained previously and the yellow triangles are the WT cells cultured in DMSO as explained previously.

Similarly to Fig.3.23 and Fig.3.24 in Fig.3.25 we can see that the nucleus zone shows lower values of E_2. But contrary to Fig.3.23 and Fig.3.24 in Fig.3.25 the average WT cell has the lowest value of E_2, the average MT cell has the second lowest value of E_2 and the average WT cell cultured in WFA and DMSO show similarly high values of E_2.

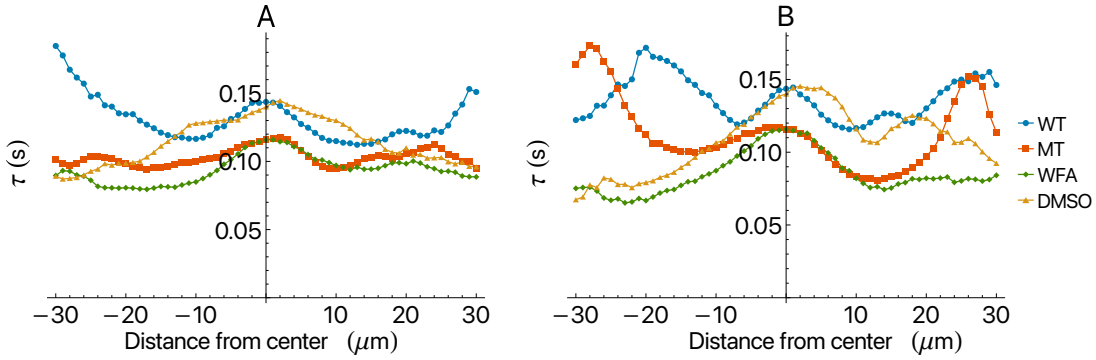

Figure 3.26: Average τ for all cells types, (a), along the semi major axis, (b), along the semi minor axis. The blue dots are WT cells, the red squares are MT cells, the green diamonds are the WT cells cultured in WFA as explained previously and the yellow triangles are the WT cells cultured in DMSO as explained previously. The blue dots are WT cells, the red squares are MT cells, the green diamonds are the WT cells cultured in WFA as explained previously and the yellow triangles are the WT cells cultured in DMSO as explained previously.

From Fig.3.26 we can see that in the nucleus zone τ is the highest. We can also see that for the nucleus zone the average WT and the average WT cultured in DMSO tend to have similar values of τ, and that for the nucleus zone the average MT and average WT cultured in WFA have similar values of τ.

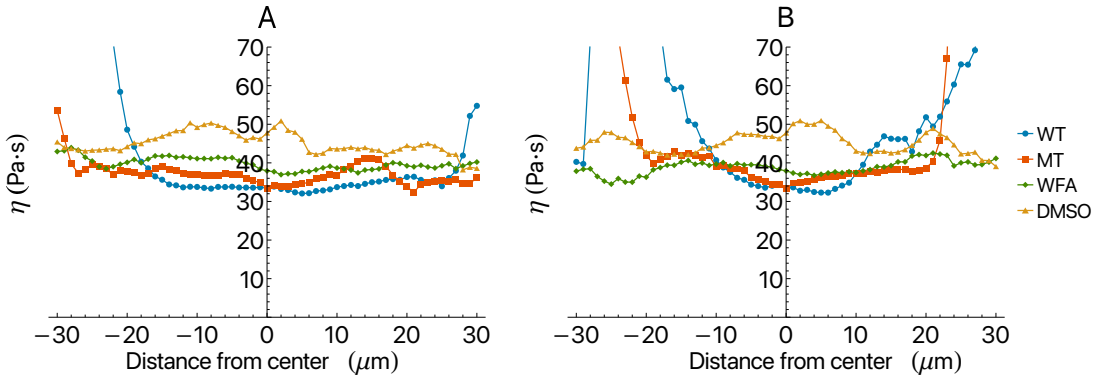

Figure 3.27: Average η for all cells types, (a), along the semi major axis, (b), along the semi minor axis. The blue dots are WT cells, the red squares are MT cells, the green diamonds are the WT cells cultured in WFA as explained previously and the yellow triangles are the WT cells cultured in DMSO as explained previously. The blue dots are WT cells, the red squares are MT cells, the green diamonds are the WT cells cultured in WFA as explained previously and the yellow triangles are the WT cells cultured in DMSO as explained previously.

From Fig.3.27 the values of η for the semi major axis seem to be constant for all cell types, with the average WT cell having the lowest value of η.

3.5.3 Nucleus and perinuclear area

To investigate potential differences between the nucleus and the perinuclear area, other than just analysing the profiles along a specific direction, the two regions were analysed separately. In Fig.3.28 we show the distribution of E_1, E_2 and η obtained within a range of 10 μm from the cell center and the distribution obtained within a ring of 10 to 20 μm from the cell center.

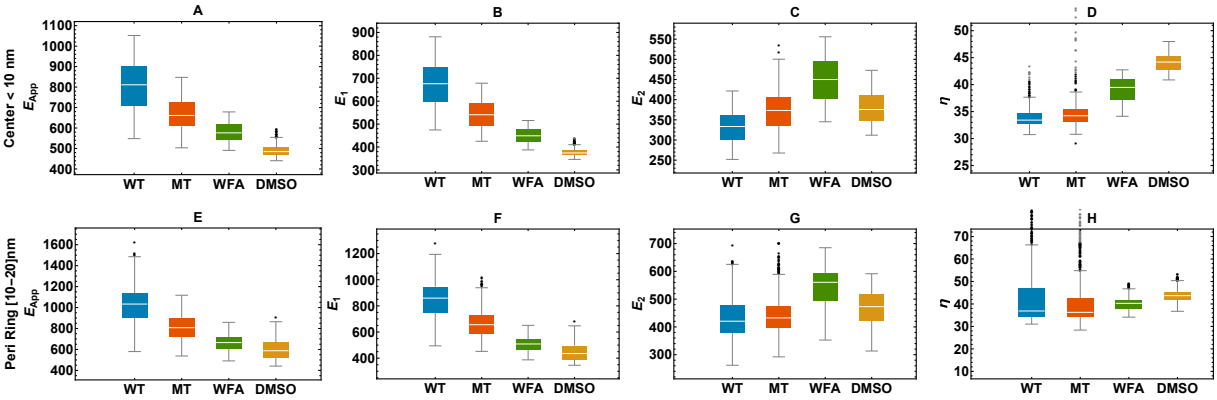

Figure 3.28: (A), (B), (C), (D), are respectively E_{app}, E_1, E_2 and η obtained within a range of 10 μm. (E), (F), (G), (H), are respectively E_{app}, E_1, E_2 and η obtained within a ring of 10 to 20 μm from the cell center. The black dots represent outliers with some not being shown for better visualisation.

3.6 Normalised values

To determine whether a relationship exists between the parameters obtained from the viscoelastic model and the Young's modulus obtained using the Hertz model and because of the great deal of variability in the cells mechanical parameters, to minimize biases and fluctuations arising from variations in cantilever stiffness and calibration of the cantilevers and AFM, we divided the obtained SLS' parameters (E_1, E_2 and η) for a cell by approach Young's modulus, E_{app}, for the same cell obtaining the normalised values, E_1/E_{app}, E_2/E_{app} and η/E_{app}. This is done because all the parameters depend on the cantilever stiffness and AFM calibration in the same manner, hence, the influence of the calibration should be mitigated.

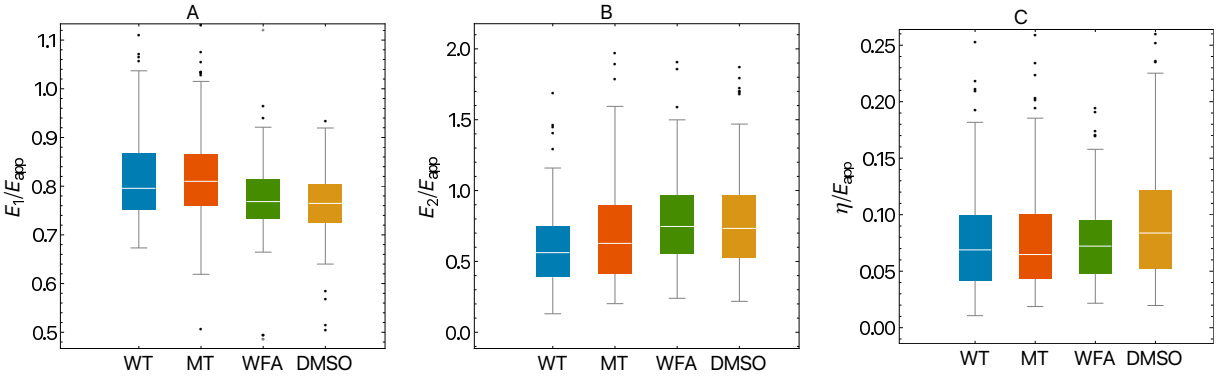

Figure 3.29: (A), E_1 obtained from the SLS model divided E_{app} obtained from the Hertz model. For WT we obtained 0.80 $(0.75, 0.87)$, for MT we obtain 0.81 $(0.76, 0.87)$, for WT cells cultured in WFA we obtained 0.77 $(0.73, 0.81)$ and for WT cell cultured in DMSO we obtain 0.76 $(0.73, 0.80)$. (B), E_2 obtained from the SLS model divided E_{app} obtained from the Hertz model. For WT we obtained 0.56 $(0.39, 0.77)$, for MT we obtain 0.63 $(0.41, 0.90)$, for WT cells cultured in WFA we obtained 0.75 $(0.55, 0.97)$ and for WT cell cultured in DMSO we obtain 0.73 $(0.53, 0.97)$. (C), η obtained from the SLS model divided E_{app} obtained from the Hertz model. For WT we obtained 69 $(42, 99)$ ms, for MT we obtain 65 $(43, 100)$ ms, for WT cells cultured in WFA we obtained 72 $(48, 95)$ ms and for WT cells cultured in DMSO we obtain 84 $(52, 122)$ ms The black dots represent outliers with some not being shown for better visualisation.

Table 3.4: Values obtained for the normalisation of the SLS parameters (E_1, E_2 and η) by E_{app} for WT, MT, WT cells cultured in WFA and WT cells cultured in DMSO. Values are expressed as $Median\ (Q_1, Q_3)$.

	E_1/E_{app}	E_2/E_{app}	η/E_{app} (ms)
WT	0.80 (0.75, 0.87)	0.56 (0.39, 0.77)	69 (42, 99)
MT	0.81 (0.76, 0.87)	0.63 (0.41, 0.90)	65 (43, 100)
WFA	0.77 (0.73, 0.81)	0.75 (0.55, 0.97)	72 (48, 95)
DMSO	0.76 (0.73, 0.80)	0.73 (0.53, 0.97)	84 (52, 122)

As we can see from Fig.3.29 (A) and Table 3.4 the distributions for the untreated cells, *i.e.* cells without drugs (WT and MT), are similar, the same happens for the distribution of the treated cells *i.e.* cells withh drugs (WT cells cultured in DMSO and WT cells cultured in WFA), with the distributions for the treated cells having lower medians; (B) the distribution of the untreated cells is not as similar as it was in (A), but the distribution of the treated cells is still similar, with the distributions for the treated cells having higher medians; (C) the distribution of untreated cells are similar, WT cells cultured in WFA also have a similar distribution to untreated cells but the distribution is narrower, WT cell cultured in DMSO have larger median and a wider distribution than any of the other cell types.

Similarly to what was done before, we show the normalised distribution of E_1, E_2 and η obtained within a range of 10 μm from the cell center and the normalised distribution obtained within a ring of 10 to 20 μm from the cell center. The normalisation is done by dividing by the median of E_{app} for the region of interest.

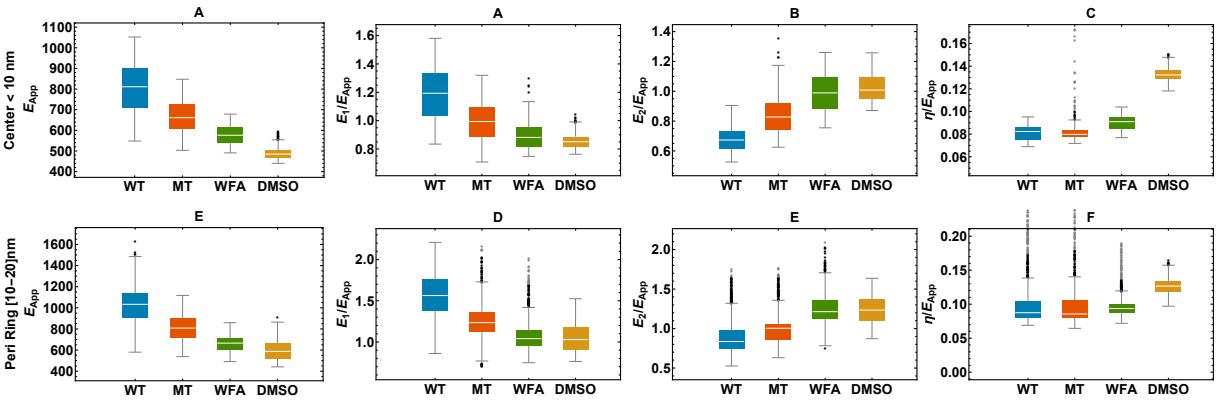

Figure 3.30: (A), (B), (C), (D), are respectively E_{app}, E_1/E_{app}, E_2/E_{app} and η/E_{app} obtained within a range of 10 μm. (E), (F), (G), (H), are respectively, E_{app}, E_1/E_{app}, E_2/E_{app} and η/E_{app} obtained within a ring of 10 to 20 μm from the cell center. The black dots represent outliers with some not being shown for better visualisation.

Chapter 4

Conclusion

We have been able to find a strategy to apply the SLS (standard linear solid) model to cells under the approximation that the indentation is linear in time. The SLS model, used to assess viscoelastic behaviour, successfully captured the mechanical properties of the cells. With this approximation we can analytically solve the set of equations imposed by the SLS model. The study demonstrated that this model could differentiate between elasticity ($E1$ and $E2$), relaxation time (τ) and viscosity (η), providing a deeper insight into the viscoelastic nature of the cells under different conditions. The differences between distinct cell types obtained from the SLS model, are much more noticeable than those obtained using the Hertz model alone.

4.1 Per Cell analysis

The data obtained from taking the median values for each cell, considering the elipse that defines the cell, is presented in Table 4.1.

Table 4.1: Values obtained for the mechanical properties for the Per Cell analysis for WT, MT, WT cells cultured in WFA and WT cells cultured in DMSO. Values are expressed as $Median\ (Q_1, Q_3)$.

Hertz / Cell type	E_{app} (Pa)	E_{ret} (Pa)
WT	533 (308, 900)	556 (320, 911)
MT	541 (306, 1020)	568 (309, 1020)
WFA	535 (413, 816)	560 (425, 823)
DMSO	383 (285, 593)	386 (303, 624)

SLS / Cell type	E_1 (Pa)	E_2 (Pa)	τ (s)	η (Pa·s)
WT	430 (243, 734)	284 (164, 511)	0.11 (0.09, 0.16)	36 (25, 50)
MT	429 (247, 846)	338 (289, 561)	0.09 (0.08, 0.13)	36 (24, 52)
WFA	404 (311, 654)	444 (357, 532)	0.09 (0.07, 0.11)	41 (36, 47)
DMSO	309 (236, 457)	347 (257, 435)	0.11 (0.10, 0.14)	38 (32, 46)

The differences in the mechanical properties are not as pronounced as one might have imagined.

Considering the data shown in Table 4.1 one can conclude that the distribution of viscosity (η) is similar in pairs, WT and MT have similar distributions. WT cultured in WFA and WT cultured in DMSO also have similar distributions, which points to η being less affected by the

cytoskeletal alterations and more by the pharmacological treatments.

For E_{app} , E_{ret} and E_1, WT, MT and WT cultured in WFA have similar values, WT cultured in DMSO show values significantly lower when compared to the other cell types. DMSO-treated cells displayed some mechanical properties that were different from WT cells, which implies that some differences observed between MT and WT cells cultured in WFA can be in part due to the effect of DMSO.

4.2 Normalised individual cell analysis

Proceeding in the same manner as before but normalising the quantities by the median E_{app} for that cell, we obtained the data displayed in Table 4.2. Since the parameters all depend on the cantilever stiffness and AFM calibration in the same manner, these influences should be mitigated. Hence, the SLS parameters are measured in units of effective elasticity.

Table 4.2: Values obtained for the normalisation of the SLS parameters (E_1, E_2 and η) by E_{app} for WT, MT, WT cells cultured in WFA and WT cells cultured in DMSO. Values are expressed as $Median\ (Q_1, Q_3)$.

	E_1/E_{app}	E_2/E_{app}	η/E_{app} (ms)
WT	0.80 (0.75, 0.87)	0.56 (0.39, 0.77)	69 (42, 99)
MT	0.81 (0.76, 0.87)	0.63 (0.41, 0.90)	65 (43, 100)
WFA	0.77 (0.73, 0.81)	0.75 (0.55, 0.97)	72 (48, 95)
DMSO	0.76 (0.73, 0.80)	0.73 (0.53, 0.97)	84 (52, 122)

From this strategy a distinction between untreated (WT and MT) cells and treated cells (WT cultured in WFA or DMSO) seems to emerge: the normalised median of E_1, E_1/E_{app}, is higher for untreated cells, whereas E_2/E_{app} is higher for the treated cells. For η/E_{app} the median values were similar for WT, MT and WT cells cultured in WFA, with WT cells cultured in DMSO having a larger median value.

4.3 "Average" cell

The average cell was computed by stacking and aligning all cells and then computing an average model-like cell.

Since for MT cells and WT cells cultured in WFA fluorescent microscopy show marked differences in the perinuclear area, E_{app} E_1, E_2 and η are obtained within a range of 10 μm from the cell center and within a ring of 10 to 20 μm from the cell center. The corresponding values are shown in Table 4.3.

Table 4.3: Values obtained for E_{app} from the Hertz model and for E_1, E_2 and η from the SLS model for both the nucleus area (radius< 10 μm) and the perinuclear area (10 <radius< 20 μm). Values are expressed as $Median \pm std$.

radius < 10 μm	E_{app} (Pa)	E_1 (Pa)	E_2 (Pa)	η (Pa·s)
WT	811 ± 123	676 ± 96	333 ± 41	33.4 ± 2.1
MT	661 ± 78	541 ± 59	373 ± 48	34.2 ± 5.2
WFA	576 ± 47	449 ± 32	450 ± 55	39.5 ± 2.3
DMSO	485 ± 31	374 ± 18	377 ± 41	44.2 ± 1.6
10 < radius < 20 μm	E_{app} (Pa)	E_1 (Pa)	E_2 (Pa)	η (Pa·s)
WT	1033 ± 168	859 ± 139	421 ± 76	36.9 ± 28.6
MT	808 ± 119	656 ± 100	432 ± 68	36.3 ± 36.5
WFA	666 ± 74	509 ± 55	561 ± 69	40.3 ± 2.5
DMSO	588 ± 93	435 ± 67	473 ± 63	43.7 ± 2.8

4.4 "Average" cell normalised

Attempting the same as before but analysing the normalised values, we have obtained E_1/E_{app}, E_2/E_{app} and η/E_{app}, within a range of 10 μm from the cell center and within a ring of 10 to 20 μm from the cell center, which are presented in Table 4.4. The normalisation is done by dividing by the median of E_{app} for the region of interest.

Table 4.4: Values obtained for E_{app} from the Hertz model and normalised values E_1/E_{app}, E_2/E_{app} and η/E_{app} obtained from the SLS model for both the nucleus area (radius< 10 μm) and the perinuclear area (10 <radius< 20 μm). Values are expressed as $Median \pm std$.

radius < 10 μm	E_{app} (Pa)	E_1/E_{app}	E_2/E_{app}	η/E_{app} (ms)
WT	811 ± 123	1.19 ± 0.18	0.67 ± 0.08	82 ± 6
MT	661 ± 78	0.99 ± 0.14	0.83 ± 0.12	80 ± 15
WFA	576 ± 47	0.88 ± 0.09	0.99 ± 0.12	91 ± 6
DMSO	485 ± 31	0.85 ± 0.06	1.00 ± 0.09	132 ± 6
10 < radius < 20 μm	E_{app} (Pa)	E_1/E_{app}	E_2/E_{app}	η/E_{app} (ms)
WT	1033 ± 168	1.56 ± 0.28	0.84 ± 0.21	87 ± 44
MT	808 ± 119	1.23 ± 0.21	1.00 ± 0.19	86 ± 144
WFA	666 ± 74	1.04 ± 0.19	1.21 ± 0.20	94 ± 17
DMSO	588 ± 93	1.03 ± 0.17	1.23 ± 0.18	127 ± 11

We emphasise these following final remarks to what can drawn from the data computed after the *average cell*. We justify this by the fact that the differences obtained between the different cell types are more distinct in this case. Notice that the trend is somewhat compatible with the data presented before. The values at the nucleus and perinuclear areas are different but the trend is the same when comparing different cell types.

If we look at the data previous to normalisation, E_1 follows the same tendency as E_{app} and E_2 follows a different trend.

In both cases (normalised and not normalised) the values for E_1 for WT cells cultured in WFA and WT cells cultured in DMSO are clearly lower than the values for cells not chemically treated. Additionally in both cases, the MT cells overall show lower values for E_1 which is compatible with cytoskeleton impairment. This aligns with observations that ARSACS, a disease that

disrupts cytoskeletal function, leads to mechanical changes in cells.

Similarly to what was observed in section 4.3, the normalised E_2/E_{app} is particularly larger for cells which are pharmacologically treated, whereas E_1/E_{app} is lower for those cells. Overall the differences between treated cells and WT cells are higher than the differences between WT and MT cells.

We conclude that DMSO does have an effect on the mechanical properties of cells. This can be seen in E_1, E_2 and in the topography. WT cells treated in DMSO are more elongated than other cell types.

The methodologies used in this work provide a basis for further exploration of the mechanical properties as potential diagnostic markers or therapeutic targets for cytoskeleton-related diseases.

Bibliography

[1] G. M. Cooper and K. Adams, *The cell: a molecular approach.* Oxford University Press, 2019.

[2] (2023, May) Histology, cell. [Online]. Available: https://www.ncbi.nlm.nih.gov/books/NBK554382/

[3] I. A. Hatton, E. D. Galbraith, N. S. Merleau, T. P. Miettinen, B. M. Smith, and J. A. Shander, "The human cell count and size distribution," *Proceedings of the National Academy of Sciences*, vol. 120, no. 39, p. e2303077120, 2023.

[4] A. F. Pegoraro, P. Janmey, and D. A. Weitz, "Mechanical properties of the cytoskeleton and cells," *Cold Spring Harbor perspectives in biology*, vol. 9, no. 11, p. a022038, 2017.

[5] B. Fabry, G. N. Maksym, J. P. Butler, M. Glogauer, D. Navajas, and J. J. Fredberg, "Scaling the microrheology of living cells," *Physical review letters*, vol. 87, no. 14, p. 148102, 2001.

[6] D. T. Chen, Q. Wen, P. A. Janmey, J. C. Crocker, and A. G. Yodh, "Rheology of soft materials," *Annu. Rev. Condens. Matter Phys.*, vol. 1, no. 1, pp. 301–322, 2010.

[7] F. Huber, A. Boire, M. P. López, and G. H. Koenderink, "Cytoskeletal crosstalk: when three different personalities team up," *Current opinion in cell biology*, vol. 32, pp. 39–47, 2015.

[8] D. Mizuno, C. Tardin, C. F. Schmidt, and F. C. MacKintosh, "Nonequilibrium mechanics of active cytoskeletal networks," *Science*, vol. 315, no. 5810, pp. 370–373, 2007.

[9] M. Guo, A. J. Ehrlicher, M. H. Jensen, M. Renz, J. R. Moore, R. D. Goldman, J. Lippincott-Schwartz, F. C. Mackintosh, and D. A. Weitz, "Probing the stochastic, motor-driven properties of the cytoplasm using force spectrum microscopy," *Cell*, vol. 158, no. 4, pp. 822–832, 2014.

[10] "X-ray studies of the structure of hair, wool, and related fibres.- i. general," *Philosophical Transactions of the Royal Society of London. Series A, Containing Papers of a Mathematical or Physical Character*, vol. 230, no. 681-693, pp. 75–101, Sep. 1931. [Online]. Available: https://doi.org/10.1098/rsta.1932.0003

[11] F. H. C. CRICK, "Is α-keratin a coiled coil?" *Nature*, vol. 170, no. 4334, pp. 882–883, Nov. 1952. [Online]. Available: https://doi.org/10.1038/170882b0

[12] F. H. C. Crick, "The packing of α-helices: simple coiled-coils," *Acta Crystallographica*, vol. 6, no. 8, pp. 689–697, Sep. 1953. [Online]. Available: https://doi.org/10.1107/s0365110x53001964

[13] P. M. Steinert, W. W. Idler, and S. B. Zimmerman, "Self-assembly of bovine epidermal keratin filaments in vitro," *Journal of Molecular Biology*, vol. 108, no. 3, pp. 547–567, Dec. 1976. [Online]. Available: https://doi.org/10.1016/s0022-2836(76)80136-2

[14] H. Ishikawa, R. Bischoff, and H. Holtzer, "MITOSIS AND INTERMEDIATE-SIZED FILAMENTS IN DEVELOPING SKELETAL MUSCLE," *Journal of Cell Biology*, vol. 38, no. 3, pp. 538–555, Sep. 1968. [Online]. Available: https://doi.org/10.1083/jcb.38.3.538

[15] C. Mencarelli, S. Ciolfi, D. Caroti, P. Lupetti, and R. Dallai, "Isomin: a novel cytoplasmic intermediate filament protein from an arthropod species," *BMC Biology*, vol. 9, no. 1, Feb. 2011. [Online]. Available: https://doi.org/10.1186/1741-7007-9-17

[16] R. G. Oshima, "Intermediate filaments: A historical perspective," *Experimental Cell Research*, vol. 313, no. 10, pp. 1981–1994, Jun. 2007. [Online]. Available: https://doi.org/10.1016/j.yexcr.2007.04.007

[17] M. B. Omary *et al.*, ""if-pathies": a broad spectrum of intermediate filament–associated diseases," *The Journal of clinical investigation*, vol. 119, no. 7, pp. 1756–1762, 2009.

[18] M. Tardy, C. Fages, G. Le Prince, B. Rolland, and J. Nunez, "Regulation of the glial fibrillary acidic protein (gfap) and of its encoding mrna in the developing brain and in cultured astrocytes," *Molecular aspects of development and aging of the nervous system*, pp. 41–52, 1990.

[19] R. A. Quinlan, M. Brenner, J. E. Goldman, and A. Messing, "Gfap and its role in alexander disease," *Experimental cell research*, vol. 313, no. 10, pp. 2077–2087, 2007.

[20] T. Katsumoto, A. Mitsushima, and T. Kurimura, "The role of the vimentin intermediate filaments in rat 3y1 cells elucidated by immunoelectron microscopy and computer-graphic reconstruction," *Biology of the Cell*, vol. 68, no. 1-3, pp. 139–146, 1990.

[21] M. Ogrodnik, H. Salmonowicz, R. Brown, J. Turkowska, W. Średniawa, S. Pattabiraman, T. Amen, A.-c. Abraham, N. Eichler, R. Lyakhovetsky *et al.*, "Dynamic junq inclusion bodies are asymmetrically inherited in mammalian cell lines through the asymmetric partitioning of vimentin," *Proceedings of the National Academy of Sciences*, vol. 111, no. 22, pp. 8049–8054, 2014.

[22] K. Michalczyk and M. Ziman, "Nestin structure and predicted function in cellular cytoskeletal organisation," *Histology and histopathology*, 2005.

[23] M. Li, L. Peng, Z. Wang, L. Liu, M. Cao, J. Cui, F. Wu, and J. Yang, "Roles of the cytoskeleton in human diseases," *Molecular Biology Reports*, pp. 1–10, 2023.

[24] F. Parker, T. G. Baboolal, and M. Peckham, "Actin mutations and their role in disease," *International Journal of Molecular Sciences*, vol. 21, no. 9, p. 3371, 2020.

[25] R. Romaniello, C. Zucca, F. Arrigoni, P. Bonanni, E. Panzeri, M. T. Bassi, and R. Borgatti, "Epilepsy in tubulinopathy: personal series and literature review," *Cells*, vol. 8, no. 7, p. 669, 2019.

[26] M. R. Heaven, L. Wilson, S. Barnes, and M. Brenner, "Relative stabilities of wild-type and mutant glial fibrillary acidic protein in patients with alexander disease," *Journal of Biological Chemistry*, vol. 294, no. 43, pp. 15 604–15 612, 2019.

[27] M. Westin, E. Rekabdar, L. Blomstrand, P. Klintberg, M. Jontell, and J. Robledo-Sierra, "Mutations in the genes for keratin-4 and keratin-13 in swedish patients with white sponge nevus," *Journal of Oral Pathology & Medicine*, vol. 47, no. 2, pp. 152–157, 2018.

[28] V. Cenni, C. Capanni, E. Mattioli, E. Schena, S. Squarzoni, M. G. Bacalini, P. Garagnani, S. Salvioli, C. Franceschi, and G. Lattanzi, "Lamin a involvement in ageing processes," *Ageing Research Reviews*, vol. 62, p. 101073, 2020.

[29] H. Dridi, W. Wu, S. R. Reiken, R. M. Ofer, Y. Liu, Q. Yuan, L. Sittenfeld, J. Kushner, A. Muchir, H. J. Worman *et al.*, "Ryanodine receptor remodeling in cardiomyopathy and muscular dystrophy caused by lamin a/c gene mutation," *Human Molecular Genetics*, vol. 29, no. 24, pp. 3919–3934, 2020.

[30] (2020, Jan) Genereviews - arsacs. [Online]. Available: https://www.ncbi.nlm.nih.gov/books/NBK1255/

[31] J. Bouchard, A. Barbeau, R. Bouchard, and R. Bouchard, "Autosomal recessive spastic ataxia of charlevoix-saguenay," *Canadian Journal of neurological sciences*, vol. 5, no. 1, pp. 61–69, 1978.

[32] L. LOVD development team. The sacs gene homepage. [Online]. Available: https://databases.lovd.nl/shared/genes/SACS

[33] A. P. Vogel, N. Rommel, A. Oettinger, L. H. Stoll, E.-M. Kraus, C. Gagnon, M. Horger, P. Krumm, D. Timmann, E. Storey *et al.*, "Coordination and timing deficits in speech and swallowing in autosomal recessive spastic ataxia of charlevoix–saguenay (arsacs)," *Journal of neurology*, vol. 265, pp. 2060–2070, 2018.

[34] R. A. Kuchay, Y. R. Mir, X. Zeng, A. Hassan, J. Musarrat, I. Parwez, C. Kernstock, A. Traschütz, and M. Synofzik, "Arsacs as a worldwide disease: novel sacs mutations identified in a consanguineous family from the remote tribal jammu and kashmir region in india," *The Cerebellum*, vol. 18, pp. 807–812, 2019.

[35] E. Garcia-Martin, L. E. Pablo, J. Gazulla, A. Vela, J. M. Larrosa, V. Polo, M. L. Marques, and J. Alfaro, "Retinal segmentation as noninvasive technique to demonstrate hyperplasia in ataxia of charlevoix-saguenay," *Investigative ophthalmology & visual science*, vol. 54, no. 10, pp. 7137–7142, 2013.

[36] Z. Ali, J. Klar, M. Jameel, K. Khan, A. Fatima, R. Raininko, S. Baig, and N. Dahl, "Novel sacs mutations associated with intellectual disability, epilepsy and widespread supratentorial abnormalities," *Journal of the Neurological Sciences*, vol. 371, pp. 105–111, 2016.

[37] H. Shimazaki, Y. Takiyama, K. Sakoe, Y. Ando, and I. Nakano, "A phenotype without spasticity in sacsin-related ataxia," *Neurology*, vol. 64, no. 12, pp. 2129–2131, 2005.

[38] H. Shimazaki, K. Sakoe, K. Niijima, I. Nakano, and Y. Takiyama, "An unusual case of a spasticity-lacking phenotype with a novel sacs mutation," *Journal of the neurological sciences*, vol. 255, no. 1-2, pp. 87–89, 2007.

[39] J. Baets, T. Deconinck, K. Smets, D. Goossens, P. Van den Bergh, K. Dahan, E. Schmedding, P. Santens, V. M. Rasic, P. Van Damme *et al.*, "Mutations in sacs cause atypical and late-onset forms of arsacs," *Neurology*, vol. 75, no. 13, pp. 1181–1188, 2010.

[40] M. Synofzik, A. S. Soehn, J. Gburek-Augustat, J. Schicks, K. N. Karle, R. Schüle, T. B. Haack, M. Schöning, S. Biskup, S. Rudnik-Schöneborn *et al.*, "Autosomal recessive spastic ataxia of charlevoix saguenay (arsacs): expanding the genetic, clinical and imaging spectrum," *Orphanet journal of rare diseases*, vol. 8, no. 1, p. 41, 2013.

[41] K. Vill, W. Müller-Felber, D. Gläser, M. Kuhn, V. Teusch, H. Schreiber, J. Weis, J. Klepper, A. Schirmacher, A. Blaschek *et al.*, "Sacs variants are a relevant cause of autosomal recessive hereditary motor and sensory neuropathy," *Human genetics*, vol. 137, pp. 911–919, 2018.

[42] F. M. Rezende Filho, M. H. Parkinson, J. L. Pedroso, R. Poh, I. Faber, C. M. Lourenço, W. M. Júnior, M. C. F. Junior, F. Kok, J. M. F. Sallum *et al.*, "Clinical, ophthalmological, imaging and genetic features in brazilian patients with arsacs," *Parkinsonism & related disorders*, vol. 62, pp. 148–155, 2019.

[43] R. Lariviere, R. Gaudet, B. J. Gentil, M. Girard, T. C. Conte, S. Minotti, K. Leclerc-Desaulniers, K. Gehring, R. A. McKinney, E. A. Shoubridge *et al.*, "Sacs knockout mice present pathophysiological defects underlying autosomal recessive spastic ataxia of charlevoix-saguenay," *Human molecular genetics*, vol. 24, no. 3, pp. 727–739, 2015.

[44] F. Murtinheira, M. Migueis, R. Letra-Vilela, M. Diallo, A. Quezada, C. A. Valente, A. Oliva, C. Rodriguez, V. Martin, and F. Herrera, "Sacsin deletion induces aggregation of glial intermediate filaments," *Cells*, vol. 11, no. 2, p. 299, 2022.

[45] J. C. Engert, P. Bérubé, J. Mercier, C. Doré, P. Lepage, B. Ge, J.-P. Bouchard, J. Mathieu, S. B. Melançon, M. Schalling *et al.*, "Arsacs, a spastic ataxia common in northeastern quebec, is caused by mutations in a new gene encoding an 11.5-kb orf," *Nature genetics*, vol. 24, no. 2, pp. 120–125, 2000.

[46] D. A. Parfitt, G. J. Michael, E. G. Vermeulen, N. V. Prodromou, T. R. Webb, J.-M. Gallo, M. E. Cheetham, W. S. Nicoll, G. L. Blatch, and J. P. Chapple, "The ataxia protein sacsin is a functional co-chaperone that protects against polyglutamine-expanded ataxin-1," *Human molecular genetics*, vol. 18, no. 9, pp. 1556–1565, 2009.

[47] M. Girard, R. Larivière, D. A. Parfitt, E. C. Deane, R. Gaudet, N. Nossova, F. Blondeau, G. Prenosil, E. G. Vermeulen, M. R. Duchen *et al.*, "Mitochondrial dysfunction and purkinje cell loss in autosomal recessive spastic ataxia of charlevoix-saguenay (arsacs)," *Proceedings of the National Academy of Sciences*, vol. 109, no. 5, pp. 1661–1666, 2012.

[48] B. J. Gentil, G.-T. Lai, M. Menade, R. Larivière, S. Minotti, K. Gehring, J.-P. Chapple, B. Brais, and H. D. Durham, "Sacsin, mutated in the ataxia arsacs, regulates intermediate filament assembly and dynamics," *The FASEB Journal*, vol. 33, no. 2, pp. 2982–2994, 2019.

[49] E. J. Duncan, R. Larivière, T. Y. Bradshaw, F. Longo, N. Sgarioto, M. J. Hayes, L. E. Romano, S. Nethisinghe, P. Giunti, M. B. Bruntraeger *et al.*, "Altered organization of the intermediate filament cytoskeleton and relocalization of proteostasis modulators in cells lacking the ataxia protein sacsin," *Human molecular genetics*, vol. 26, no. 16, pp. 3130–3143, 2017.

[50] K. Takahashi and S. Yamanaka, "Induction of pluripotent stem cells from mouse embryonic and adult fibroblast cultures by defined factors," *cell*, vol. 126, no. 4, pp. 663–676, 2006.

[51] F. Morani, S. Doccini, R. Sirica, M. Paterno, F. Pezzini, I. Ricca, A. Simonati, M. Delledonne, and F. M. Santorelli, "Functional transcriptome analysis in arsacs ko cell model reveals a role of sacsin in autophagy," *Scientific reports*, vol. 9, no. 1, p. 11878, 2019.

[52] A. Louit, M.-J. Beaudet, M. Blais, F. Gros-Louis, N. Dupré, and F. Berthod, "In vitro characterization of motor neurons and purkinje cells differentiated from induced pluripotent stem cells generated from patients with autosomal recessive spastic ataxia of charlevoix-saguenay," *Stem Cells International*, vol. 2023, no. 1, p. 1496597, 2023.

[53] P. Benda, J. Lightbody, G. Sato, L. Levine, and W. Sweet, "Differentiated rat glial cell strain in tissue culture," *Science*, vol. 161, no. 3839, pp. 370–371, 1968.

[54] M. L. Goodenberger and R. B. Jenkins, "Genetics of adult glioma," *Cancer genetics*, vol. 205, no. 12, pp. 613–621, 2012.

[55] P. Bargagna-Mohan, A. Hamza, Y.-e. Kim, Y. K. A. Ho, N. Mor-Vaknin, N. Wendschlag, J. Liu, R. M. Evans, D. M. Markovitz, C.-G. Zhan *et al.*, "The tumor inhibitor and antiangiogenic agent withaferin a targets the intermediate filament protein vimentin," *Chemistry & biology*, vol. 14, no. 6, pp. 623–634, 2007.

[56] J. T. Thaiparambil, L. Bender, T. Ganesh, E. Kline, P. Patel, Y. Liu, M. Tighiouart, P. M. Vertino, R. D. Harvey, A. Garcia *et al.*, "Withaferin a inhibits breast cancer invasion and metastasis at sub-cytotoxic doses by inducing vimentin disassembly and serine 56 phosphorylation," *International journal of cancer*, vol. 129, no. 11, pp. 2744–2755, 2011.

[57] L.-X. Chen, H. He, and F. Qiu, "Natural withanolides: an overview," *Natural product reports*, vol. 28, no. 4, pp. 705–740, 2011.

[58] T. Sultana, M. K. Okla, M. Ahmed, N. Akhtar, A. Al-Hashimi, H. Abdelgawad, and I.-u. Haq, "Withaferin a: from ancient remedy to potential drug candidate," *Molecules*, vol. 26, no. 24, p. 7696, 2021.

[59] A. Grover, A. Shandilya, V. Agrawal, P. Pratik, D. Bhasme, V. S. Bisaria, and D. Sundar, "Hsp90/cdc37 chaperone/co-chaperone complex, a novel junction anticancer target elucidated by the mode of action of herbal drug withaferin a," *BMC bioinformatics*, vol. 12, pp. 1–13, 2011.

[60] W. Suttana, S. Mankhetkorn, W. Poompimon, A. Palagani, S. Zhokhov, S. Gerlo, G. Haegeman, and W. V. Berghe, "Differential chemosensitization of p-glycoprotein over-expressing k562/adr cells by withaferin a and siamois polyphenols," *Molecular cancer*, vol. 9, pp. 1–22, 2010.

[61] P. U. Devi, "Withaferin a: a new radiosensitizer from the indian medicinal plant withania somnifera," *International Journal of Radiation Biology*, vol. 69, no. 2, pp. 193–197, 1996.

[62] M. K. Al-Hindawi, S. H. Al-Khafaji, and M. H. Abdul-Nabi, "Anti-granuloma activity of iraqi withania somnifera," *Journal of ethnopharmacology*, vol. 37, no. 2, pp. 113–116, 1992.

[63] B. Shohat, I. Kirson, and D. Lavie, "Immunosuppressive activity of two plant steroidal lactones withaferin a and withanolide e." *Biomedicine/[publiee Pour l'AAICIG]*, vol. 28, no. 1, pp. 18–24, 1978.

[64] V. Khedgikar, P. Kushwaha, J. Gautam, A. Verma, B. Changkija, A. Kumar, S. Sharma, G. Nagar, D. Singh, P. Trivedi *et al.*, "Withaferin a: a proteasomal inhibitor promotes healing after injury and exerts anabolic effect on osteoporotic bone," *Cell death & disease*, vol. 4, no. 8, pp. e778–e778, 2013.

[65] A. A. Challa, M. Vukmirovic, J. Blackmon, and B. Stefanovic, "Withaferin-a reduces type i collagen expression in vitro and inhibits development of myocardial fibrosis in vivo," 2012.

[66] G. Imokawa and K. Ishida, "Inhibitors of intracellular signaling pathways that lead to stimulated epidermal pigmentation: Perspective of anti-pigmenting agents," *International journal of molecular sciences*, vol. 15, no. 5, pp. 8293–8315, 2014.

[67] N. Sen, B. Banerjee, B. Das, A. Ganguly, T. Sen, S. Pramanik, S. Mukhopadhyay, and H. Majumder, "Apoptosis is induced in leishmanial cells by a novel protein kinase inhibitor withaferin a and is facilitated by apoptotic topoisomerase i–dna complex," *Cell Death & Differentiation*, vol. 14, no. 2, pp. 358–367, 2007.

[68] C. Tripathi, R. Gupta, P. Kushawaha, C. Mandal, S. Misra Bhattacharya, and A. Dube, "Efficacy of w ithania somnifera chemotypes nmitli–101r, 118r and withaferin a against experimental visceral leishmaniasis," *Parasite Immunology*, vol. 36, no. 6, pp. 253–265, 2014.

[69] S.-K. Ku and J.-S. Bae, "Antiplatelet, anticoagulant, and profibrinolytic activities of withaferin a," *Vascular pharmacology*, vol. 60, no. 3, pp. 120–126, 2014.

[70] Y. Hao, S. Cheng, Y. Tanaka, Y. Hosokawa, Y. Yalikun, and M. Li, "Mechanical properties of single cells: Measurement methods and applications," *Biotechnology Advances*, vol. 45, p. 107648, 2020.

[71] C. T. Mierke, "The fundamental role of mechanical properties in the progression of cancer disease and inflammation," *Reports on Progress in Physics*, vol. 77, no. 7, p. 076602, 2014.

[72] Y. M. Efremov, M. Lomakina, D. Bagrov, P. Makhnovskiy, A. Alexandrova, M. Kirpichnikov, and K. Shaitan, "Mechanical properties of fibroblasts depend on level of cancer transformation," *Biochimica et Biophysica Acta (BBA)-Molecular Cell Research*, vol. 1843, no. 5, pp. 1013–1019, 2014.

[73] X. Cai, X. Xing, J. Cai, Q. Chen, S. Wu, and F. Huang, "Connection between biomechanics and cytoskeleton structure of lymphocyte and jurkat cells: An afm study," *Micron*, vol. 41, no. 3, pp. 257–262, 2010.

[74] S. K. Seidlits, Z. Z. Khaing, R. R. Petersen, J. D. Nickels, J. E. Vanscoy, J. B. Shear, and C. E. Schmidt, "The effects of hyaluronic acid hydrogels with tunable mechanical properties on neural progenitor cell differentiation," *Biomaterials*, vol. 31, no. 14, pp. 3930–3940, 2010.

[75] D. E. Discher, P. Janmey, and Y.-l. Wang, "Tissue cells feel and respond to the stiffness of their substrate," *Science*, vol. 310, no. 5751, pp. 1139–1143, 2005.

[76] G. Charras, P. P. Lehenkari, and M. Horton, "Atomic force microscopy can be used to mechanically stimulate osteoblasts and evaluate cellular strain distributions," *Ultramicroscopy*, vol. 86, no. 1-2, pp. 85–95, 2001.

[77] V. Gkretsi and T. Stylianopoulos, "Cell adhesion and matrix stiffness: coordinating cancer cell invasion and metastasis," *Frontiers in oncology*, vol. 8, p. 145, 2018.

[78] S.-Q. Chen, Q. Liao, O. W. Meldrum, L. Guo, K. Wang, S. Zhang, Y. Liu, X. Chen, J. Zhu, and L. Li, "Mechanical properties and wound healing potential of bacterial cellulose-xyloglucan-dextran hydrogels," *Carbohydrate Polymers*, vol. 321, p. 121268, 2023.

[79] G. Thomas, N. A. Burnham, T. A. Camesano, and Q. Wen, "Measuring the mechanical properties of living cells using atomic force microscopy," *JoVE (Journal of Visualized Experiments)*, no. 76, p. e50497, 2013.

[80] J. Guck, S. Schinkinger, B. Lincoln, F. Wottawah, S. Ebert, M. Romeyke, D. Lenz, H. M. Erickson, R. Ananthakrishnan, D. Mitchell *et al.*, "Optical deformability as an inherent cell marker for testing malignant transformation and metastatic competence," *Biophysical journal*, vol. 88, no. 5, pp. 3689–3698, 2005.

[81] S. E. Cross, Y.-S. Jin, J. Rao, and J. K. Gimzewski, "Nanomechanical analysis of cells from cancer patients," in *Nano-enabled medical applications*. Jenny Stanford Publishing, 2020, pp. 547–566.

[82] M. Plodinec, M. Loparic, C. A. Monnier, E. C. Obermann, R. Zanetti-Dallenbach, P. Oertle, J. T. Hyotyla, U. Aebi, M. Bentires-Alj, R. Y. Lim *et al.*, "The nanomechanical signature of breast cancer," *Nature nanotechnology*, vol. 7, no. 11, pp. 757–765, 2012.

[83] W. Xu, R. Mezencev, B. Kim, L. Wang, J. McDonald, and T. Sulchek, "Cell stiffness is a biomarker of the metastatic potential of ovarian cancer cells," 2012.

[84] Q. Li, G. Y. Lee, C. N. Ong, and C. T. Lim, "Afm indentation study of breast cancer cells," *Biochemical and biophysical research communications*, vol. 374, no. 4, pp. 609–613, 2008.

[85] L. Neary-Zajiczek, C. Essmann, N. Clancy, A. Haider, E. Miranda, M. Shaw, A. Gander, B. Davidson, D. Fernandez-Reyes, V. Pawar *et al.*, "Whole-sample mapping of cancerous and benign tissue properties," in *Medical Image Computing and Computer Assisted Intervention–MICCAI 2019: 22nd International Conference, Shenzhen, China, October 13–17, 2019, Proceedings, Part I 22*. Springer, 2019, pp. 760–768.

[86] A. F. Guedes, F. A. Carvalho, I. Malho, N. Lousada, L. Sargento, and N. C. Santos, "Atomic force microscopy as a tool to evaluate the risk of cardiovascular diseases in patients," *Nature nanotechnology*, vol. 11, no. 8, pp. 687–692, 2016.

[87] J. Jaffar, S.-H. Yang, S. Y. Kim, H.-W. Kim, A. Faiz, W. Chrzanowski, and J. K. Burgess, "Greater cellular stiffness in fibroblasts from patients with idiopathic pulmonary fibrosis," *American Journal of Physiology-Lung Cellular and Molecular Physiology*, vol. 315, no. 1, pp. L59–L65, 2018.

[88] A. P. Carapeto, M. V. Vitorino, J. D. Santos, S. S. Ramalho, T. Robalo, M. S. Rodrigues, and C. M. Farinha, "Mechanical properties of human bronchial epithelial cells expressing wt-and mutant cftr," *International Journal of Molecular Sciences*, vol. 21, no. 8, p. 2916, 2020.

[89] G. Y. Lee and C. T. Lim, "Biomechanics approaches to studying human diseases," *Trends in biotechnology*, vol. 25, no. 3, pp. 111–118, 2007.

[90] J. S. Lee, D. H. Sinn, S. Y. Park, H. J. Shin, H. W. Lee, B. K. Kim, J. Y. Park, D. Y. Kim, S. H. Ahn, J. H. Oh *et al.*, "Liver stiffness-based risk prediction model for hepatocellular carcinoma in patients with nonalcoholic fatty liver disease," *Cancers*, vol. 13, no. 18, p. 4567, 2021.

[91] H. Jin, X. Xing, H. Zhao, Y. Chen, X. Huang, S. Ma, H. Ye, and J. Cai, "Detection of erythrocytes influenced by aging and type 2 diabetes using atomic force microscope," *Biochemical and biophysical research communications*, vol. 391, no. 4, pp. 1698–1702, 2010.

[92] P. C. Georges and P. A. Janmey, "Cell type-specific response to growth on soft materials," *Journal of applied physiology*, vol. 98, no. 4, pp. 1547–1553, 2005.

[93] A. J. Engler, S. Sen, H. L. Sweeney, and D. E. Discher, "Matrix elasticity directs stem cell lineage specification," *Cell*, vol. 126, no. 4, pp. 677–689, 2006.

[94] P. M. Gilbert, K. L. Havenstrite, K. E. Magnusson, A. Sacco, N. A. Leonardi, P. Kraft, N. K. Nguyen, S. Thrun, M. P. Lutolf, and H. M. Blau, "Substrate elasticity regulates skeletal muscle stem cell self-renewal in culture," *Science*, vol. 329, no. 5995, pp. 1078–1081, 2010.

[95] N. Tarannum, R. Singh, and S. Woolner, "Sculpting an embryo: the interplay between mechanical force and cell division," *Journal of Developmental Biology*, vol. 10, no. 3, p. 37, 2022.

[96] S. Maheswaran and D. A. Haber, "Circulating tumor cells: a window into cancer biology and metastasis," *Current opinion in genetics & development*, vol. 20, no. 1, pp. 96–99, 2010.

[97] P.-H. Wu, D. R.-B. Aroush, A. Asnacios, W.-C. Chen, M. E. Dokukin, B. L. Doss, P. Durand-Smet, A. Ekpenyong, J. Guck, N. V. Guz *et al.*, "A comparison of methods to assess cell mechanical properties," *Nature methods*, vol. 15, no. 7, pp. 491–498, 2018.

[98] A. E. H. Love, *A treatise on the mathematical theory of elasticity*. Cambridge university press, 2013.

[99] R. Goldstein, V. Gorodtsov, and D. Lisovenko, "Variability of elastic properties of hexagonal auxetics." in *Doklady Physics*, vol. 56, no. 12, 2011.

[100] R. V. Goldstein, V. A. Gorodtsov, and D. S. Lisovenko, "Classification of cubic auxetics," *physica status solidi (b)*, vol. 250, no. 10, pp. 2038–2043, 2013.

[101] R. Lakes, "Foam structures with a negative poisson's ratio," *Science*, vol. 235, no. 4792, pp. 1038–1040, 1987.

[102] Z. Y. Wei, Z. V. Guo, L. Dudte, H. Y. Liang, and L. Mahadevan, "Geometric mechanics of periodic pleated origami," *Physical review letters*, vol. 110, no. 21, p. 215501, 2013.

[103] M. Doi, *Soft matter physics*. Oxford University Press, USA, 2013.

[104] J. Y. Rho, R. B. Ashman, and C. H. Turner, "Young's modulus of trabecular and cortical bone material: ultrasonic and microtensile measurements," *Journal of biomechanics*, vol. 26, no. 2, pp. 111–119, 1993.

[105] C. G. Caro, *The mechanics of the circulation*. Cambridge University Press, 2012.

[106] M. Stekelenburg, M. C. Rutten, L. H. Snoeckx, and F. P. Baaijens, "Dynamic straining combined with fibrin gel cell seeding improves strength of tissue-engineered small-diameter vascular grafts," *Tissue Engineering Part A*, vol. 15, no. 5, pp. 1081–1089, 2009.

[107] Y. Feng, Y. Li, C. Liu, and Z. Zhang, "Assessing the elastic properties of skeletal muscle and tendon using shearwave ultrasound elastography and myotonpro," *Scientific reports*, vol. 8, no. 1, p. 17064, 2018.

[108] P. J. Fellows, *Food processing technology: principles and practice*. Woodhead publishing, 2022.

[109] B. Bhandari, B. D'Arcy, and C. Kelly, "Rheology and crystallization kinetics of honey: present status," *International Journal of Food Properties*, vol. 2, no. 3, pp. 217–226, 1999.

[110] C. Lim, E. Zhou, and S. Quek, "Mechanical models for living cells—a review," *Journal of biomechanics*, vol. 39, no. 2, pp. 195–216, 2006.

[111] E. Evans and A. Yeung, "Apparent viscosity and cortical tension of blood granulocytes determined by micropipet aspiration," *Biophysical journal*, vol. 56, no. 1, pp. 151–160, 1989.

[112] C. Dong, R. Skalak, and K.-L. P. Sung, "Cytoplasmic rheology of passive neutrophils," *Biorheology*, vol. 28, no. 6, pp. 557–567, 1991.

[113] N. Caille, O. Thoumine, Y. Tardy, and J.-J. Meister, "Contribution of the nucleus to the mechanical properties of endothelial cells," *Journal of biomechanics*, vol. 35, no. 2, pp. 177–187, 2002.

[114] R. Hochmuth, H. Ting-Beall, B. Beaty, D. Needham, and R. Tran-Son-Tay, "Viscosity of passive human neutrophils undergoing small deformations," *Biophysical journal*, vol. 64, no. 5, pp. 1596–1601, 1993.

[115] H.-C. Kan, H. S. Udaykumar, W. Shyy, and R. Tran-Son-Tay, "Hydrodynamics of a compound drop with application to leukocyte modeling," *Physics of fluids*, vol. 10, no. 4, pp. 760–774, 1998.

[116] M. A. Tsai, R. S. Frank, and R. E. Waugh, "Passive mechanical behavior of human neutrophils: power-law fluid," *Biophysical journal*, vol. 65, no. 5, pp. 2078–2088, 1993.

[117] C. Dong, R. Skalak, K.-L. P. Sung, G. Schmid-Scho¨ nbein, and S. Chien, "Passive deformation analysis of human leukocytes," 1988.

[118] G. Schmid-Schönbein, K.-L. Sung, H. Tözeren, R. Skalak, and S. Chien, "Passive mechanical properties of human leukocytes," *Biophysical Journal*, vol. 36, no. 1, pp. 243–256, 1981.

[119] J. Hildebrandt, "Comparison of mathematical models for cat lung and viscoelastic balloon derived by laplace transform methods from pressurevolume data," *The Bulletin of mathematical biophysics*, vol. 31, pp. 651–667, 1969.

[120] J. J. Fredberg and D. Stamenovic, "On the imperfect elasticity of lung tissue," *Journal of applied physiology*, vol. 67, no. 6, pp. 2408–2419, 1989.

[121] G. N. Maksym, B. Fabry, J. P. Butler, D. Navajas, D. J. Tschumperlin, J. D. Laporte, and J. J. Fredberg, "Mechanical properties of cultured human airway smooth muscle cells from 0.05 to 0.4 hz," *Journal of applied physiology*, vol. 89, no. 4, pp. 1619–1632, 2000.

[122] M. Rodriguez and N. Sniadecki, "Computational modeling of cell mechanics," *Computational Modelling of Biomechanics and Biotribology in the Musculoskeletal System*, pp. 93–140, 2014.

[123] V. C. Mow, S. Kuei, W. M. Lai, and C. G. Armstrong, "Biphasic creep and stress relaxation of articular cartilage in compression: theory and experiments," 1980.

[124] P. Torzilli and V. C. Mow, "On the fundamental fluid transport mechanisms through normal and pathological articular cartilage during function—i the formulation," *Journal of biomechanics*, vol. 9, no. 8, pp. 541–552, 1976.

[125] V. C. Mow and J. M. Mansour, "The nonlinear interaction between cartilage deformation and interstitial fluid flow," *Journal of biomechanics*, vol. 10, no. 1, pp. 31–39, 1977.

[126] D. E. Ingber, "Cellular tensegrity: defining new rules of biological design that govern the cytoskeleton," *Journal of cell science*, vol. 104, no. 3, pp. 613–627, 1993.

[127] D. Stamenović, J. J. Fredberg, N. Wang, J. P. Butler, and D. E. Ingber, "A microstructural approach to cytoskeletal mechanics based on tensegrity," *Journal of Theoretical Biology*, vol. 181, no. 2, pp. 125–136, 1996.

[128] R. L. Satcher and C. F. Dewey, "Theoretical estimates of mechanical properties of the endothelial cell cytoskeleton," *Biophysical journal*, vol. 71, no. 1, pp. 109–118, 1996.

[129] V. Bennett, "The spectrin-actin junction of erythrocyte membrane skeletons," *Biochimica et Biophysica Acta (BBA)-Reviews on Biomembranes*, vol. 988, no. 1, pp. 107–121, 1989.

[130] D. Kabaso, R. Shlomovitz, T. Auth, V. L. Lew, and N. S. Gov, "Curling and local shape changes of red blood cell membranes driven by cytoskeletal reorganization," *Biophysical journal*, vol. 99, no. 3, pp. 808–816, 2010.

[131] D. H. Boal, "Computer simulation of a model network for the erythrocyte cytoskeleton," *Biophysical Journal*, vol. 67, no. 2, pp. 521–529, 1994.

[132] S. K. Boey, D. H. Boal, and D. E. Discher, "Simulations of the erythrocyte cytoskeleton at large deformation. i. microscopic models," *Biophysical Journal*, vol. 75, no. 3, pp. 1573–1583, 1998.

[133] D. E. Discher, D. H. Boal, and S. K. Boey, "Simulations of the erythrocyte cytoskeleton at large deformation. ii. micropipette aspiration," *Biophysical Journal*, vol. 75, no. 3, pp. 1584–1597, 1998.

[134] S. G. Kulkarni, S. Pérez-Domínguez, and M. Radmacher, "Influence of cantilever tip geometry and contact model on afm elasticity measurement of cells," *Journal of Molecular Recognition*, p. e3018, 2023.

[135] G. Binnig, H. Rohrer, C. Gerber, and E. Weibel, "Surface studies by scanning tunneling microscopy," *Physical review letters*, vol. 49, no. 1, p. 57, 1982.

[136] G. Binnig, C. F. Quate, and C. Gerber, "Atomic force microscope," *Physical review letters*, vol. 56, no. 9, p. 930, 1986.

[137] G. Binnig, C. Gerber, E. Stoll, T. Albrecht, and C. Quate, "Atomic resolution with atomic force microscope," *Europhysics Letters*, vol. 3, no. 12, p. 1281, 1987.

[138] C. Quate, "The afm as a tool for surface imaging," *Surface Science*, vol. 299, pp. 980–995, 1994.

[139] B. Bhushan, "Wear and mechanical characterisation on micro-to picoscales using afm," *International materials reviews*, vol. 44, no. 3, pp. 105–117, 1999.

[140] S. Kim, D. C. Ratchford, and X. Li, "Atomic force microscope nanomanipulation with simultaneous visual guidance," *ACS nano*, vol. 3, no. 10, pp. 2989–2994, 2009.

[141] M. Kappl and H.-J. Butt, "The colloidal probe technique and its application to adhesion force measurements," *Particle & Particle Systems Characterization: Measurement and Description of Particle Properties and Behavior in Powders and Other Disperse Systems*, vol. 19, no. 3, pp. 129–143, 2002.

[142] D. L. Sedin and K. L. Rowlen, "Adhesion forces measured by atomic force microscopy in humid air," *Analytical chemistry*, vol. 72, no. 10, pp. 2183–2189, 2000.

[143] H. H. Fang, K.-Y. Chan, and L.-C. Xu, "Quantification of bacterial adhesion forces using atomic force microscopy (afm)," *Journal of microbiological methods*, vol. 40, no. 1, pp. 89–97, 2000.

[144] G. Marshall Jr, M. Balooch, R. Gallagher, S. Gansky, and S. Marshall, "Mechanical properties of the dentinoenamel junction: Afm studies of nanohardness, elastic modulus, and fracture," *Journal of Biomedical Materials Research: An Official Journal of The Society for Biomaterials and The Japanese Society for Biomaterials*, vol. 54, no. 1, pp. 87–95, 2001.

[145] S. Sundararajan and B. Bhushan, "Development of afm-based techniques to measure mechanical properties of nanoscale structures," *Sensors and actuators A: Physical*, vol. 101, no. 3, pp. 338–351, 2002.

[146] Y. Li, J. Yang, Z. Pan, and W. Tong, "Nanoscale pore structure and mechanical property analysis of coal: An insight combining afm and sem images," *Fuel*, vol. 260, p. 116352, 2020.

[147] D. G. de Oteyza, P. Gorman, Y.-C. Chen, S. Wickenburg, A. Riss, D. J. Mowbray, G. Etkin, Z. Pedramrazi, H.-Z. Tsai, A. Rubio *et al.*, "Direct imaging of covalent bond structure in single-molecule chemical reactions," *Science*, vol. 340, no. 6139, pp. 1434–1437, 2013.

[148] S. J. T. van Noort, O. H. Willemsen, K. O. van der Werf, B. G. de Grooth, and J. Greve, "Mapping electrostatic forces using higher harmonics tapping mode atomic force microscopy in liquid," *Langmuir*, vol. 15, no. 21, pp. 7101–7107, 1999.

[149] T. R. Rodriguez and R. García, "Compositional mapping of surfaces in atomic force microscopy by excitation of the second normal mode of the microcantilever," *Applied Physics Letters*, vol. 84, no. 3, pp. 449–451, 2004.

[150] R. Proksch, "Multifrequency, repulsive-mode amplitude-modulated atomic force microscopy," *Applied Physics Letters*, vol. 89, no. 11, 2006.

[151] R. Barrett and C. Quate, "High-speed, large-scale imaging with the atomic force microscope," *Journal of Vacuum Science & Technology B: Microelectronics and Nanometer Structures Processing, Measurement, and Phenomena*, vol. 9, no. 2, pp. 302–306, 1991.

[152] N. Kodera, D. Yamamoto, R. Ishikawa, and T. Ando, "Video imaging of walking myosin v by high-speed atomic force microscopy," *Nature*, vol. 468, no. 7320, pp. 72–76, 2010.

[153] A. Meister, M. Gabi, P. Behr, P. Studer, J. Vörös, P. Niedermann, J. Bitterli, J. Polesel-Maris, M. Liley, H. Heinzelmann *et al.*, "Fluidfm: combining atomic force microscopy and nanofluidics in a universal liquid delivery system for single cell applications and beyond," *Nano letters*, vol. 9, no. 6, pp. 2501–2507, 2009.

[154] A. E. Brown, A. Hategan, D. Safer, Y. E. Goldman, and D. E. Discher, "Cross-correlated tirf/afm reveals asymmetric distribution of force-generating heads along self-assembled,"synthetic" myosin filaments," *Biophysical journal*, vol. 96, no. 5, pp. 1952–1960, 2009.

[155] E. Bailo and V. Deckert, "Tip-enhanced raman spectroscopy of single rna strands: towards a novel direct-sequencing method," *Angewandte Chemie International Edition*, vol. 47, no. 9, pp. 1658–1661, 2008.

[156] S. Berweger, D. M. Nguyen, E. A. Muller, H. A. Bechtel, T. T. Perkins, and M. B. Raschke, "Nano-chemical infrared imaging of membrane proteins in lipid bilayers," *Journal of the American Chemical Society*, vol. 135, no. 49, pp. 18 292–18 295, 2013.

[157] D. Fronczek, C. Quammen, H. Wang, C. Kisker, R. Superfine, R. Taylor, D. Erie, and I. Tessmer, "High accuracy fiona–afm hybrid imaging," *Ultramicroscopy*, vol. 111, no. 5, pp. 350–355, 2011.

[158] G. R. Heath, E. Kots, J. L. Robertson, S. Lansky, G. Khelashvili, H. Weinstein, and S. Scheuring, "Localization atomic force microscopy," *Nature*, vol. 594, no. 7863, pp. 385–390, 2021.

[159] S. Gould, O. Marti, B. Drake, L. Hellemans, C. E. Bracker, P. K. Hansma, N. L. Keder, M. M. Eddy, and G. D. Stucky, "Molecular resolution images of amino acid crystals with the atomic force microscope," *Nature*, vol. 332, no. 6162, pp. 332–334, 1988.

[160] H.-J. Butt, E. Wolff, S. Gould, B. D. Northern, C. Peterson, and P. Hansma, "Imaging cells with the atomic force microscope," *Journal of structural biology*, vol. 105, no. 1-3, pp. 54–61, 1990.

[161] W. Kolbe, D. Ogletree, and M. Salmeron, "Atomic force microscopy imaging of t4 bacteriophages on silicon substrates," *Ultramicroscopy*, vol. 42, pp. 1113–1117, 1992.

[162] J. Thimonier, C. Montixi, J.-P. Chauvin, H. T. He, J. Rocca-Serra, and J. Barbet, "Thy-1 immunolabeled thymocyte microdomains studied with the atomic force microscope and the electron microscope," *Biophysical journal*, vol. 73, no. 3, pp. 1627–1632, 1997.

[163] H.-J. Butt, K. H. Downing, and P. K. Hansma, "Imaging the membrane protein bacteriorhodopsin with the atomic force microscope," *Biophysical journal*, vol. 58, no. 6, pp. 1473–1480, 1990.

[164] E. Henderson, P. Haydon, and D. Sakaguchi, "Actin filament dynamics in living glial cells imaged by atomic force microscopy," *Science*, vol. 257, no. 5078, pp. 1944–1946, 1992.

[165] S. Kasas, V. Gotzos, and M. Celio, "Observation of living cells using the atomic force microscope," *Biophysical journal*, vol. 64, no. 2, pp. 539–544, 1993.

[166] C. A. Putman, K. O. Van der Werf, B. G. De Grooth, N. F. Van Hulst, and J. Greve, "Tapping mode atomic force microscopy in liquid," *Applied physics letters*, vol. 64, no. 18, pp. 2454–2456, 1994.

[167] S. Nagayama, M. Morimoto, K. Kawabata, Y. Fujito, S. Ogura, K. Abe, T. Ushiki, and E. Ito, "Afm observation of three-dimensional fine structural changes in living neurons," *Bioimages*, vol. 4, no. 3, pp. 111–116, 1996.

[168] C. Rotsch, F. Braet, E. Wisse, and M. Radmacher, "Afm imaging and elasticity measurements on living rat liver macrophages," *Cell biology international*, vol. 21, no. 11, pp. 685–696, 1997.

[169] U. G. Hofmann, C. Rotsch, W. J. Parak, and M. Radmacher, "Investigating the cytoskeleton of chicken cardiocytes with the atomic force microscope," *Journal of structural biology*, vol. 119, no. 2, pp. 84–91, 1997.

[170] A. Emad, W. F. Heinz, M. D. Antonik, N. P. D'Costa, S. Nageswaran, C.-A. Schoenenberger, J. H. Hoh *et al.*, "Relative microelastic mapping of living cells by atomic force microscopy," *Biophysical journal*, vol. 74, no. 3, pp. 1564–1578, 1998.

[171] N. Tao, S. Lindsay, and S. Lees, "Measuring the microelastic properties of biological material," *Biophysical journal*, vol. 63, no. 4, pp. 1165–1169, 1992.

[172] K. A. Barbee, P. F. Davies, and R. Lal, "Shear stress-induced reorganization of the surface topography of living endothelial cells imaged by atomic force microscopy." *Circulation research*, vol. 74, no. 1, pp. 163–171, 1994.

[173] C. Bustamante, J. Vesenka, C. L. Tang, W. Rees, M. Guthold, and R. Keller, "Circular dna molecules imaged in air by scanning force microscopy," *Biochemistry*, vol. 31, no. 1, pp. 22–26, 1992.

[174] H. G. Hansma, R. L. Sinsheimer, M.-Q. Li, and P. K. Hansma, "Atomic force microscopy of single-and double-stranded dna," *Nucleic acids research*, vol. 20, no. 14, pp. 3585–3590, 1992.

[175] B. G. D. Grooth and C. A. Putman, "High-resolution imaging of chromosome-related structures by atomic force microscopy," *Journal of microscopy*, vol. 168, no. 3, pp. 239–247, 1992.

[176] H. Hansma, J. Vesenka, C. Siegerist, G. Kelderman, H. Morrett, R. L. Sinsheimer, V. Elings, C. Bustamante, and P. Hansma, "Reproducible imaging and dissection of plasmid dna under liquid with the atomic force microscope," *Science*, vol. 256, no. 5060, pp. 1180–1184, 1992.

[177] H. Arakawa, K. Umemura, and A. Ikai, "Protein images obtained by stm, afm and tem." *Nature*, vol. 358, no. 6382, pp. 171–173, 1992.

[178] E. A. Chernoff and D. A. Chernoff, "Atomic force microscope images of collagen fibers," *Journal of Vacuum Science & Technology A: Vacuum, Surfaces, and Films*, vol. 10, no. 4, pp. 596–599, 1992.

[179] J. Donachy, B. Drake, and C. Sikes, "Sequence and atomic-force microscopy analysis of a matrix protein from the shell of the oyster crassostrea virginica," *Marine Biology*, vol. 114, pp. 423–428, 1992.

[180] S. Ohnishi, M. Hara, T. Furuno, and H. Sasabe, "Imaging the ordered arrays of water-soluble protein ferritin with the atomic force microscope," *Biophysical journal*, vol. 63, no. 5, pp. 1425–1431, 1992.

[181] P. Hinterdorfer, W. Baumgartner, H. J. Gruber, K. Schilcher, and H. Schindler, "Detection and localization of individual antibody-antigen recognition events by atomic force microscopy." *Proceedings of the National Academy of Sciences*, vol. 93, no. 8, pp. 3477–3481, 1996.

[182] M. GAD, A. Itoh, and A. Ikai, "Mapping cell wall polysaccharides of living microbial cells using atomic force microscopy," *Cell biology international*, vol. 21, no. 11, pp. 697–706, 1997.

[183] L. Kordylewski, D. Saner, and R. Lal, "Atomic force microscopy of freeze-fracture replicas of rat atrial tissue," *Journal of microscopy*, vol. 173, no. 3, pp. 173–181, 1994.

[184] R. Lal and S. A. John, "Biological applications of atomic force microscopy," *American Journal of Physiology-Cell Physiology*, vol. 266, no. 1, pp. C1–C21, 1994.

[185] A. Engel and D. J. Müller, "Observing single biomolecules at work with the atomic force microscope," *Nature structural biology*, vol. 7, no. 9, pp. 715–718, 2000.

[186] P. Hansma, J. Cleveland, M. Radmacher, D. Walters, P. Hillner, M. Bezanilla, M. Fritz, D. Vie, H. Hansma, C. Prater *et al.*, "Tapping mode atomic force microscopy in liquids," *Applied Physics Letters*, vol. 64, no. 13, pp. 1738–1740, 1994.

[187] A. C. Dumitru and M. Koehler, "Recent advances in the application of atomic force microscopy to structural biology," *Journal of Structural Biology*, p. 107963, 2023.

[188] J. Galvao, B. Davis, M. Tilley, E. Normando, M. R. Duchen, and M. F. Cordeiro, "Unexpected low-dose toxicity of the universal solvent dmso," *The FASEB Journal*, vol. 28, no. 3, pp. 1317–1330, 2014.

[189] R. Kudělka, L. Václavek, J. Tomáštík, S. Malecová, and R. Čtvrtlík, "Laser-induced surface acoustic waves for thin film characterization," *Acta Polytechnica CTU Proceedings*, vol. 27, pp. 57–61, 2020.

[190] J. Chen, J. Shi, Y. Wang, J. Sun, J. Han, K. Sun, and L. Fang, "Nanoindentation and deformation behaviors of silicon covered with amorphous sio 2: a molecular dynamic study," *RSC advances*, vol. 8, no. 23, pp. 12 597–12 607, 2018.

[191] I. N. Sneddon, "The relation between load and penetration in the axisymmetric boussinesq problem for a punch of arbitrary profile," *International journal of engineering science*, vol. 3, no. 1, pp. 47–57, 1965.

[192] A. Vinckier and G. Semenza, "Measuring elasticity of biological materials by atomic force microscopy," *FEBS letters*, vol. 430, no. 1-2, pp. 12–16, 1998.

[193] Y.-R. Chang, V. K. Raghunathan, S. P. Garland, J. T. Morgan, P. Russell, and C. J. Murphy, "Automated afm force curve analysis for determining elastic modulus of biomaterials and biological samples," *Journal of the mechanical behavior of biomedical materials*, vol. 37, pp. 209–218, 2014.

[194] N. Guz, M. Dokukin, V. Kalaparthi, and I. Sokolov, "If cell mechanics can be described by elastic modulus: study of different models and probes used in indentation experiments," *Biophysical journal*, vol. 107, no. 3, pp. 564–575, 2014.

[195] M. Offroy, A. Razafitianamaharavo, A. Beaussart, C. Pagnout, and J. F. Duval, "Fast automated processing of afm peakforce curves to evaluate spatially resolved young modulus and stiffness of turgescent cells," *RSC advances*, vol. 10, no. 33, pp. 19 258–19 275, 2020.

[196] W. C. Oliver and G. M. Pharr, "An improved technique for determining hardness and elastic modulus using load and displacement sensing indentation experiments," *Journal of materials research*, vol. 7, no. 6, pp. 1564–1583, 1992.

[197] ——, "Measurement of hardness and elastic modulus by instrumented indentation: Advances in understanding and refinements to methodology," *Journal of materials research*, vol. 19, no. 1, pp. 3–20, 2004.

[198] T. Ting, "The contact stresses between a rigid indenter and a viscoelastic half-space," 1966.

[199] Y. M. Efremov, W.-H. Wang, S. D. Hardy, R. L. Geahlen, and A. Raman, "Measuring nanoscale viscoelastic parameters of cells directly from afm force-displacement curves," *Scientific reports*, vol. 7, no. 1, p. 1541, 2017.

[200] P. Chugh and E. K. Paluch, "The actin cortex at a glance," *Journal of cell science*, vol. 131, no. 14, p. jcs186254, 2018.

[201] W. R. Inc., "Mathematica, Version 13.3," champaign, IL, 2023. [Online]. Available: https://www.wolfram.com/mathematica